Modeling Optical Technologies with Continuous and Discrete Nonlinear Schrödinger Equations

Zur Erlangung des akademischen Grades eines

DOKTORS DER NATURWISSENSCHAFTEN

von der Fakultät für Mathematik
der Universität Karlsruhe (TH) genehmigte
DISSERTATION
von

MSc.-Math. Christopher Chong

aus

Boston, MA USA

Tag der mündlichen Prüfung: 23. Juli 2009

Referent: Prof. Dr. Guido Schneider
Korreferent: Prof. Dr. Michael Plum

This thesis is dedicated to my late uncle Bill.

Contents

Acknowledgements

I owe the most gratitude to my PhD adviser Prof. Dr. Guido Schneider who provided many invaluable comments, suggestions, and improvements to this thesis. He included me in several aspects of his research and encouraged me to discuss and work with others, which in the end helped me mature as a researcher.

I thank Prof. Dr. Michael Plum for taking the time to be a member of my thesis committee and for the useful comments and discussions concerning the content of this thesis.

In addition to my advisers, I would like to mention a few of the people I interacted with during my time as a doctoral candidate. They each had a positive impact on this work in some way.

I owe many thanks to my former MSc adviser Prof. Dr. Ricardo Carretero. He maintained this role informally during my PhD studies. I received a great deal of feedback concerning discrete nonlinear Schrödinger (DNLS) equations and other aspects of an academic nature. The hospitality at San Diego State university during a research visit in January 2008 is appreciated.

I am happy to have experienced the turbulence of PhD life with my colleague and friend Martina Chrilius-Bruckner. We had many long discussions over several areas of mathematics, physics, and also of a personal nature.

I thank Professor Dr. Willy Dörfler for coordinating our research training group and for feedback concerning numerical integration of wave equations.

I appreciated feedback from Professors Dr. Ernst Hairer and Dr. Christian Lubich concerning numerical integration of nonlinear wave equations, especially geometric integrators.

I thank Dr. Kirankumar Hiremath for taking the time to read the physical setting section of this thesis and for our scientific and personal discussions.

I thank Prof. Dr. Panayotis Kevrekidis for inviting me to the Mathematics department of the University of Massachusetts, Amherst to work on DNLS related problems. His feedback for the two-dimensional case was particularly helpful.

Prof. Dr. Boris Malomed originally proposed studying the cubic-quintic DNLS equation, of which a large part of this thesis is dedicated to. Naturally, his input was extremely valuable.

Prof. Dr. Dmitry Pelinovksy was very willing to answer my several questions concerning the properties of DNLS operators and variational approximations of discrete solitons. I appreciated the hospitality of his host institute, McMaster University, during a research visit in January 2009.

I am very thankful to Christina Spaniol and Denise Chong for proof reading the text and finding typographical errors and to Danny Chong for designing Fig. A.7.

I thank Prof. Dr. Hannes Uecker for his input concerning pulse interaction and numerical integrators.

Finally I would like to thank the faculty members and my other colleagues of the mathematics department at the Universität Karlsruhe and the Universität Stuttgart for questions raised during the presentations I gave concerning topics that appear in this dissertation.

This work was supported by the German Research Foundation (DFG) through the GRK 1294: Analysis, Simulation and Design of Nanotechnological Processes. Travel expenses were partially supported by the Humboldt Foundation and the National Science Foundation.

Chapter 1

Introduction

Optics is the science that deals with the genesis, propagation, and properties of light and its interaction with matter. Various modern technologies are based on optical principles and operate by exploiting some light related phenomena. One common example is optical communication, where light signals are sent through *fiber optic* cables and represent bits of information.

One can elicit information about the physical system by studying the underlying model equations. This is especially important when direct experimentation is costly. The main theme of this dissertation is the mathematical analysis and numerical simulation of models that describe optical technologies, particularly nonlinear fiber optics and nonlinear waveguide arrays. A more detailed description of these two technologies can be found in Appendix A or in Refs. [Agr01, CLS03]. Derivations of the studied models from the fundamental physical laws (i.e. the Maxwell equations) are also given there. Another unifying theme of this thesis is the importance of the relationship: *numerical investigation* $\leftrightarrow$ *conjecture* $\rightarrow$ *theorem*. The first two steps should be considered as a loop, where the numerics can motivate a conjecture and/or verify or deny an existing conjecture. Ideally, the information gained from this process can be used to produce a theorem. What is studied here is a small part of an already extensive field of research. Therefore, Fig. 1.1 is provided to put the results of this thesis into context and perspective.

In Chapter 2 (left two columns of Fig. 1.1) we approach the problem of the interaction of modulated pulses in nonlinear dispersive media. This is relevant for fiber optic communication systems, as seen in Appendix A.1. The nonlinear Klein-Gordon (NKG) equation is used as a prototype for our study. Rigorous estimates of the interaction of modulated pulses were previously studied in works like [PW96, BF06]. In [OY74, TPB04] pulse interaction is also described, and formulas for the phase and envelope shift resulting from this interaction were derived. Later, in [CBSU07] it was shown that an improved estimate (compared to that in [PW96]) is possible by combining ideas from [TPB04, OY74] (explicit representation of the phase and envelope shifts) and [KSM92] (justification of the estimate). Additionally, it was implicitly conjectured that in order to obtain the improved estimates one needs a special form of the envelope function. Our work begins where [CBSU07] left off. After performing an intensive numerical investigation, it is shown that the conjecture is *incorrect*. This investigation is conducted with the use of several integrators, for one of which a proof of convergence is provided. For these reasons, we are fairly confident in the obtained results. Indeed based on the numerical investigation, a modified statement is proposed and proved.

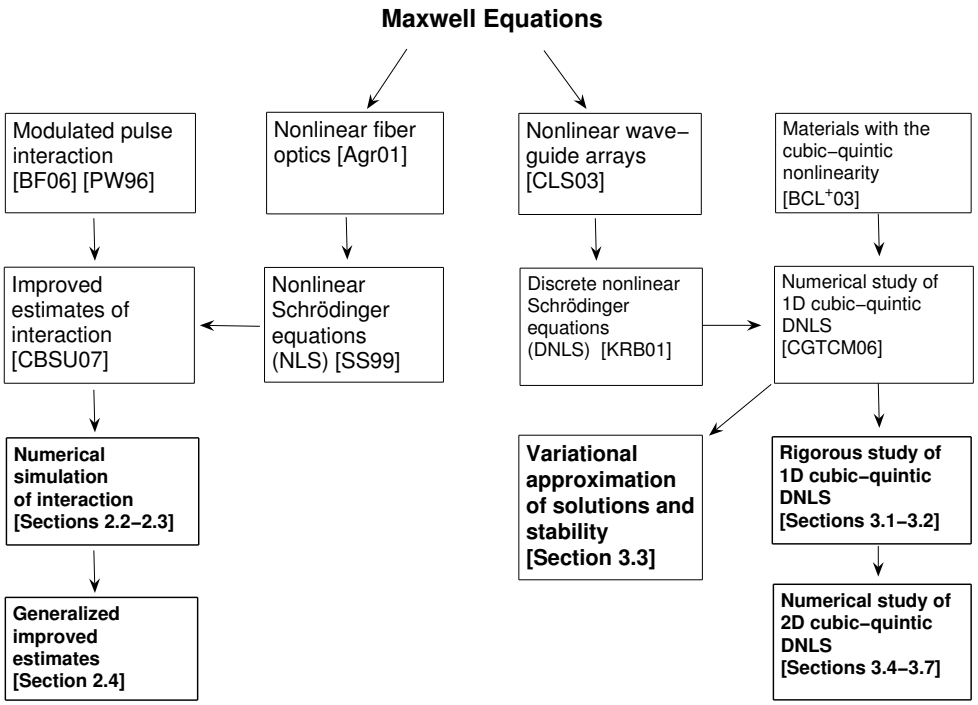

Figure 1.1: How the results presented in this thesis (bold items) are an extension of the existing pool of knowledge concerning optical technologies. Explanations of the relationships are given in this introduction.

Chapter 2 is structured as follows. In Sec. 2.1 we outline the results of [CBSU07]. By posing a multiple-scale ansatz, the problem of pulse propagation and evolution is reduced to solving a *continuous* nonlinear Schrödinger (NLS) equation which describes slow modulations in time and space of the underlying carrier wave (see Ref. [SS99] for more on the NLS equation). In a similar fashion a two pulse ansatz is constructed. The improved estimates of the approximation and phase shift are justified. The conjecture (cf. [CBSU07, Remark 1.4]) is that the envelope functions must be NLS 1-solitons in order to obtain the improved estimate. In Sec. 2.2 the four integrators used for the numerical study are explained. Due to the multiple-scale character of the problem, many spatial grid points are required. Therefore, the choice of integrator is important. These include a finite difference scheme, a method of lines, and two pseudo-spectral methods. The convergence rate for the finite difference method is proved in terms of the spatial step size. We found that the pseudo-spectral methods, which utilize the fast Fourier transform (FFT), allow for larger spatial steps, which is most likely due to the localization of the corresponding spectrum. It is also observed that *all* of the methods conserve energy (the Hamiltonian) for long time-periods. In Sec. 2.3 we present the results of the simulations which discredit the conjecture implicitly made in [CBSU07]. Namely, we show that the improved estimates of the phase and envelope shifts are possible without assuming the envelope is an NLS 1-soliton. The final section, 2.4, states the generalized claim, which is also proved. This is possible by interpreting the terms in the residual in a special way; by separating terms that account for internal dynamics and those that account for interaction dynamics, one can reduce the residual to the required amount. The numerical simulations and analysis presented in Chapter 2 provide an almost complete description of modulated pulse interaction in the NKG equation with a cubic nonlinearity, thus providing a reasonable conclusion to the problem. The underlying ideas discussed here are extended to other models, including those with periodic coefficients, which are presented in a general and broader context in the PhD thesis of Chirilus-Bruckner [CB09]. There, the focus is on the methodology, rather than specific and salient features of the pulse interaction itself and thus provides a nice contrast and complement to Chapter 2 of this thesis.

In Chapter 3 (right two columns of Fig. 1.1) properties of localized solutions of a *discrete* nonlinear Schrödinger (DNLS) equation are studied. In Appendix A.2 it is shown that DNLS equations describe light propagation in waveguide arrays. Much of the existing literature is dedicated to models with the cubic nonlinearity (see reviews [KRB01, JM03]). Recent experimental works (cf. Ref. [BCL$^+$03]) have shown that cubic-quintic nonlinearities are also relevant. This motivated the more recent theoretical study [CGTCM06] where the existence of localized solutions (sometimes called discrete solitons) is studied using a dynamical reduction and numerical methods. Eigenvalues of the spectral problem determining stability are also computed numerically, and the existence of pitchfork and saddle-node bifurcations is conjectured, which is based on the numerical continuation. In this thesis, we rigorously verify some of the claims made in [CGTCM06] (see below). An analytical approximation of the solutions is developed here and the corresponding stability is predicted. A numerical study of the associated two-dimensional model (in space) is also included.

Chapter 3 is structured as follows. In Sec. 3.1 we begin by rigorously verifying some of the claims made in [CGTCM06]. Specifically, (a) the existence and uniqueness of discrete solitons is proved, (b) an exact expression for the essential spectrum of the operator determining stability is provided and (c) the existence of saddle-node and pitchfork bifurcations is proved. Analytic conditions of the bifurcation theorem are verified numerically. In Sec. 3.2 the relevant numerical methods to approximate the solutions and stability are described.

Additionally, for numerical computations of the discrete spectrum, the persistence of eigenvalues of the truncated problem in the infinite dimensional problem is proved. In Sec. 3.3 an analytical approximation of the discrete solitons and the corresponding spectrum based on the Lagrangian formulation of the problem is derived. The anstaz used in this so-called variational approximation was first used in Ref. [Kau05] to describe discrete solitons of DNLS models with the cubic nonlinearity. Stability was not predicted there. Finally, in Secs. 3.4-3.7 the system in the space of two dimensions is explored numerically, and a number of conjectures concerning the classification of the bifurcations are posed. Similarly to the 1D model, a variational approximation is formulated for the higher dimensional discrete-solitons, although stability is not approximated. The last section explores the mobility of the 2D discrete solitons; a conjecture supported by numerical computations stating that mobility is related to energy differences between the solution families is formulated.

Remark 1.1. Some of the material presented here can also be found in [CBCSU08,CCGMK09], however a large extent of the results can only be found in this thesis. References to these two works are made explicitly where appropriate.

Remark 1.2. All chapters should be considered independent in terms of notation, e.g. the meaning of C in Chapter 2 is different than in Chapter 3. A list of symbols and other notations used is given in Appendix B.

Chapter 2

Interaction of modulated pulses in the nonlinear Klein-Gordon equation

In this chapter a detailed description of the interaction of modulated pulses with different carrier waves is given. This is done within the context of the nonlinear Klein-Gordon (NKG) equation. It will be shown that the nonlinear Schrödinger (NLS) equation can be derived in a rigorous way, eventually leading to an improved estimate for the interaction. The derivation of the NLS equation from the Maxwell equations as found in the relevant physics texts is summarized in Appendix A.1.

In Ref. [CBSU07] approximate modulated pulse solutions were derived in order to describe two pulse interaction. Based on the assumption that the modulating envelopes are NLS 1-solitons, it was possible to prove error estimates that were an order better than existing estimates found in [PW96]. It was implicitly conjectured that the NLS 1-soliton condition was necessary, cf. [CBSU07, Remark 1.4]. One goal was to check this claim by conducting an intensive numerical study with the aid of various integrators and some tools from numerical analysis. Based on the results, we show that the original NLS 1-soliton conjecture was incorrect. This eventually leads to an almost complete description of the interaction dynamics, which in turn is represented in a general version of the theorem presented in Ref. [CBSU07]. The numerics also suggest that the estimate is optimal.

It should be noted that the NKG equation cannot be derived directly from the Maxwell equations. However, the extension of the ideas presented in this chapter should be extendable to physically realistic equations since dispersion and nonlinear interaction are present in the NKG equation.

We start by introducing the NKG equation,

$$\partial_t^2 u = \partial_x^2 u - u + u^3, \tag{2.1}$$

where $u = u(x,t), x, t \in \mathbb{R}$. The associated first order system,

$$\begin{cases} \partial_t u = v, \\ \partial_t v = \partial_x^2 u - u + u^3, \end{cases} \tag{2.2}$$

is a Hamiltonian system,

$$\partial_t \begin{pmatrix} u \\ v \end{pmatrix} = J \nabla H(u, v), \tag{2.3}$$

with the Hamiltonian,

$$H(u, v) = \int_{-\infty}^{\infty} \frac{1}{2} \left(\quad v^2 + (\partial_x u)^2 + u^2 \right)(x) - \frac{u(x)^4}{4} dx, \tag{2.4}$$

and skew symmetric operator,

$$J = \begin{pmatrix} 0 & 1 \\ -1 & 0 \end{pmatrix}. \tag{2.5}$$

A broad analytical treatment of Eq. (2.1) is given in Ref. [Tao06].

2.1 Pulse interaction approximated by the NLS equation

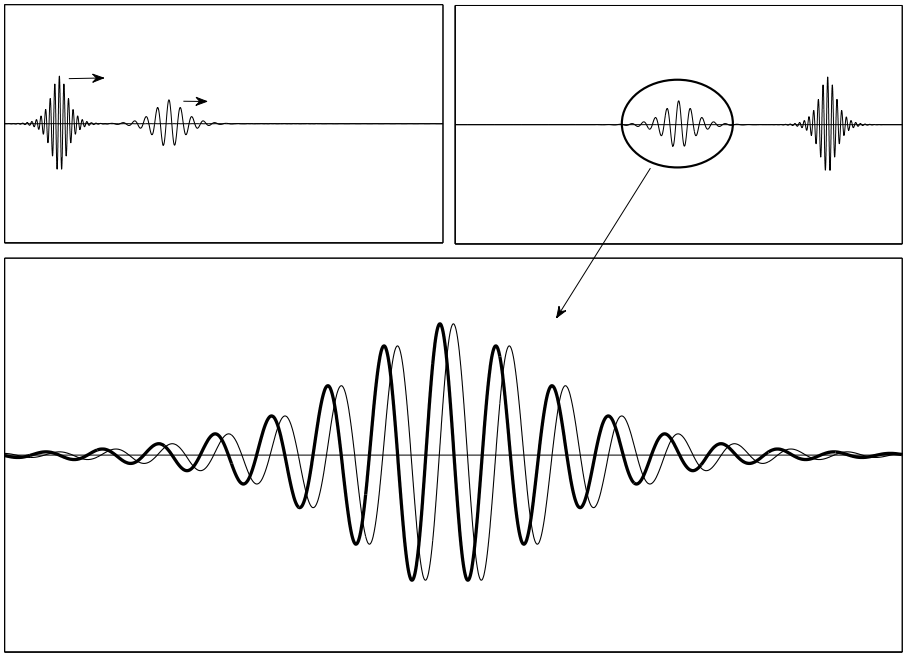

Figure 2.1: Schematic of two pulse interaction. Top left: Initial configuration of two pulses with different wavenumbers. Top right: After the pulse with the higher wavenumber has passed through the slower pulse. Bottom: zoom of the slower pulse (bold line) after interaction. The position of the pulse if no interaction had occurred is also shown (thin line).

This section summarizes how Ref. [CBSU07] was able to prove that, under certain conditions, there is almost no interaction (see Fig. 2.1) of modulated pulses with different carrier waves in the NKG equation. "Almost no interaction" means that in lowest order, the only

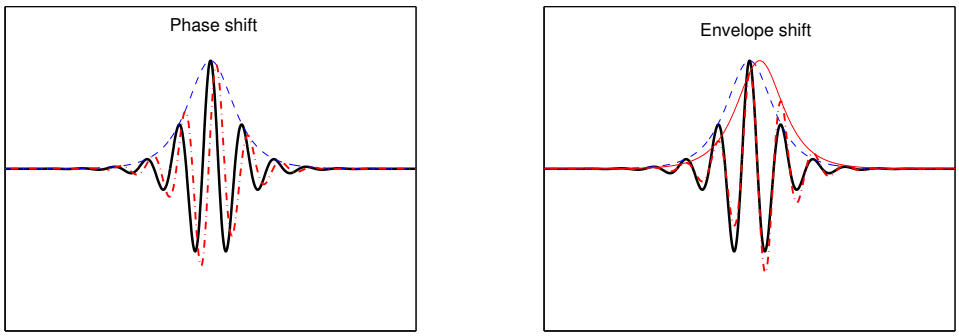

Figure 2.2: Illustration of the two types of shifts that occur due to pulse interaction. Left: For clarity, a pure *phase shift* is shown. In this case the envelope function (blue dashed line) has fixed position. The shifted carrier wave is shown as a thick solid line. For comparison, the non-shifted carrier wave is also shown (red dash-dot line). Right: A pure *envelope shift*. In this case, the position of the carrier wave (thick solid line) is fixed and the amplitudes modified by the shifted envelope function (blue dashed line). The non-shifted envelope function (thin solid line) and the corresponding unaffected carrier wave (red dash-dot line) are also shown. After interaction the modulated pulses suffer phase *and* envelope shifts.

change a pulse suffers after traveling through another pulse of a different wavelength[1] will be a small phase and envelope shift of $\mathcal{O}(\varepsilon)$, see Fig. 2.2. The estimates obtained in the previously mentioned work [PW96] were $\mathcal{O}(1)$. To show this, the following strategy is used: (a) establish what a modulated pulse is, (b) construct a single pulse approximation, (c) add two single pulse approximations with a correction for the shifts and, (d) show that the resulting two pulse approximation is close to an actual solution of the original equation. The revealing step here is (c), which assumes that the major consequence from the interaction will be an $\mathcal{O}(\varepsilon)$ phase and envelope shift. It turns out that the approximate solutions referred to in step (b) are based on the NLS equation.

2.1.1 Modulated pulse definition

Now that we have a general idea of the result and how we could prove it, we can proceed to make things more precise. We begin by formulating what a modulated pulse is. Suppose it is the superposition of plane waves,

$$u(x,t) = \int_{-\infty}^{\infty} \hat{A}(k) e^{\mathrm{i}(kx-\omega(k)t)} dk + \text{c.c.}, \tag{2.6}$$

where $\omega(k)$ is the frequency which is a function of the so-called wavenumber k. We can make the change of variables,

$$k = k_0 + \varepsilon \tilde{k}, \tag{2.7}$$

[1] As will be shown later, the wavelength (and frequency) are related to the wavenumber. These in turn define the carrier wave. Therefore, we could have also said "another pulse of a different wavenumber" or "another pulse with a different carrier wave" to mean the same thing.

where $0 < \varepsilon \ll 1$ is a small perturbation parameter and where we express $\omega(k)$ as a Taylor series centered at k_0,

$$\omega(k) = \omega_0 + \omega'\varepsilon\tilde{k} + \frac{\omega''}{2}\varepsilon^2\tilde{k}^2 + \text{h.o.t.}, \tag{2.8}$$

where $\omega_0 = \omega(k_0)$, $w' = \frac{d\omega}{dk}|_{k=k_0}$, and $w'' = \frac{d^2\omega}{dk^2}|_{k=k_0}$. Equation (2.6) can now be written as,

$$\begin{aligned} u(x,t) &= \int_{-\infty}^{\infty} \hat{A}(k_0+\varepsilon\tilde{k}) e^{\mathrm{i}((k_0+\varepsilon\tilde{k})x - (\omega_0+\omega'\varepsilon\tilde{k}+\frac{\omega''}{2}\varepsilon^2\tilde{k}^2+\mathcal{O}(\varepsilon^3))t)}\varepsilon d\tilde{k} + \text{c.c.}\,, \\ &= e^{\mathrm{i}(k_0x-\omega_0t)}\varepsilon \int_{-\infty}^{\infty} \hat{A}(k_0+\varepsilon\tilde{k}) e^{\mathrm{i}(\varepsilon(x-\omega't)\tilde{k}+\varepsilon^2t\frac{\omega''}{2}\tilde{k}^2+\mathcal{O}(\varepsilon^3)t)} d\tilde{k} + \text{c.c.}\,, \\ &= e^{\mathrm{i}(k_0x-\omega_0t)}\varepsilon \int_{-\infty}^{\infty} \hat{A}(k_0+\varepsilon\tilde{k}) e^{\mathrm{i}(X\tilde{k}+T\frac{\omega''}{2}\tilde{k}^2+\mathcal{O}(\varepsilon^3)t)} d\tilde{k} + \text{c.c.}\,, \end{aligned}$$

where $T = \varepsilon^2 t$ and $X = \varepsilon(x - ct)$ with $c = \omega'$. In the linear case, we can define a function $A(X,T)$ to represent the integral part in the above expression. This motivates the form of our ansatz,

$$u_{\text{simple pulse}}(x,t) = \varepsilon A(X,T)E + \text{c.c.}, \tag{2.9}$$

where $A(X,T)$ is a complex valued envelope function that modulates the carrier wave $E = e^{\mathrm{i}(k_0x-\omega_0t)}$, which travels with a phase velocity of $c_\text{p} = \omega_0/k_0$. The pulse can be centered arbitrarily so we could define $X = \varepsilon(x - ct - x_0)$ where x_0 is the initial *envelope shift*. An initial *phase shift* can be accounted for by taking $E = e^{\mathrm{i}(k_0x-\omega_0t-\phi)}$. Unless otherwise stated we set x_0 and ϕ to be zero. In Sec. 2.4 we will add space and time dependent shifts which account for interaction effects.

This ansatz has two scales. The function $A(X,T)$ acts on the long spatial and temporal scales which are separated from the normal scale of the carrier wave E. See Fig. 2.3 for an example. As we will see in Sec. 2.1.2, the problem is reduced to solving an equation for the function $A(X,T)$. This procedure is sometimes referred to as multiple-scale analysis.

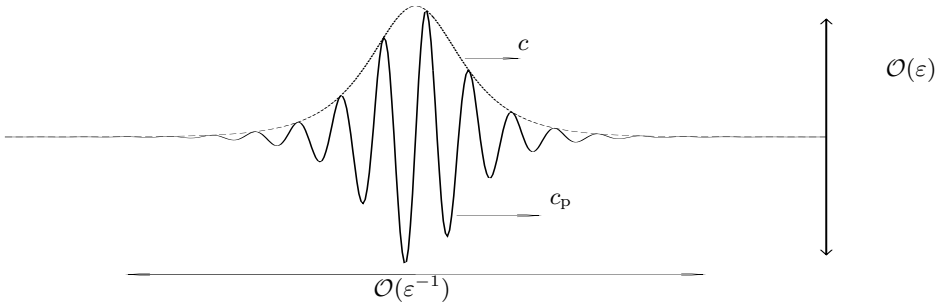

Figure 2.3: A carrier wave (solid line) modulated by an envelope (dashed line). The envelope moves with velocity c and the carrier wave with velocity c_p. The amplitude and width of the pulse are defined in terms of the small parameter ε. See text for more details.

2.1.2 Single pulse approximation

We need a way to quantify how well the approximate solution satisfies the equation. We can use the residual, which is defined as,

$$\mathrm{Res}(u) = -\partial_t^2 u + \partial_x^2 u - u + u^3, \tag{2.10}$$

where $\mathrm{Res}(u) = 0$ implies that u is an exact solution of Eq. (2.1). The residual of the modulated pulse (2.9) is,

$$\begin{aligned}\mathrm{Res}(u_{\text{simple pulse}}) &= \varepsilon(k_0^2 - \omega_0^2 + 1)AE + \varepsilon^2(\mathrm{i}k_0 - \mathrm{i}\omega_0 c)(\partial_X A)E \\ &\quad + \varepsilon^3(2\mathrm{i}\omega_0\partial_T A + (1-c^2)\partial_X^2 A + 3|A|^2 A)E \\ &\quad + \varepsilon^3 A^3 E^3 + \varepsilon^4 2c(\partial_{XT} A)E \\ &\quad - \varepsilon^5(\partial_T^2 A)E + \text{c.c.}\,.\end{aligned}$$

The εE term will vanish if the linear dispersion relation $\omega_0^2 = k_0^2 + 1$ is satisfied. Choosing the group velocity relation $c = k_0/\omega_0$ will cancel terms at $\varepsilon^2 E$. At $\varepsilon^3 E$ we find that A should satisfy,

$$2\mathrm{i}\omega_0\partial_T A + (1-c^2)\partial_X^2 A + 3|A|^2 A = 0, \tag{2.11}$$

which is a nonlinear Schrödinger equation.

We need to make some definitions and establish notation conventions (see Appendix B for a full list of notations, symbols and spaces).

Definition 2.1. The space $H^s(m)$ consists of s-times weakly differentiable functions for which $\|u\|_{H^s(m)} = \|u\rho^m\|_{H^s} = (\sum_{j=0}^s \int |\partial_x^j(u(x)\rho^m(x))|^2 dx)^{1/2}$ with $\rho(x) = \sqrt{1+x^2}$ is finite, where we do not distinguish between scalar and vector-valued functions or real- and complex-valued functions. The space C_b^s consists of s-times continuously differentiable functions for which $\|u\|_{C_b^s} = \sum_{j=0}^s \sup_{x\in\mathbb{R}} |\partial_x^j u(x)|$ is finite. We sometimes write, e.g., $\|u(x)\|_{C_b^s}$ for the C_b^s-norm of the function $x \mapsto u(x)$. The possibly different constants which can be chosen independently of ε are denoted by C.

The formal order $\mathcal{O}(\varepsilon^3)$ corresponds to the variables X and T. When expressed in terms of the variables x, t (which correspond to the scale of the NKG equation) a factor of $\varepsilon^{1/2}$ is lost due to the way the L^2 norm scales in terms of ε. Therefore,

$$||\mathrm{Res}(u_{\text{simple pulse}})||_{H^s} \leq C\varepsilon^{5/2}.$$

We choose $A(X,T)$ to be a time periodic solution in H^s of the NLS equation (2.11),

$$A(X,T) = \tilde{A}(X)e^{-i\gamma T}, \tag{2.12}$$

where $\gamma \in \mathbb{R}$ and $\tilde{A} \in \mathbb{R}$ satisfy the second order differential equation,

$$\partial_X^2 \tilde{A} = C_1\tilde{A} + C_2\tilde{A}^3, \tag{2.13}$$

with $C_1 = -2\gamma\omega_0/(1-c^2)$, $C_2 = 3/(1-c^2)$. Since we choose $\omega_0 > 0$, this equation has two homoclinic solutions for $\gamma < 0$,

$$\tilde{A}_{\text{simple pulse}}(X) = \pm\left(\frac{2C_1}{C_2}\right)^{1/2} \mathrm{sech}\,(C_1^{1/2}X). \tag{2.14}$$

By definition of the hyperbolic secant, we also have,

$$|\tilde{A}_{\text{simple pulse}}(X)| \leq Ce^{-r|X|}, \qquad r = \sqrt{C_1} = \sqrt{\frac{-2\gamma\omega_0}{1-c^2}}. \tag{2.15}$$

Remark 2.2. Solutions of the form given in (2.12) with $\tilde{A}$ given by (2.14) are called NLS 1-solitons.

The approximation has the form,

$$u_{\text{simple pulse}}(x,t) = v(x-ct, k_0x - \omega t), \tag{2.16}$$

with

$$v(\xi, y) = \varepsilon\tilde{A}_{\text{simple pulse}}(\varepsilon\xi)e^{iy} + \text{c.c.}\ , \tag{2.17}$$

where $\omega = \omega_0 + \varepsilon^2\gamma$. The function v is 2π periodic in its second argument and satisfies $\lim_{\xi\to\pm\infty} v(\xi, y) = 0$ (due to Eq. 2.15). Functions with these two properties are called moving *breathers*. It was shown in Refs. [BMW94,SK87,Den93] that Eq. (2.1) has no breather solutions. However, for single pulse approximations we can compute approximate breather solutions which make the residual arbitrarily small in terms of powers of ε.

Making use of γ in the ansatz could allow us more freedom to make the residual small. Additionally, we can take higher order terms to define a new ansatz,

$$u_{\text{pulse}}(x,t) = \varepsilon A_1E + \varepsilon^3A_3E^3 + \varepsilon^5A_5E^5 + \text{c.c.}, \tag{2.18}$$

where the A_j depend on the variable $X = \varepsilon(x-ct)$ and we redefine $E = e^{\mathrm{i}(k_0x-\omega t)}$ where $\omega = \omega_0 + \varepsilon^2\gamma$. We can make the residual three orders smaller for this ansatz if the following equations are satisfied,

$$\omega_0^2 = k_0^2 + 1, \tag{2.19}$$

$$c = \frac{k_0}{\omega}, \tag{2.20}$$

$$A_5 = \frac{3A_3A_1^2}{25\omega^2 - 25k_0^2 - 1}, \tag{2.21}$$

$$A_3 = -\alpha A_1^3 + \varepsilon^2\alpha^2((1-c_g^2)\partial_X^2A_1^3 + 6A_1^3|A_1|^2), \tag{2.22}$$

$$0 = (1-c^2)\partial_X^2A_1 + 2\omega_0\gamma A_1 + 3A_1|A_1|^2 + \varepsilon^2(\gamma^2A_1 - 3\alpha|A_1|^4A_1), \tag{2.23}$$

where $\alpha = (9\omega^2 - 9k_0^2 - 1)^{-1}$. Equation (2.19) represents the linear dispersion relation and Eq. (2.20) represents the group velocity. The difference between this group velocity and that for $u_{\text{simple pulse}}$ is an $\mathcal{O}(\varepsilon^2)$ correction (since ω is used in place of ω_0). Equation (2.23) is a cubic-quintic NLS equation and has two homoclinic solutions [MGDM05, PPT79],

$$A_1^2 = \frac{24C_1}{C_2(6 + 2\sqrt{9 - 48C_1C_3/C_2^2}\cosh(2\sqrt{C_1}x)}, \tag{2.24}$$

for,

$$\alpha, \gamma < 0, \qquad \frac{C_1C_3}{C_2^2} < \frac{16}{3},$$

where $C_1 = -(2\gamma\omega_0 + \varepsilon^2\gamma^2)/(1-c^2)$, $C_2 = 3/(1-c^2)$ and $C_3 = 3\alpha\varepsilon^2/(1-c^2)$. The condition $C_1C_3/C_2^2 < 16/3$ is satisfied for ε sufficiently small. The functions A_3 and A_5 follow once A_1 is determined due to the recursive nature of the equations. Since $0 < \varepsilon \ll 1$, Eq. (2.23) can also be viewed as a small perturbation of the differential equation (2.13), which has solutions given by Eq. (2.14) with the group velocity $c = k_0/\omega$. Expressing the solution as a moving breather yields,

$$u_{\text{pulse}}(x,t) = v(x - ct, k_0 x - \omega t), \tag{2.25}$$

with

$$\begin{aligned} v(\xi, y) &= \varepsilon A_1(\varepsilon\xi)e^{iy} + \varepsilon^3 A_3(\varepsilon\xi)e^{3iy} + \varepsilon^5 A_5(\varepsilon\xi)e^{5iy} + \text{c.c.} && (2.26)\\ &= \varepsilon\tilde{A}_{\text{pulse}}(\varepsilon\xi)e^{iy} + \mathcal{O}(\varepsilon^3 e^{-r\varepsilon|\xi|}) + \text{c.c.} && (2.27)\end{aligned}$$

where $\tilde{A}_{\text{pulse}}$ corresponds to the homoclinic solution of Eq. (2.13) with $c = k_0/\omega$ and with r defined in Eq. (2.15). We can make the more precise statement:

Lemma 2.3. *Let $s \geq 2$, $k_0 > 0$. For sufficiently small $\varepsilon > 0$ there exists a two-dimensional family of approximate modulating pulse solutions to* (2.1) *of the form*

$$u(x,t) = v(x - ct + x_0, k_0 x - \omega t + \phi),$$

parametrized by the initial envelope shift $x_0 \in \mathbb{R}$ and initial phase shift $\phi \in [0, 2\pi)$, where v is 2π-periodic in its second argument, $\omega = \omega_0 + \gamma\varepsilon^2$ and $c = k_0/\omega$. Moreover,

$$v(\xi, y) = \varepsilon\tilde{A}_{\text{pulse}}(\varepsilon\xi)e^{iy} + \mathcal{O}(\varepsilon^3 e^{-r\varepsilon|\xi|}) + \text{c.c.}$$

The residual fulfills,

$$||\text{Res}(u_{\text{pulse}})||_{H^s} \leq C\varepsilon^{11/2}.$$

Proof. This is Ref. [CBSU07, Lemma 3.1]. The proof follows the basic idea highlighted above.

□

2.1.3 Two pulse approximation

Now that we have constructed single pulse approximations we can pose a two pulse ansatz,

$$\begin{aligned} u_{\text{two pulse}}(x,t) =& \varepsilon A_1 E + \varepsilon^3 A_3 E^3 + \varepsilon^5 A_5 E^5 + \varepsilon B_1 F + \varepsilon^3 B_3 F^3 + \varepsilon^5 B_5 F^5 \\ &+ \varepsilon^3 Y_A E + \varepsilon^3 Y_B F + \varepsilon^3 M_{\text{mixed}} + \text{c.c.}\,, \end{aligned} \tag{2.28}$$

where,

$$\begin{aligned} M_{\text{mixed}} &= M_{\text{mixed}}(A_1, A_3, A_5, B_1, B_3, B_5, Y_A, Y_B, E, F)\\ E &= \exp\left(\text{i}(k_A x - \omega_A t + \varepsilon\Omega_A(X_B))\right),\\ F &= \exp\left(\text{i}(k_B x - \omega_B t + \varepsilon\Omega_B(X_A))\right),\\ A_j &= A_j(X_A), \quad B_j = B_j(X_B), \quad Y_A = Y_A(X_A, T), \quad Y_B = Y_B(X_B, T),\\ X_A &= \varepsilon(x - c_A t - x_A), \quad X_B = \varepsilon(x - c_B t - x_B), \end{aligned}$$

and the parameters have adopted the appropriate subscripts. The first line in ansatz (2.28) is the sum of two single pulses as seen in Eq. (2.18), with modified coordinates. The second line is also necessary to eliminate terms in the residual. The term M_{mixed} accounts for the mixed frequencies resulting from the nonlinear term. The expressions Ω_A and Ω_B in the two pulse ansatz represent space dependent phase shift *corrections* of pulse A and B respectively. We assume that the wavenumbers satisfy $k_A > k_B$ and that the initial envelope shifts satisfy $x_A < x_B$ such that pulse A will travel through pulse B. Fig. 2.1 shows an example of two pulse evolution.

Trying to make $\text{Res}(u_{\text{two pulse}})$ small we find linear dispersion and group velocity relations analogous to those for u_{pulse},

$$\omega_{A,0}^2 = k_A^2 + 1, \quad \omega_{B,0}^2 = k_B^2 + 1, \tag{2.29}$$

$$c_A = \tfrac{k_A}{\omega_A}, \quad c_B = \tfrac{k_B}{\omega_B}, \tag{2.30}$$

where $\omega_A = \omega_{A,0} + \varepsilon^2\gamma$ and likewise for ω_B. The following equations must also be satisfied,

$$\begin{aligned} 2\omega_{A,0}A_1 + (1-c_A^2)\partial_1^2 A_1 + 3|A_1|^2 A_1 + \big(2\omega_A(c_A - c_B)\partial_1\Omega_A + 6|B_1|^2\big) \\ + \varepsilon^2(\gamma^2 A_1 - 3\alpha|A_1|^4 A_1) = 0, \end{aligned} \tag{2.31}$$

$$\begin{aligned} 2\omega_{B,0}B_1 + (1-c_B^2)\partial_1^2 B_1 + 3|B_1|^2 B_1 + \big(2\omega_B(c_B - c_A)\partial_1\Omega_B + 6|A_1|^2\big) \\ + \varepsilon^2(\gamma^2 B_1 - 3\beta|B_1|^4 B_1) = 0, \end{aligned} \tag{2.32}$$

where $\alpha = (9\omega_A^2 - 9k_A^2 - 1)^{-1}$ and $\beta = (9\omega_B^2 - 9k_B^2 - 1)^{-1}$. The notation ∂_j means differentiation with respect to the jth argument. If we define the phase shift corrections as,

$$\Omega_A(X_B) = \int^{X_B} \frac{3|B_1(\zeta)|^2}{\omega_A(c_A - c_B)}\, d\zeta + \Omega_A^0, \tag{2.33}$$

$$\Omega_B(X_A) = \int^{X_A} \frac{3|A_1(\zeta)|^2}{\omega_B(c_B - c_A)}\, d\zeta + \Omega_B^0, \tag{2.34}$$

where Ω_A^0 and Ω_B^0 are constants which normalize the initial phases, then Eqs. (2.31) and (2.32) become ODEs analogous to Eq. (2.23),

$$\begin{aligned} 0 &= 2\omega_{A,0}A_1 + (1-c_A^2)\partial_1^2 A_1 + 3|A_1|^2 A_1 + \varepsilon^2(\gamma^2 A_1 - 3\alpha|A_1|^4 A_1), \\ 0 &= 2\omega_{B,0}B_1 + (1-c_B^2)\partial_1^2 B_1 + 3|B_1|^2 B_1 + \varepsilon^2(\gamma^2 B_1 - 3\beta|B_1|^4 B_1). \end{aligned}$$

Similarly, the functions A_3,A_5 and B_3,B_5 are analogous to those in Eqs. (2.21) and (2.22). Thus we have explicit expressions for all the terms in the first line of Eq. (2.28). It turns out that the functions Y_A and Y_B must satisfy linear Schrödinger equations and the determining equations for M_{mixed} are algebraic. See [CBSU07, Sec. 4.2] for the exact expressions. Thus, the ansatz $u_{\text{two pulse}}$ is really just the sum of two different pulses defined by u_{pulse} with a *small* space dependent phase correction. In other words,

$$u_{\text{two pulse}}(x,t) = \Psi(x,t) + \varepsilon^3 h(x,t), \tag{2.35}$$

where $h(x,t)$ represents terms in the second line of the two pulse ansatz (2.28) and,

$$\begin{aligned} \Psi(x,t) &= v_A(x - c_A t + x_A, k_A x - \omega_A t + \varepsilon\Omega_A) \\ &\quad + v_B(x - c_B t + x_B, k_B x - \omega_B t + \varepsilon\Omega_B), \end{aligned} \tag{2.36}$$

where $v_A(\xi, y)$ and $v_B(\xi, y)$ are the breathers defined by Eq. (2.26) with the parameters satisfying Eqs. (2.29) and (2.30). A result similar to Lemma 2.3 for the residual holds in the two pulse case:

Lemma 2.4. *Let $s \geq 2$, $k_A, k_B > 0$, $k_A \neq k_B$, $\gamma_A, \gamma_B < 0$, $x_A, x_B \in \mathbb{R}$, and $T_0 > 0$. There exist $\varepsilon_0 > 0$ and $C_1, C_2 > 0$ such that for all $\varepsilon \in (0, \varepsilon_0)$ the approximation u_{twopulse} satisfies,*

$$\|h(\cdot, t)\|_{C_b^{s-1}} \leq C_1, \tag{2.37}$$

and

$$\sup_{t \in [0, T_0/\varepsilon^2]} \|\text{Res}(u_{\text{twopulse}})\|_{H^s} \leq C_2 \varepsilon^{11/2}. \tag{2.38}$$

Proof. We have already shown that the residual vanishes formally up to $\mathcal{O}(\varepsilon^6)$. Other details, such as the equation for Y_A and Y_B and showing that $h(x, t)$ is $\mathcal{O}(1)$ bounded on the time scale $\mathcal{O}(1/\varepsilon^2)$, can be found in [CBSU07, Sec. 4.2]. □

2.1.4 Justification of the two pulse approximation

Up until now, we have shown that our approximate pulses have a small residual. We now make an estimate on the order of the approximation:

Lemma 2.5. *Under the assumptions of Lemma 2.4 there exist $\varepsilon_0 > 0$ and $C_1, C_2 > 0$ such that for all $\varepsilon \in (0, \varepsilon_0)$ the following holds: if*

$$\|u(x, 0) - u_{\text{twopulse}}(x, 0)\|_{H^s} + \|\partial_t u(x, 0) - \partial_t u_{\text{twopulse}}(x, 0)\|_{H^{s-1}} \leq C_1 \varepsilon^{7/2}, \tag{2.39}$$

where Ω_A, Ω_B are given by (2.33),(2.34), then

$$\sup_{t \in [0, T_0/\varepsilon^2]} \|u(x, t) - u_{\text{twopulse}}(x, t)\|_{C_b^{s-1}} \leq C_2 \varepsilon^{7/2}. \tag{2.40}$$

Proof. See [CBSU07, Sec. 4.3]. One needs that the residual is small (see Lemma 2.4), which requires the envelope functions are time independent (NLS 1-solitons). The estimate can be shown using energy estimates and Gronwall's inequality. This strategy was first introduced in [KSM92]. □

Since the proof makes a number of estimates, it is not clear if a better estimate is possible. Also, it was only possible to obtain the estimate for $t \in [0, T_0/\varepsilon^2]$ where T_0 is the natural time scale of the NLS equation. We can choose T_0 as large as we wish, but this in turn will require ε_0 to be smaller. We explore these issues numerically in Sec. 2.3.

We express the preceding estimate of the approximate solution u_{twopulse} in terms of the associated breather solution:

Theorem 2.6. *Under the assumptions of Lemma 2.4 there exist $\varepsilon_0 > 0$ and $C_1, C_2 > 0$ such that for all $\varepsilon \in (0, \varepsilon_0)$ the following holds: if*

$$\|u(x, 0) - \Psi(x, 0)\|_{H^s} + \|\partial_t u(x, 0) - \partial_t \Psi(x, 0)\|_{H^{s-1}} \leq C_1 \varepsilon^{7/2}, \tag{2.41}$$

where Ω_A, Ω_B are given by (2.33),(2.34), then

$$\sup_{t \in [0, T_0/\varepsilon^2]} \|u(x, t) - \Psi(x, t)\|_{C_b^{s-1}} \leq C_2 \varepsilon^3. \tag{2.42}$$

Proof. An application of the triangle inequality,

$$\|u - \Psi\|_{H^s} \leq \|u - u_{\text{twopulse}}\|_{H^s} + \|u_{\text{twopulse}} - \Psi\|_{H^s}$$

along with Eqs. (2.40) and (2.37) and the Sobolev embedding theorem $H^s \subset C_b^{s-1}$ yields the result. □

The final statement of Ref. [CBSU07] transfers Theorem 2.6 to an envelope shift estimate by supposing that the error comes from a shift of the envelope and noting that,

$$\varepsilon g(\varepsilon(x + \varepsilon a)) - \varepsilon g(\varepsilon x) = \varepsilon g'(\varepsilon x)\varepsilon^2 a + \mathcal{O}(\varepsilon(\varepsilon^2 a)^2) = \mathcal{O}(\varepsilon^3). \tag{2.43}$$

Thus, even if the error is only due to the envelope shift, it can be at most $\mathcal{O}(\varepsilon)$.

Summary

Assuming the terms and parameter are chosen such that $\text{Res}(u_{\text{two pulse}})$ is small enough, which requires that A_1 and B_1 are NLS 1-solitons, and that the initial data is small enough, then,

(i) $\sup_{t\in[0,T_0/\varepsilon^2]} \|u(x,t) - \Psi(x,t)\|_{C_b^{s-1}} = \mathcal{O}(\varepsilon^3)$ (from Theorem 2.6),
(ii) the phase shift is at most $\mathcal{O}(\varepsilon)$ (since Ω is independent of ε),
(iii) the envelope shift is at most $\mathcal{O}(\varepsilon)$ (from Eq. (2.43)).

In the next section, various numerical methods are presented to solve Eq. (2.1). In Sec. 2.3 those numerical methods are used to confirm Theorem 2.6 and to show that A_1 and B_1 *do not* have to be NLS 1-solitons in order to obtain (i) - (iii) and that these results are indeed the best we can achieve, which is not discernable from the theorem alone.

2.2 Numerical integrators

One of the tools used in the previous section to obtain accurate approximate solutions was multiple-scale analysis. By exploiting the multiple-scale character of the problem, the main task was reduced to solving equations (like the NLS equation) on the slow scales X and T. Thus, for small ε the dimension of the problem in numerical simulations is dramatically reduced[2]. However, in order to conduct the numerical investigation, the *full* problem (2.1) must be solved. This section is dedicated to the numerical integrators used to solve Eq. (2.1). Choice of the scheme and its implementation is important due to the large problem size. We use (a) a finite difference scheme (leapfrog), (b) a method of lines, (c) an implicit pseudo-spectral method and (d) a geometric pseudo-spectral method.

There are no known exact solutions of Eq. (2.1) that are useful[3] to test the integrity of the integrators. The use of multiple solvers helps to compensate for this. Additionally, convergence of the leapfrog scheme is proved. Although a comprehensive comparison of the schemes is not carried out, we do mention our observations in terms of performance.

[2]If the same step sizes are taken in both systems then the factor is 10^6 (in x) for $\varepsilon = .01$.
[3]There are known exact solutions to Eq. (2.1), but they are unbounded, see [PZ04, Sec. 3.1].

We start by restating Eq. (2.1) as the initial value-boundary problem,

$$\partial_t^2 u - \partial_x^2 u + u - u^3 = 0, \tag{2.44}$$

$$u(\cdot, 0) = U_0, \tag{2.45}$$

$$u_t(\cdot, 0) = U_1, \tag{2.46}$$

$$u(-a, \cdot) = u(a, \cdot), \tag{2.47}$$

$$\partial_x u(-a, \cdot) = \partial_x u(a.\cdot), \tag{2.48}$$

in the domain $D = \{(x,t) \,|\, (x,t) \in [-a,a] \times [0,\tau]\}, a, \tau \in \mathbb{R}$, which is well-posed (see [Tao06, Sec. 3.3]). We assume equally spaced temporal and spatial meshes so that for arbitrary integers m and n we define $(x_m, t_n) = (m\Delta x, n\Delta t)$ where $\Delta x, \Delta t \ll 1$ represent the spatial and temporal spacings respectively. Let M and N represent the number of spatial and temporal points respectively.

2.2.1 Leapfrog

We obtain the so-called *leapfrog* scheme by replacing the derivatives of Eq. (2.1) with central difference approximations. This method is often used for nonlinear Klein-Gordon equations like Eq. (2.1) and those with other nonlinearities (cf. [DJ89, AKL79, BRI05, Agr01]). A more complete description of finite difference methods like the leapfrog scheme can be found in Refs. [Str04, Tho95]. For Eq. (2.1) the scheme is,

$$\frac{u_m^{n+1} + u_m^{n-1} - 2u_m^n}{\Delta t^2} - \frac{u_{m+1}^n + u_{m-1}^n - 2u_m^n}{\Delta x^2} + u_m^n - (u_m^n)^3 = 0, \tag{2.49}$$

where $u_m^n = u(x_m, t_n)$. We can rearrange the above equation to obtain an explicit formula to advance one step in time,

$$u_m^{n+1} = \Delta t^2 \left(\frac{u_{m+1}^n + u_{m-1}^n - 2u_m^n}{\Delta x^2} - u_m^n + (u_m^n)^3 \right) - u_m^{n-1} + 2u_m^n. \tag{2.50}$$

In order to start the computation we need the first two time levels. Using the initial value (2.45), we can define,

$$u_m^0 = U_0(x_m).$$

The Taylor series expansion of $u(x,t)$ centered at $t = 0$ and evaluated at $t = \Delta t$,

$$u(x, \Delta t) = u(x,0) + u_t(x,0)\Delta t + u_{tt}(x,0)\frac{\Delta t^2}{2} + \mathcal{O}(\Delta t^3), \tag{2.51}$$

along with Eqs. (2.44)-(2.46) can be used to compute the next time level,

$$u_m^1 = U_0(x_m) + U_1(x_m)\Delta t + \left(\frac{u_{m+1}^0 + u_{m-1}^0 - 2u_m^0}{\Delta x^2} + u_m^0 - \left(u_m^0\right)^3 \right) \frac{\Delta t^2}{2}. \tag{2.52}$$

Remark 2.7. We use the notation u_m^n when witting down the numerical schemes. When referring to the numerical solution, we write $\tilde{u}_m^n$. We drop the tilde for notational simplicity if the meaning is clear.

We measure the numerical solution using the norms,

$$\|u^n\|_{\Delta x} = \left(\Delta x \sum_m |u_m^n|^2\right)^{1/2}, \qquad \|u^n\|_{l^\infty} = \sup_m |u_m^n|. \tag{2.53}$$

To show that the above scheme is convergent we will use the following computational lemma:

Lemma 2.8. *If $a, b > 0$ and $\{x_n\}_{n\leq N}$ is a sequence satsifying $x_0 \geq -b/a$, and*

$$x_{n+1} \leq (1+a)x_n + b, \tag{2.54}$$

then,

$$x_N \leq e^{Na}\left(x_0 + \frac{b}{a}\right) - \frac{b}{a}. \tag{2.55}$$

Proof. Iterating Eq. (2.54) N times is a convergent geometric series. This, along with the coarse estimate $(1+x)^n \leq e^{nx}$ for $x \geq -1, n > 0$ yields Eq. (2.55). □

Theorem 2.9. *Let $s > 4$ and fix U_0 and U_1. Then for the solution $u \in C([0,T_0], H^s)$ of the initial-boundary value problem* (2.44) *there exists a $C > 0$ and a $\Delta x_0 > 0$ such that for all $\Delta x \in (0, \Delta x_0)$ the numerical solution $\tilde{u}$ of Eq.* (2.49) *with $\tilde{u}_m^0 = u(x_m, t_0) = U_1(x)$ and $\tilde{u}_m^1$ given by* (2.52) *satisfies,*

$$\sup_{n\leq N} \|u(x_m, t_n) - \tilde{u}_m^n\|_{\Delta x} \leq C\Delta x^2, \tag{2.56}$$

where $N = \mathcal{O}(\Delta t^{-2})$ is the number of temporal steps and $\Delta t/\Delta x < 1$ is held constant.

Proof. Define the residual as,

$$\mathrm{Res}_{n,m} = -u_m^{n+1} + \Delta t^2\left(\frac{u_{m+1}^n + u_{m-1}^n - 2u_m^n}{\Delta x^2} - u_m^n + (u_m^n)^3\right) - u_m^{n-1} + 2u_m^n. \tag{2.57}$$

Then for u solving Eq. (2.44) we have

$$\mathrm{Res}_{n,m} = \mathcal{O}(\Delta t^2(\Delta x^2 + \Delta t^2)). \tag{2.58}$$

Fixing $\Delta t = \mathcal{O}(\Delta x)$ we get $\mathrm{Res}_{n,m} = \mathcal{O}(\Delta x^4)$. We define the error η_m^n such that,

$$\tilde{u}_m^n = u(x_m, t_n) + \eta_m^n. \tag{2.59}$$

We find,

$$\eta_m^{n+1} = L\eta_m^n + N(\eta_m^n) + \mathrm{Res}_{n,m}, \tag{2.60}$$

where the linear part is defined as,

$$L\eta_m^n = \Delta t^2\left(\frac{\eta_{m+1}^n + \eta_{m-1}^n - 2\eta_m^n}{\Delta x^2} - \eta_m^n\right) - \eta_m^{n-1} + 2\eta_m^n, \tag{2.61}$$

and the nonlinear part as

$$N(\eta_m^n) = \Delta t^2(3(u_m^n)^2\eta_m^n + 3u_m^n(\eta_m^n)^2 + (\eta_m^n)^3). \tag{2.62}$$

For $\Delta t/\Delta x < 1$ the linear problem ($N = 0$) is convergent (see [Str04, Theorem 10.7.1]). Thus we can write,

$$\|\eta^{n+1}\|_{\Delta x} \leq \|\eta^n\|_{\Delta x} + \|N(\eta^n)\|_{\Delta x} + \|\mathrm{Res}_m\|_{\Delta x}. \tag{2.63}$$

We know,

$$\begin{aligned}\sup_m |u_m| &\leq \sum_m (\Delta x)^{-1/2}|u_m|(\Delta x)^{1/2},\\ &\leq \left(\sum_m (\Delta x)^{-1}\right)^{1/2}\left(\sum_m \Delta x|u_m|^2\right)^{1/2},\\ &\leq \mathcal{O}(\Delta x^{-1})\|u\|_{\Delta x},\end{aligned}$$

where the number of spatial points $M = \mathcal{O}(\Delta x^{-1})$. Thus we have the inequalities,

$$\|u^n u^n \eta^n\|_{\Delta x} \leq \|u^n\|_{l^\infty}^2 \|\eta^n\|_{\Delta x}, \tag{2.64}$$

$$\|u^n \eta^n \eta^n\|_{\Delta x} \leq \|u^n\|_{l^\infty} \mathcal{O}(\Delta x^{-1})\|\eta^n\|_{\Delta x}^2, \tag{2.65}$$

$$\|(\eta^n)^3\|_{\Delta x} \leq \mathcal{O}(\Delta x^{-2})\|\eta^n\|_{\Delta x}^3. \tag{2.66}$$

Additionally, there are constants C_1, C_2 and C_{Res} such that $\|u(\cdot,t)\|_{l^\infty} \leq C_1$, $\|u(\cdot,t)\|_{l^\infty}^2 \leq C_2$ and $\|\mathrm{Res_m}\|_{\Delta x} \leq C_{\mathrm{Res}}\Delta x^4$. Using the solution bounds and (2.64)-(2.66), Eq. (2.63) becomes,

$$\|\eta^{n+1}\|_{\Delta x} \leq \|\eta^n\|_{\Delta x} + \Delta t^2(C_1\|\eta^n\|_{\Delta x} + C_2\Delta x^{-1}\|\eta^n\|_{\Delta x}^2 + \Delta x^{-2}C_3\|\eta^n\|_{\Delta x}^3) + C_{\mathrm{Res}}\Delta x^4,$$

where the constant from the big O in Eqs. (2.65) and (2.66) have been absorbed by C_2 and C_3. For the moment, let us assume

$$C_2\Delta x^{-1}\|\eta^n\|_{\Delta x} + C_3\Delta x^{-2}\|\eta^n\|_{\Delta x}^2 < 1. \tag{2.67}$$

Then,

$$\|\eta^{n+1}\|_{\Delta x} \leq \left(1 + \Delta t^2(C_1+1)\right)\|\eta^n\|_{\Delta x} + C_{\mathrm{Res}}\Delta x^4. \tag{2.68}$$

Using Lemma 2.8 we have,

$$\|\eta^N\|_{\Delta x} \leq \frac{C_{\mathrm{Res}}\Delta x^2}{C_4^2(C_1+1)}e^{N\Delta t^2\Delta x^2(C_1+1)} - \frac{C_{\mathrm{Res}}\Delta x^2}{C_4^2(C_1+1)}, \tag{2.69}$$

where $\Delta t/\Delta x = C_4 < 1$. If we fix $N = \mathcal{O}(\Delta t^{-2})$ all terms are bounded and there is a C such that,

$$\|\eta^N\|_{\Delta x} \leq C\Delta x^2. \tag{2.70}$$

Assumption (2.67) holds for Δx sufficiently small since,

$$C_2\Delta x^{-1}\|\eta^n\|_{\Delta x} + C_3\Delta x^{-2}\|\eta^n\|_{\Delta x}^2 \leq C_2C\Delta x + C_3\Delta x^2 C.$$

□

Besides knowing that the numerical solutions converge to the actual solutions of the initial value-boundary problem (2.44) as the spatial step size is decreased, it also formally connects Secs. 2.1 and 2.3. Suppose we are interested in showing some ε dependent approximation $\Psi = \Psi(x,t;\varepsilon)$ is $\mathcal{O}(\varepsilon^\beta)$ accurate, we can take $\Delta x \leq \varepsilon^\beta$ so that,

$$\sup_{n\leq N} \|u(x_m,t_n) - \Psi(x_m,t_n)\|_{l^\infty} \leq \sup_{n\leq N} \|u(x_m,t_n) - \tilde{u}_m^n\|_{l^\infty} + \|\tilde{u}_m^n - \Psi(x_m,t_n)\|_{l^\infty}. \tag{2.71}$$

In Sec. 2.3 we estimate $\sup_{n\leq N} \|\tilde{u}_m^n - \Psi(x_m,t_n)\|_{l^\infty}$ by making the computations for $\varepsilon \to 0$ and Theorem 2.9 addresses $\sup_{n\leq N} \|u(x_m,t_n) - \tilde{u}_m^n\|_{l^\infty}$. However we do not compare $\|u(x_m,t_n) - \Psi(x_m,t_n)\|_{l^\infty}$ and $\|u(x_m,t_n) - \Psi(x_m,t_n)\|_{H^s}$ and so inequality (2.71) only connects the two types of estimates heuristically.

2.2.2 Method of lines

In the *method of lines* all but one dimension is discretized (typically the spatial dimensions) and the resulting system of ordinary differential equations (ODEs) is integrated [Sch91]. This method is advantageous since it allows us to use packaged ODE software. Discretizing the spatial dimension of the NKG system (2.2) with a central difference yields the system of ODEs,

$$\begin{aligned} \partial_t u_m &= v_m \\ \partial_t v_m &= \frac{u_{m+1} + u_{m-1} - 2u_{m+1}}{\Delta x^2} - u_m + u_m^3, \end{aligned}$$

where $u_m = u_m(x_m,t)$ and $v_m = v_m(x_m,t)$. The above ODE system can be solved using a Runge-Kutta method like the one implemented in the *ode45* MATLAB routine.

2.2.3 Implicit pseudo-spectral method

Again we consider system (2.2). This method is in the same spirit as the method of lines described above since the discretization is not the same in every dimension. Along the spatial dimension we use a *pseudo-spectral* (PS) discretization which is done by approximating a solution $u(x,t)$ by a finite sum of known continuous functions [GO77]. We choose the Fourier series due to the availability of efficient FFT routines. This in turn reduces the PDEs into a system of ODEs. Following Ref. [WMGS91], we use a Crank-Nicolson finite difference stencil for the temporal discretization. The linear part is computed in the Fourier domain while the nonlinear part is computed in the spatial domain.

For simplicity we first assume $x \in [-\pi,\pi]$ and later show the scaling that extends this to general intervals. We consider equidistant collocation points $x_m = m\Delta x$ for $m = -M/2, ..., M/2-1$, where the spatial step size is $\Delta x = 2\pi/M$.

We start by stating the discrete Fourier transform,

$$\mathcal{F}_M[u](k) = \sum_{m=-M/2}^{M/2-1} u_m e^{-\mathrm{i}kx_m},$$

where $u_m = u(x_m,t)$. The M subscript of $\mathcal{F}_M$ indicates that the transform is discrete and is taken with M points. This transform allows us to define the functions in the Fourier domain,

$$\hat{u}_k \equiv \mathcal{F}_M[u](k), \qquad \hat{v}_k \equiv \mathcal{F}_M[v](k).$$

The inverse discrete Fourier transform is given by,

$$\mathcal{F}_M^{-1}[\hat{u}](m) = \frac{1}{M}\sum_{k=-M/2}^{M/2-1} \hat{u}_k e^{\mathrm{i}kx_m},$$

which allows us to return to the spatial domain,

$$u_m = \mathcal{F}_M^{-1}[\hat{u}](m), \qquad\qquad v_m = \mathcal{F}_M^{-1}[\hat{v}](m).$$

Substituting this into system (2.2) gives us the conditions for each Fourier coefficient to satisfy,

$$\begin{cases} \partial_t \hat{u}_k &= \hat{v}_k, \\ \partial_t \hat{v}_k &= \mathcal{L}(k)\hat{u}_k + \mathcal{N}(\hat{u})(k), \end{cases} \tag{2.72}$$

where the dispersion relation is,

$$\mathcal{L}(k) = -(k^2+1), \tag{2.73}$$

where k is the spectral variable and the nonlinear part is defined as,

$$\mathcal{N}(\hat{u})(k) = \mathcal{F}_M[\left(\mathcal{F}_M^{-1}[\hat{u}]\right)^3](k). \tag{2.74}$$

We immediately see the advantage of representing the variables in Fourier space. The differential operator has been reduced to a multiplication, as seen in the operator $\mathcal{L}(k)$.

Eigenvalues of the linear problem extend to a maximum modulus of $\mathcal{O}(\Delta t^3)$. This poses a restriction of the step size for explicit methods [WMGS91]. The time step restriction can be avoided if we use an implicit method. Applying the Crank-Nicolson stencil to each equation yields,

$$\hat{u}^{n+1} = \hat{u}^n + \frac{\Delta t}{2}\left[\hat{v}^{n+1} + \hat{v}^n\right], \tag{2.75}$$

$$\hat{v}^{n+1} = \hat{v}^n + \frac{\Delta t}{2}\left[\mathcal{L}\hat{u}^{n+1} + \mathcal{N}(\hat{u}^{n+1}) + \mathcal{L}\hat{u}^n + \mathcal{N}(\hat{u}^n)\right], \tag{2.76}$$

where the dependence on k has been dropped for notional simplicity. Substituting (2.76) into (2.75) gives us an implicit expression for $\hat{u}^{n+1}$,

$$\hat{u}^{n+1} = \hat{u}^n + \frac{\Delta t}{2}\left[2\hat{v}^n + \frac{\Delta t}{2}\left(\mathcal{L}\hat{u}^{n+1} + \mathcal{N}(\hat{u}^{n+1}) + \mathcal{L}\hat{u}^n + \mathcal{N}(\hat{u}^n)\right)\right].$$

The linear operator $\mathcal{L}$ can be inverted explicitly, which allows us to rewrite the above equation as,

$$\hat{u}^{n+1} = \left[1 - \frac{\Delta t^2}{4}\mathcal{L}\right]^{-1}\left[\hat{u}^n + \hat{v}^n\Delta t + \frac{\Delta t^2}{4}\left(\mathcal{N}(\hat{u}^{n+1}) + \mathcal{L}\hat{u}^n + \mathcal{N}(\hat{u}^n)\right)\right].$$

This nonlinear equation can be solved iteratively for $\hat{u}^{n+1}$,

$$\hat{u}^{n+1,j+1} = \left[1 - \frac{\Delta t^2}{4}\mathcal{L}\right]^{-1}\left[\hat{u}^n + \hat{v}^n\Delta t + \frac{\Delta t^2}{4}\left(\mathcal{N}(\hat{u}^{n+1,j}) + \mathcal{L}\hat{u}^n + \mathcal{N}(\hat{u}^n)\right)\right],$$

where the additional superscript j represents the iterate and $\hat{u}^{n+1,0} = \hat{u}^n$ is used as the initial guess for the iteration. Once $\hat{u}^{n+1}$ is computed we can use Eq. (2.76) to calculate $\hat{v}^{n+1}$.

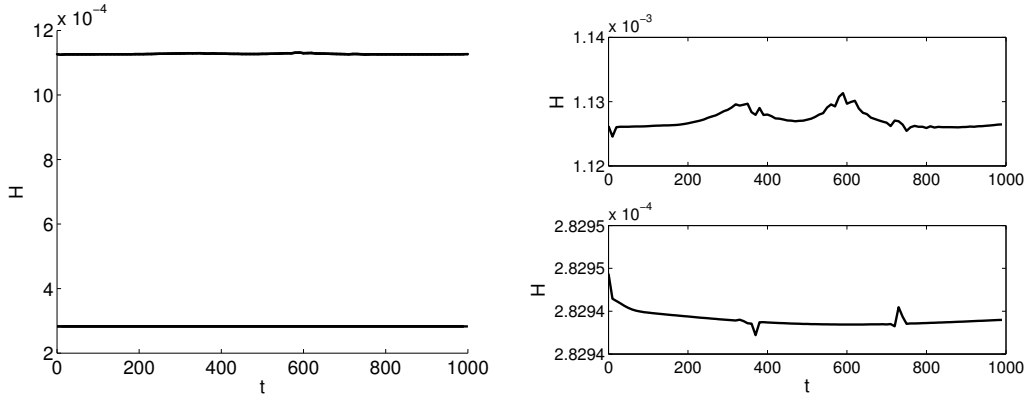

Figure 2.4: Left: Energy plots for a rectangular modulated pulse (top line) and NLS 1-soliton modulated pulse (bottom line). Both energies are bounded for $t \in [0, 1000]$. Right: Zooms of the right panel showing that the energy for the rectangular pulse (top) varies more then the NLS 1-soliton pulse (bottom).

Finally, we show how a simple scaling allows us to extend the spatial domain to $[-a, a]$. Let,

$$\xi = st, \qquad \eta = sx, \qquad p(\eta, \xi) = u(sx, st), \tag{2.77}$$

where $s = \pi/a$. Clearly, $x \in [-a, a]$ for $\eta \in [-\pi, \pi]$. Substituting the above into the original system (2.2) yields,

$$\begin{aligned} \partial_\xi p &= q, \\ \partial_\xi q &= \partial_\eta^2 p - \tfrac{1}{s^2}(p - p^3). \end{aligned}$$

We also have $p_\xi = s^{-1} u_t$ and so the initial data in Eq. (2.46) must be scaled,

$$p_\xi(\eta, 0) = \frac{1}{s} U_1. \tag{2.78}$$

The scaled step-sizes are $\Delta\xi = s\Delta t$ and $\Delta\eta = s\Delta x$.

2.2.4 Geometric pseudo-spectral method

One way to test the integrity of a method is to check to what extent the numerical solution exhibits conservation laws of the full problem. This does not necessarily translate into a statement about accuracy, but we should disregard any schemes that produce numerical solutions where conservation properties are not satisfied (within some tolerance).

The quantity H defined by Eq. (2.4), sometimes referred to as the energy or the Hamiltonian, is a conserved quantity of the NKG equation. As shown in Ref. [CHL08], some schemes fail to conserve energy, especially over long time intervals. We computed the energy of solutions generated by each of the above mentioned integrators for NLS 1-soliton and rectangular described initial data (see Sec. 2.3 for a detailed description of the initial data). In both cases the energy stays bounded (see the left panel of Fig. 2.4). We observed that the energy corresponding to rectangular pulses varies a bit more (see the right panel of Fig. 2.4). This could be because of the loss of regularity of the initial data.

Geometric integrators preserve geometric properties of the flow of a differential equation [HLW00]. The idea is to incorporate the conservation laws into the integrator. A natural question is, how does the energy of a solution obtained using a geometric method compare?

A pseudo-spectral method which uses a structuring preserving scheme for the time marching is developed in Ref. [CHL08] for the NKG equation on the bounded domain $x \in [-\pi, \pi]$. This method is easily adapted to our problem using the scaling (2.77).

Recall the problem cast in the Fourier domain,

$$\partial_t^2 \hat{u} = \mathcal{L}\hat{u} + \mathcal{N}(\hat{u}), \tag{2.79}$$

where $\mathcal{L}$ and $\mathcal{N}$ are defined in Eqs. (2.73) and (2.74) respectively. The only difference here is that we present the second order problem rather than the first order system as shown in Eq. (2.72). Using a structure preserving time discretization yields,

$$\hat{u}^{n+1} - 2\cos\left(\Delta x\sqrt{\mathcal{L}}\right)\hat{u} + \hat{u}^{n-1} = \Delta t^2 \mathrm{sinc}^2\left(\Delta x\sqrt{\mathcal{L}}\right)\mathcal{N}\left(\mathrm{sinc}\left(\Delta x\sqrt{\mathcal{L}}\right)\hat{u}^n\right),$$

where $\mathrm{sinc}(x) = \sin(x)/x$. Derivation of this scheme can be found in Ref. [HLW00, Chapter XIII] which is dedicated to highly oscillatory differential equations. Error analysis for this method in conjunction with Eq. (2.1) can be found in Ref. [CHL08]. However, the analysis is not directly applicable in our case since the small initial data condition is violated (see Eq. (2.78)). Despite this, we found that energy was conserved over long time intervals using this method.

2.2.5 Comparison of methods

We briefly discuss how each method performed and mention some advantages and disadvantages. All programs were run with MATLAB R2007 on a machine with an INTEL PENTIUM D 3.40GHz processor. The algorithms are coded using the optimal performance conventions according to Ref. [Mat08b]. The source code for each method can be found on the web.[4]

Leapfrog: Of the four methods used, the leapfrog method demonstrated the best performance in terms of computation time (see Table 2.1) when compared to the other methods using the same number of spatial grid points M. The program exploits the sparse matrix structure and is required to store only three time levels at any given time step. Implementation and analysis were also straight forward.

Method of lines: Our particular implementation of this method led to the poorest performance results. The major problem is the MATLAB *ode45* routine which is slow for large problems, since it is a *black box* routine. Indeed, with a spatial grid size of 2^{17}, integration takes days (see Table 2.1). The program must be run in small time increments and results saved incrementally in order to avoid memory problems and other bottlenecks. This method could be improved by using an alternative method to solve the ODEs.

Implicit pseudo-spectral method: As mentioned above, the PS methods are slower then the leapfrog scheme when the same value of M is taken. This is because the nonlinear term is computed in the spatial domain (see Eq. (2.74)), and so

[4] See `http://www.iadm.uni-stuttgart.de/LstAnaMod/Chong/home.html`.

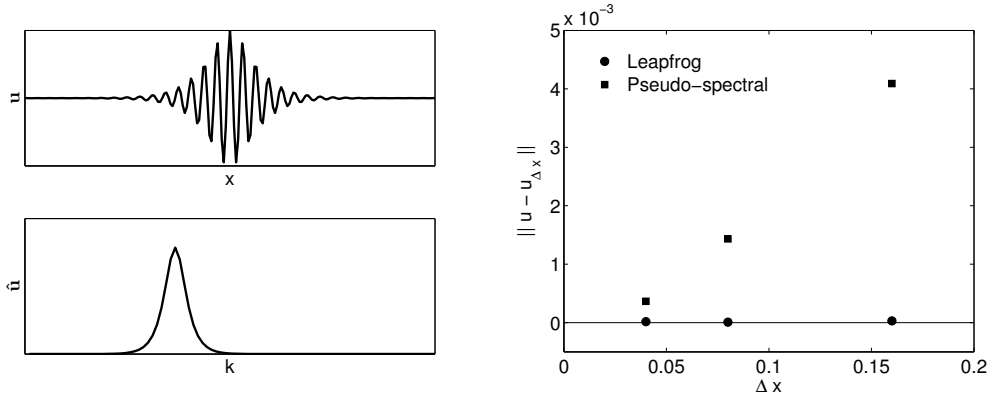

Figure 2.5: Left: Example of a modulated pulse (top) and the corresponding Fourier transform (bottom). Right: The estimated error of the numerical solution for various spatial grid sizes using the leapfrog scheme (squares) and the geometric pseudo-spectral method (circles). Here we used $\sup_{t<\tau} \|u - u_{\Delta x}\|_{l^\infty}$ where u is the numerical solution with $M = 2^{17}$ and $u_{\Delta x}$ is the numerical solution with indicated step size.

the Fourier transform must be computed at each time step. The MATLAB implementation of the fast Fourier transform (FFT) routine requires $\mathcal{O}(M \log M)$ operations[5]. For large problem sizes this seriously affects performance (see Table 2.1). However, making use of the fact that spectrum of the initial data is localized (see left panel of Fig. 2.5), we should be able to take larger step sizes. To check this, we took solutions that were computed with many grid points ($M = 2^{17}$) and compared them with various numerical solutions with smaller M. This provided an estimation of the error. The estimated error in case of the finite difference method was much more severe (as expected due to Theorem 2.9) when compared to the pseudo-spectral methods. The estimated error using a PS method with $M = 2^{12}$, (which only takes seconds to run, see Table 2.2) is smaller then estimated error using the leapfrog method with $M = 2^{17}$ (see the right panel of Fig. 2.5). Thus, the loss of efficiency due to the necessity of the FFT calls is overcompensated by the fact that larger spatial steps can be taken. In fact, when compared with the method of lines, the time is reduced by a factor of 10^4. For the implicit method, the restriction of the time step is also not as large as the leapfrog case, which is an explicit scheme.

Geometric pseudo-spectral method: It was shown in Ref. [CHL08] that this scheme (on the spatial domain $[-\pi, \pi]$) has a smaller time step restriction and is more accurate, and has better conservation properties then the leapfrog scheme. However, the main purpose of this implementation was to explore the conservation of energy, which was not significantly better for our problem. It does, of course, enjoy the aforementioned benefits of PS methods. In terms of computational expense, this method proved to be the best.

[5]Optimal performance is achieved if $M = 2^n$ for some $n \in \mathbb{Z}^+$. However, even in the worst case scenario (when M is prime), $\mathcal{O}(M \log M)$ complexity is still achieved [Mat08a].

Method	**Runtime** (in hours)
Leapfrog	.972
Method of lines	115.00
Implicit PS	5.49
Geometric PS	1.36

Table 2.1: List of runtimes for $M = 2^{17}$ and $\tau = 1000$ for each of the methods described in this section.

M	**Runtime** (in seconds)
2^{12}	54
2^{13}	186
2^{14}	917
2^{17}	4,890

Table 2.2: List of runtimes using the geometric method for various M and $\tau = 1000$.

2.3 Simulation results

Results of the simulations using the solvers explained in Sec. 2.2 are presented in this section. Initial data based on the analytical approximations are used to verify the main results of Ref. [CBSU07] (see summary at end of our Sec. 2.1). Differences between the analytical approximations and the numerical solutions (in the $\|\cdot\|_{l^\infty}$ norm) are taken for various $\varepsilon \to 0$ to estimate the approximation order. The phase and envelope shifts can also be estimated. These are close to the expected values based on the derived formulas for the shifts. The results also suggest that the approximation order obtained in Theorem 2.6 is optimal in orders of ε.

This procedure is also carried out for initial data that is not described by NLS 1-solitons, but rather general localized pulses. We find that the main results of Ref. [CBSU07] should be possible in this case, contrary to expectations (the NLS 1-soliton conjecture).

2.3.1 Definition of the initial data

We start by recalling the initial-boundary-value problem associated to the NKG equation,

$$\begin{aligned} \partial_t^2 u - \partial_x^2 u + u - u^3 &= 0, \\ u(\cdot,0) &= U_0, \\ u_t(\cdot,0) &= U_1, \\ u(-a,\cdot) &= u(a,\cdot) \\ \partial_x u(-a.\cdot) &= \partial_x u(a.\cdot). \end{aligned}$$

For single pulses we define the initial data based on the modulated pulse defined in Eq. (2.27),

$$U_0 = u_{\text{simple pulse}}(x,0). \tag{2.80}$$

Recall that,

$$u_{\text{simple pulse}}(x,t) = \varepsilon A(X,T)E + \text{c.c.},$$

where $A = A(X,T)$ is the complex valued envelope function that modulates the carrier wave $E = e^{\mathrm{i}(k_0 x - \omega_0 t)}$ and $X = \varepsilon(x - ct - x_0)$ and $T = \varepsilon^2 t$. We also need the initial velocity. This is obtained by differentiating (2.80) with respect to t,

$$\partial_t u_{\text{simple pulse}} = (\partial_T A\varepsilon^3 - c\partial_X A\varepsilon^2)E - \varepsilon \mathrm{i}\omega_0 AE + \text{c.c.}\ . \tag{2.81}$$

We are only interested in the case where the envelope function $A(X,T)$ satisfies the NLS equation (2.11). Making this assumption and evaluating at the initial time we arrive at,

$$U_1 = \varepsilon \left[-\mathrm{i}\omega_0 AE - c\partial_X AE\varepsilon - \frac{(1-c^2)\partial_X^2 A + 3|A|^2 A}{\mathrm{i}2\omega_0} E\varepsilon^2 + \text{c.c.} \right]_{t=0} . \tag{2.82}$$

For the pulse corresponding to Theorem 2.6 the envelope function is,

$$A(X,T) = \tilde{A}_{\text{pulse}}(X) e^{-i\gamma T} e^{i\phi}, \tag{2.83}$$

where $\omega_0^2 = k_0^2 + 1$ and $\tilde{A}_{\text{pulse}}$ is the homoclinic solution of Eq. (2.13) with $c = k_0/\omega$ where $\omega = \omega_0 + \varepsilon^2\gamma$. Calculations are done with $\gamma = -0.5$ and $\phi = 0$. Initial data corresponding to this pulse will be called $U_0^{\text{pulse}}(k_0, x_0, \varepsilon)$ and $U_1^{\text{pulse}}(k_0, x_0, \varepsilon)$. The parameters k_0, x_0, and ε appear as arguments since they determine the final shape of the pulse.

2.3.2 Numerical estimate of the approximation order

For the two-pulse case a sum of two separated pulses with $k_A = 2$ and $k_B = 0$ with $\varepsilon = 0.08$ is used as initial data. We define,

$$\begin{aligned} U_0^{\text{two pulse}} &= U_0^{\text{pulse}}(2, 0, .08) + U_0^{\text{pulse}}(0, 10, .08), \\ U_1^{\text{two pulse}} &= U_1^{\text{pulse}}(2, 0, .08) + U_1^{\text{pulse}}(0, 10, .08). \end{aligned}$$

We integrate Eq. (2.44) using the schemes described in Sec. 2.2. We compare the analytical approximations against numerical solutions by taking the difference:

$$r(t_n) = \|\tilde{u}(x_m, t_n) - u_{\text{an}}(x_m, t_n)\|_{l^\infty} , \tag{2.84}$$

as a function of time where $(x_m, t_n) \in D$, $\tilde{u}$ is the numerical solution, and u_{an} is the analytical approximation. We first take $u_{\text{an}} = \Psi$, where Ψ is two pulse ansatz defined in Eq. (2.36) and compare it to the standard ansatz where no shift corrections are taken into account, i.e. $u_{\text{an}} = v_A(k_A x + c_A t - x_A) + v_B(k_B x + c_B t - x_B)$. In the left panel of Fig. 2.6 a plot of $r(t_n)$ is shown. Before interaction, the difference between the standard and the improved approximate solution is negligible. After interaction the approximate solution with the phase shift corrections is clearly better. We compute $\sup_{t_n \in [0,\tau]} r(t_n)$ for various $\varepsilon \to 0$ to estimate the order of the approximation. The data points are fit with a function of the form $f(\varepsilon) = \zeta\varepsilon^\eta$ using MATLAB's *lsqcurve* routine. The best fit functions corresponding to the improved approximation and standard approximation are $f(\varepsilon) \approx 4.80\varepsilon^{3.00}$ and $f(\varepsilon) \approx 5.58\varepsilon^{2.02}$ respectively. See the right panel of Fig. 2.6. Indeed, the approximation with a phase correction is an order better than the standard solution and,

$$\sup_{t_n \in [0,\tau]} r(t_n) = \mathcal{O}(\varepsilon^3). \tag{2.85}$$

This illustrates and confirms Theorem 2.6 due to Eq. (2.71) and Eq. (2.85). The numerics also suggest that the estimate (2.42) is the best possible, since there was agreement in terms of the order.

We now turn to the case where the envelope function is not a NLS 1-soliton. We consider the 2-soliton solution of Eq. (2.11) which has the form,

$$A_{2-\text{soliton}} = Q\left(\zeta_1 \cosh(S_1) + \zeta_2 \cosh(S_2)\right), \tag{2.86}$$

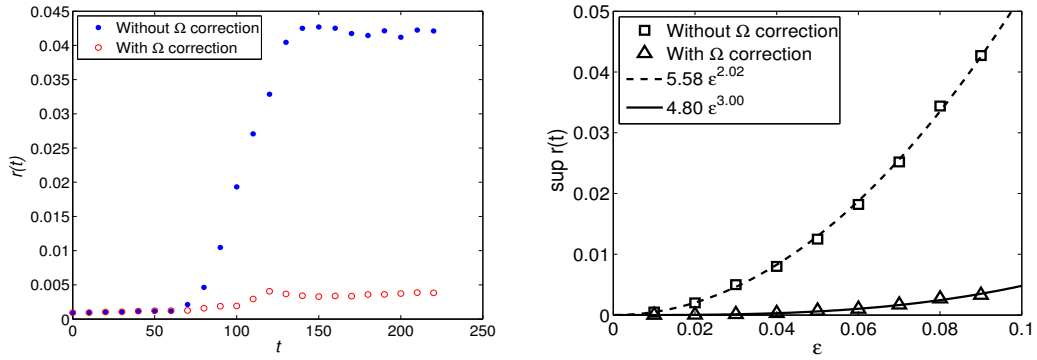

Figure 2.6: Numerical results for $k_A = 2$ and $k_B = 0$. Left: Plot of error function $r(t)$ for $\varepsilon = 0.8$ for the normal solution (points) and the improved solution (circles). Right: Plot of $\sup_{t_n \in [0,\tau]} r(t)$ for various ε (markers) and the functions $5.58\varepsilon^{2.02}$ and $4.80\varepsilon^{3.00}$ (lines).

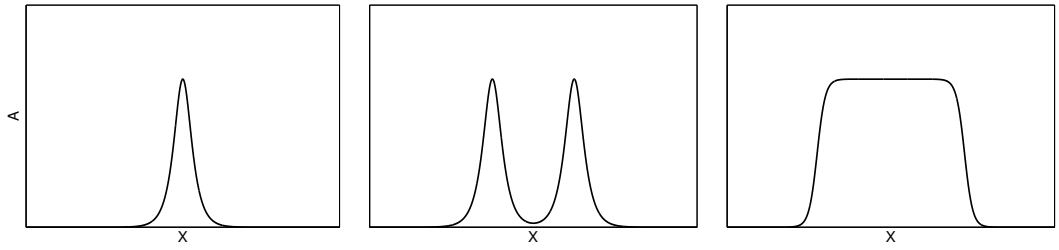

Figure 2.7: Examples of a NLS 1-soliton (left), a NLS 2-soliton (middle) and a rectangular pulse (right) which are used as envelope functions to modulate some carrier wave.

where the exact (quite lengthy) definition of the parameters can be found in Appendix C. Additionally, we consider a rectangular type pulse,

$$A_{\text{rect}} = \frac{-a_1 \tanh(a_2(X - a_3)) \tanh(a_2(X + a_3)) + a_1}{2}, \tag{2.87}$$

with $a_1, a_2, a_3 \in \mathbb{R}$. See Fig. 2.7 for examples of the three envelope functions. Although the analysis in Ref. [CBSU07] was unable to treat this general case, the results below suggest that the restriction on the form of the envelope is not necessary. As shown in Sec. 2.1 and in Ref. [CBSU07], a good single pulse approximation for each pulse along with a phase shift correction was important. The space and time dependent phase shift corrections in this general case (see Sec. 2.4) are,

$$\Omega_A(X_B, T) = \int^{X_B} \frac{3|B(\zeta, T)|^2}{\omega_A(c_A - c_B)}\, d\zeta + \Omega_A^0, \tag{2.88}$$

$$\Omega_B(X_A, T) = \int^{X_A} \frac{3|A(\zeta, T)|^2}{\omega_B(c_B - c_A)}\, d\zeta + \Omega_B^0, \tag{2.89}$$

where A and B represent time-dependent solutions of the NLS equation with initial data given by A_{rect} and B_{rect} or $A_{2-\text{soliton}}$ and $B_{2-\text{soliton}}$ respectively. Since high order single pulse

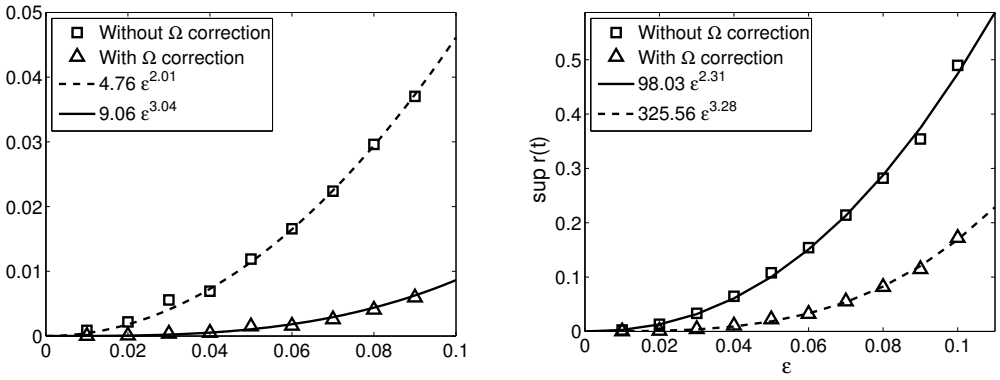

Figure 2.8: Plot of $\sup_{t\in[0,\tau]} r(t)$ (markers) for pulses that have NLS 2-soliton envelopes (left) and rectangular envelopes (right). The fitting functions are also shown (lines).

approximations are not available we take $u_{\rm an}$ to be the sum of the corresponding numerical solutions which we call $\tilde{u}^A(x_m,t_n)$ and $\tilde{u}^B(x_m,t_n)$ respectively, where,

$$\begin{aligned}\tilde{u}^A(x_m,0) &= U_0^{\rm pulse}(2,0,.08),\\ \tilde{u}^B(x_m,0) &= U_0^{\rm pulse}(0,10,.08).\end{aligned}$$

To apply the phase correction we shift the index by the appropriate amount. This allows us to define the error function,

$$r(t_n) = \|\tilde{u}^{A+B}(x_m,t_n) - \tilde{u}^A(x_{m+m_a},t_n) - \tilde{u}^B(x_{m+m_b},t_n)\|_{\Delta x}$$

where,

$$m_a = \left\lfloor \frac{\varepsilon\Omega_A(x_m,t_n)}{k_A\Delta x}\right\rfloor, \qquad m_b = \left\lfloor \frac{\varepsilon\Omega_B(x_m,t_n)}{k_B\Delta x}\right\rfloor,$$

where $\lfloor\cdot\rfloor$ is the floor operator defined by $\lfloor x\rfloor = \max\{n\in\mathbb{Z} : n\le x\}$ and where $\tilde{u}^{A+B}(x_m,t_n)$ is the numerical solution with initial data given by the sum of two pulses (i.e. $\tilde{u}^{A+B}(x_m,0) = \tilde{u}^A(x_m,0) + \tilde{u}^B(x_m,0)$). Figure 2.8 shows $\sup_{t\in[0,\tau]} r(t_n)$ for various $\varepsilon\to 0$. For completeness we also include results for $r(t_n)$ without the phase correction, i.e. $m_a = m_b = 0$. Each set of data was again fit with a function of the form $f(\varepsilon) = \zeta\varepsilon^\eta$. For NLS 2-soliton described pulses we find $f(\varepsilon)\approx 9.06\varepsilon^{3.04}$ when the phase shift is taken into account and $f(\varepsilon)\approx 4.76\varepsilon^{2.01}$ when it is not. For rectangular pulses we find $f(\varepsilon)\approx 325.56\varepsilon^{3.28}$ and $f(\varepsilon)\approx 98.03\varepsilon^{2.31}$ respectively.

Thus, we are able to obtain an improved estimate for approximations that are not described by NLS 1-solitons! We shall discuss the consequences of this shortly, but first we present numerical estimates of the shifts.

2.3.3 Numerical estimate of phase and envelope shifts

The next main result of Sec. 2.1 states that the phase and envelope shifts due to interaction are $\mathcal{O}(\varepsilon)$ (points (ii) and (iii) of the summary in Sec. 2.1). To find the phase shift, we compute the roots of each of the solutions at some time after the interaction. To do this, we first define,

$$L^A = \left\{ m \,:\, \tilde{u}^A(x_m,t)\tilde{u}^A(x_{m+1},t) < 0, m\in\tilde{M}^A\right\},$$

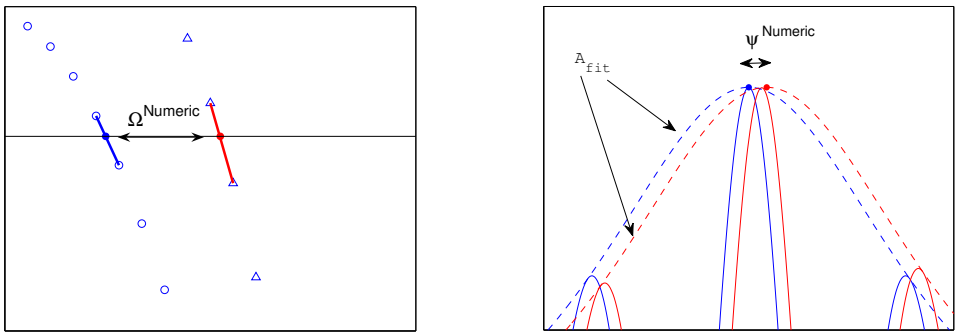

Figure 2.9: Illustration of how the phase (left) and envelope shifts (right) were extracted from the numerical solution.

where $\tilde{M}^A$ is a set of indices where the pulse is located, for example we could take,

$$\tilde{M}^A = [M_{\min}, M_{\max}]$$

where $M_{\min}$ and $M_{\max}$ are defined such that $|\tilde{u}^A(x_m, \cdot)| \leq \frac{\varepsilon}{20}$ for all $m < M_{\min}$ and $m > M_{\max}$. The elements of L^A are the indices of the x values that have an adjacent node with an opposite sign. To obtain approximate roots, we define,

$$R^A = \left\{x \,:\, (\tilde{u}^A(x_l, t) - \tilde{u}^A(x_{l+1}, t))/(x_l - x_{l+1})(x - x_l) + \tilde{u}(x_l, t) = 0, l \in L^A\right\},$$

which are the roots of all the line segments resulting from interpolating pairs of points which lie on opposite sides of the x-axis. Assume similar definitions corresponding to $\tilde{u}^B$ and $\tilde{u}^{A+B}$. If we assume R^A, R^B, and R^{A+B} are ordered, and the numbers I, J, and K represent their cardinalities respectively, where $K = I + J$, then we can define,

$$\Omega_A^{\text{Numeric}} = \frac{\sum_{i=1}^{I} |R_i^{A+B} - R_i^A|}{I}, \tag{2.90}$$

$$\Omega_B^{\text{Numeric}} = \frac{\sum_{i=I+1}^{K} |R_i^{A+B} - R_{i-I}^B|}{J}, \tag{2.91}$$

where $\Omega_A^{\text{Numeric}}$ and $\Omega_B^{\text{Numeric}}$ are the numerically predicted phase shifts of each pulse respectively. An illustration of this procedure can be seen in Fig. 2.9. This can be carried out for all times after the interaction and the resulting shifts computed at each time step can be averaged or maximized. The envelope shift when $k = 0$ can be estimated by looking at the position of the maximal amplitude. This is due to the fact that the carrier wave with $k = 0$ will be identical to its modulating envelope, thus making it easier to detect the actual envelope shift. We define the numerical envelope shift,

$$\psi_B^{\text{Numeric}} = x_{\max}^{A+B} - x_{\max}^B, \tag{2.92}$$

where $x_{\max}^{A+B}$ and $x_{\max}^B$ are the x values of the maximum points of the pulses with $k = 0$ (in our example pulse B). In addition, for the NLS 1-soliton the envelope shift can be found for $k \neq 0$ by fitting the maximal points of the pulse with an appropriate function including a

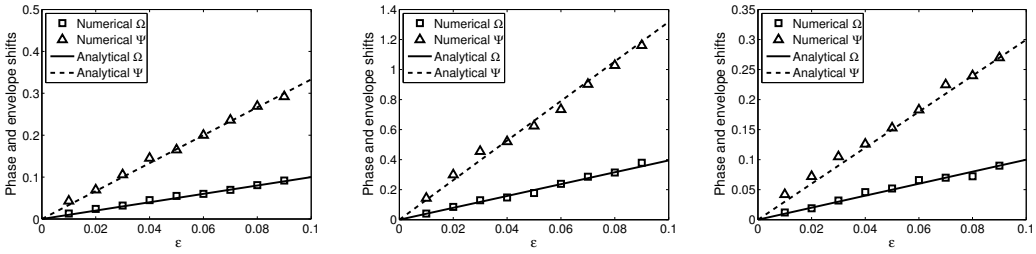

Figure 2.10: Plot of numerically computed phase and envelope shifts (markers) for the NLS 1-soliton case (left), rectangular case (middle) and NLS 2-soliton case (right) based on the procedure explained in the text and the analytical values (lines); all shifts are $\mathcal{O}(\varepsilon)$ and the analytical shifts are close to the numerically computed shifts.

parameter for the envelope shift. For example, for the NLS 1-soliton we would use the trial function,

$$A_{\text{fit}} = p_1 \text{sech}\left(p_2(x - p_3)\right), \tag{2.93}$$

with the fitting parameters $p_1, p_2, p_3 \in \mathbb{R}$. We can define,

$$\psi_A^{\text{Numeric}} \quad = \quad p_3^{\text{A+B}} - p_3^{\text{A}}, \tag{2.94}$$

where $p_3^{\text{A+B}}$ and p_3^{A} are the fitting parameters for the envelope shift for each pulse respectively.

In Sec. 2.1.3 formulas were derived predicting the phase and envelope shifts. In Fig 2.10 the numerically computed phase shifts for pulses with $k = 2$ and envelope shifts for pulses with $k = 0$ and the corresponding analytical values are plotted for the NLS 1-soliton, rectangular, and NLS 2-soliton modulated pulses. Such formulas for the envelope shifts were derived formally in works like [OY74, TPB04]. Since the formulas are not justified, we cannot assume they capture the entire envelope shift, (perhaps other terms of the same order account for interaction effects). However, the numerical results suggest that they are indeed correct.

Summary

We were able to show that $\|\tilde{u} - \Psi\|_{l^\infty} \leq C\varepsilon^3$ where Ψ is a NLS 1-soliton modulated pulse. This, in conjunction with Eq. (2.71) "verifies" Theorem 2.6. This also suggests that the estimate when using NLS 1-soliton envelopes is optimal since the orders agree.

We also posed an approximate solution that was modulated by a general localized function. In this case we were also able to obtain $\|\tilde{u} - \Psi\|_{l^\infty} \leq C\varepsilon^3$. These findings discredit the conjecture that NLS 1-soliton are necessary for the improved estimates of the pulse interaction implicitly stated in Ref. [CBSU07]. In addition, we found good agreement between the analytical values for the phase and envelope shifts and the numerically computed ones.

Thus, all the main results of Ref. [CBSU07] should be possible without assuming the NLS 1-soliton conjecture. Using this insight, we revisit the problem of obtaining improved estimates for modulated pulse interaction in the following section. The numerics suggests that a general ansatz that accurately describes single pulse dynamics can approximate two pulse interaction accurately with the appropriate phase shift corrections taken into account.

2.4 A generalized approximation result

Now that we know that the NLS 1-soliton condition is not necessary, we reexamine the analysis presented in Sec. 2.1 to identify at what steps this was assumed. The NLS 1-solitons have the form,

$$A(X,T) = \tilde{A}(X)e^{-i\gamma T},$$

which motivates the form of the ansatz (2.28), which is,

$$\begin{aligned} u_{\text{two pulse}}(x,t) &= \varepsilon A_1 E + \varepsilon^3 A_3 E^3 + \varepsilon^5 A_5 E^5 + \varepsilon B_1 F + \varepsilon^3 B_3 F^3 + \varepsilon^5 B_5 F^5 \\ &\quad + \varepsilon^3 Y_A E + \varepsilon^3 Y_B F + \varepsilon^3 M_{\text{mixed}} + \text{c.c.}\,, \end{aligned}$$

where

$$\begin{aligned} E &= \exp\left(\mathrm{i}(k_A x - \omega_A t + \varepsilon\Omega_A(X_B))\right), \\ F &= \exp\left(\mathrm{i}(k_B x - \omega_B t + \varepsilon\Omega_B(X_A))\right), \\ A_j &= A_j(X_A), \quad B_j = B_j(X_B), \quad Y_A = Y_A(X_A,T), \quad Y_B = Y_B(X_B,T), \\ X_A &= \varepsilon(x - c_A t - x_A), \quad X_B = \varepsilon(x - c_B t - x_B), \end{aligned}$$

where the envelope functions (e.g. A_1) do not depend on T and the $e^{-i\gamma T}$ has been absorbed by the harmonics E and F (since $\omega_A = \omega_{A,0} + \varepsilon^2\gamma$ and $\omega_B = \omega_{B,0} + \varepsilon^2\gamma$). The naïve way of trying to generalize the problem would be to assume the A_j (and B_j) are time dependent (and to set $\gamma = 0$ since it only makes sense if ansatz (2.12) is used). However, terms like $\varepsilon^{-1}2c_A\partial_T\partial_X A$ appear at order ε^5 in the residual, which breaks the argument used to bound terms, see [CBSU07, Lemma 4.2].

So it seems advisable to consider $2c_A\partial_T\partial_X A$ at order ε^4 and modify the ansatz so that additional terms will appear to cancel it. This will inevitably lead to other undesirable terms in the residual. The question is, how can we modify the ansatz in a clever way?

2.4.1 Separation of internal and interaction dynamics

In order to simplify presentation, let us move all terms with higher order harmonics (E^3, E^5 etc.) to the expression M_{mixed} and let $\omega_A = \omega_{A,0}$. To obtain additional terms in the residual at ε^4 we can modify the ansatz in the following way,

$$\begin{aligned} u_{\text{general}}(x,t) &= (\varepsilon A_1 + \varepsilon^2 A_2 + \varepsilon^3 Y_A)E + (\varepsilon B_1 + \varepsilon^2 B_2 + \varepsilon^3 Y_B)F \\ &\quad + \text{c.c.} + \varepsilon^3 M_{\text{mixed}}, \end{aligned} \tag{2.95}$$

where,

$$\begin{aligned} E &= \exp\left(\mathrm{i}(k_A x - \omega_A t + \varepsilon\Omega_A(X_B))\right), \\ F &= \exp\left(\mathrm{i}(k_B x - \omega_B t + \varepsilon\Omega_B(X_A))\right), \\ A_j &= A_j(X_A,T), \quad B_j = B_j(X_B,T), \quad Y_A = Y_A(X_A,T), \quad Y_B = Y_B(X_B,T), \\ X_A &= \varepsilon(x - c_A t - x_A), \quad X_B = \varepsilon(x - c_B t - x_B), \end{aligned}$$

The difference here is that the envelope functions are time dependent (e.g. $A_1 = A_1(X_A,T)$) and the terms A_2 and B_2 are new. There is also no parameter γ. We find upon substitution of the ansatz (2.95) into the NKG equation (2.1) that the conditions at the first two orders of the

residual remain the same (i.e. we find the linear dispersion and group velocity relationship). At ε^3 we have the NLS equation,

$$-2\mathrm{i}\omega_A\partial_2 A_1 = (1-c_A^2)\partial_1^2 A_1 + 3|A_1|^2 A_1, \tag{2.96}$$

and a time dependent *phase shift formula*,

$$\Omega_A(X_B,T) = \frac{3}{\omega_A(c_A-c_B)}\int^{X_B} |B_1(\zeta,T)|^2 d\zeta + \Omega_A^0, \tag{2.97}$$

where Ω_A^0 normalizes the initial phase. Since Ω_A is a real quantity it represents a *pure phase correction*. We define B_1 and Ω_B in a similar way. At ε^4 we have,

$$\begin{aligned}
&2\omega_A\mathrm{i}\partial_2 A_2 + (1-c_A^2)\partial_1^2 A_2 + \left(6A_2\overline{A}_1 + 3\overline{A}_2 A_1\right)A_1 + 2c_A\partial_1\partial_2 A_1 \ \Big\}\text{internal}\\
&+A_1\left[6\left(B_2\overline{B}_1 + \overline{B}_2 B_1\right) - 2\omega_A\partial_2\Omega_A + \mathrm{i}(1-c_B^2)\partial_1^2\Omega_A + \clubsuit\right] \ \Big\}\text{interaction}\\
&+2\mathrm{i}\partial_1 A_1\left[(1-c_Ac_B)\partial_1\Omega_A(Z_B,T) + \clubsuit\right] \ \Big\}\text{interaction}
\end{aligned}$$

Terms where only A_j appears are grouped together as *internal* and terms where A_j and B_j are mixed are grouped together as *interaction*. Since A_1 (and B_1 for that matter) is already defined through Eq. (2.96) we can use the expression in the *internal* bracket as a condition for A_2 (and likewise for B_2). At this point, the expressions corresponding to the *interaction* brackets cannot be canceled since everything was already defined somewhere else in the residual. The $\clubsuit$ symbols represent the "missing" expressions. However, now that we have separated terms in this logic way, it is clear that we must add *interaction* terms to the ansatz, which in our case correspond to phase and envelope shifts. This motivates the general form of the ansatz.

2.4.2 General ansatz

In order to add interaction terms to the ansatz, we must modify the variables,

$$\begin{cases}
E = & \exp\left(\mathrm{i}(k_Ax - \omega_A t + \varepsilon\Omega_{A,1}(Z_B) + \varepsilon^2\Omega_{A,2}(Z_B))\right),\\
F = & \exp\left(\mathrm{i}(k_Bx - \omega_B t + \varepsilon\Omega_{B,1}(Z_A) + \varepsilon^2\Omega_{B,2}(Z_A))\right),\\
Z_A = & \varepsilon(x - c_At - x_A + \varepsilon\psi_A(Z_B)),\\
Z_B = & \varepsilon(x - c_Bt - x_B + \varepsilon\psi_B(Z_A)),\\
A_j = & A_j(Z_A), \quad B_j = B_j(Z_B), Y_A = Y_A(Z_A,T), \quad Y_B = Y_B(Z_B,T).
\end{cases}$$

Here we have added a higher order correction in the carrier wave $\varepsilon^2\Omega_{A,2}(Z_B)$ and a correction in the envelope $\varepsilon\psi_A(Z_B)$. We now call $\Omega_A = \Omega_{A,1}$. Note that the argument X_A has been replaced by Z_A. The same is done for the variables for the second modulated pulse B. With this modified ansatz, the residual at ε^4 becomes,

$$\begin{aligned}
&2\omega_A\mathrm{i}\partial_2 A_2 + (1-c_A^2)\partial_1^2 A_2 + \left(6A_2\overline{A}_1 + 3\overline{A}_2 A_1\right)A_1 + 2c_A\partial_1\partial_2 A_1 \ \Big\}\text{internal}\\
&\left.\begin{aligned}
&+A_1\left[6\left(B_2\overline{B}_1 + \overline{B}_2 B_1\right) - 2\omega_A\partial_2\Omega_A\right.\\
&\left.+\mathrm{i}(1-c_B^2)\partial_1^2\Omega_A + (\mathbf{k_A} - \mathbf{c_B}\omega_\mathbf{A})\partial_\mathbf{1}\psi_\mathbf{A}(\mathbf{Z_B},\mathbf{T})\right]
\end{aligned}\right\}\text{interaction}\\
&+2\mathrm{i}\partial_1 A_1\left[(1-c_Ac_B)\partial_1\Omega_A(Z_B,T) + \mathbf{2}\partial_\mathbf{1}\mathbf{\Omega_{A,2}}(\mathbf{Z_B},\mathbf{T})(\omega_\mathbf{A}\mathbf{c_B} - \mathbf{k_A})\right] \ \Big\}\text{interaction}
\end{aligned}$$

where the bold expressions represent the desired expressions resulting from the new interaction terms. We can now define the *envelope shift formula*,

$$\psi_A(Z_B,T) = \frac{3(1-c_Ac_B)}{(c_B\omega_A - k_A)^2}\int^{Z_B} |B_1(\eta,T)|^2 d\zeta, \tag{2.98}$$

and *second order correction to the phase shift* which has the form

$$\Omega_{A,2}(Z_B,T) = \operatorname{Re}\Omega_{A,2} + \operatorname{Im}\Omega_{A,2}, \tag{2.99}$$

where,

$$\begin{aligned}\operatorname{Re}\Omega_{A,2} =& \int^{Z_B} \frac{1}{2(k_A-\omega_Ac_B)}\Big(-6\left(B_2\overline{B}_1 + \overline{B}_2B_1\right) + 2\omega_A\partial_2\Omega_{A,1}\Big)d\zeta\ ,\\ \operatorname{Im}\Omega_{A,2} =& \frac{\mathrm{i}(1-c_B^2)\partial_1\Omega_{A,1}}{2(k_A-\omega_Ac_B)} = \frac{3\mathrm{i}(1-c_B^2)}{2(k_A-\omega_Ac_B)^2}|B_1|^2\ .\end{aligned}$$

Since $\Omega_{A,2}(Z_B,T)$ belongs to the carrier wave, the real part $\operatorname{Re}\Omega_{A,2}$ contributes a phase correction, while the imaginary part $\operatorname{Im}\Omega_{A,2}$ is an *amplitude correction*. It can be shown that second order correction to the phase shift (2.99) is algebraically small w.r.t. ε except during the collision of wave packets, see [CBCSU08, Remark 2.3].

At ε^5 we find that Y_A must satisfy a linear PDE (see [CBCSU08, Sec. 3] for the exact expression). From the above analysis, we have shown that A_1 and A_2 contribute to internal dynamics and $\Omega_{A,1}, \Omega_{A,2}, \psi_A$ contribute to interaction dynamics. The situation is less clear for Y_A, since by Taylor expansion w.r.t. ψ_A and ψ_B we have with $X_A = \varepsilon(x-c_At), X_B = \varepsilon(x-c_Bt)$,

$$\begin{aligned}u_{\text{general}} =& \big(\varepsilon A_1(X_A,T) + \varepsilon^2A_2(X_A,T) + \varepsilon^3(Y_A(X_A,T) + \psi_A\partial_1A_1(X_A,T))\big)E\\ &+ \big(\varepsilon B_1(X_B,T) + \varepsilon^2B_2(X_B,T) + \varepsilon^3(Y_B(X_B,T) + \psi_B\partial_1B_1(X_B,T))\big)F + \text{h.o.t.}.\end{aligned}$$

We see that Y_A appears at the same order as the envelope correction and thus it is not clear if the formula ψ_A really describes the entire envelope shift, i.e. if it is *valid*. The numerical results of Sec. 2.3 suggest that the formula for the envelope shift is correct. Indeed, it can be shown that the envelope shift formula is valid, see [CBCSU08, Sec. 6].

2.4.3 Justification of the result

In the previous section we derived six equations such that first nonvanishing term of the residual appear at $\mathcal{O}(\varepsilon^6)$. One can prove the following:

Lemma 2.10. *Let $s \geq 2, m \geq 2, s_A \geq s+10, k_A \neq k_B, k_A, k_B > 0$, and let $A_1|_{T=0}, B_1|_{T=0} \in H^{s_A}(m) \cap H^{s_A+m}(0)$. Then for all $T_0 > 0$ there exist $\varepsilon_0 > 0, C > 0$ such that for all $\varepsilon \in (0,\varepsilon_0)$ we have*

$$\sup_{t\in[0,T_0/\varepsilon^2]} \|\operatorname{Res}(u_{\text{general}})\|_{H^s} \leq C\varepsilon^{11/2}.$$

Proof. Proving the above is a matter of showing the existence of $\mathcal{O}(1)$ solutions on the $\mathcal{O}(1/t^2)$ time scale to six above mentioned equations that eliminate terms up to $\mathcal{O}(\varepsilon^5)$ in the residual, see [CBCSU08, Lemma 4.1].

□

In terms of spaces, we have,

$$\begin{aligned} A_1 &\in C\left([0,T_0], H^{s_A}(m) \cap H^{s_A+m}(0)\right), \\ A_2 &\in C\left([0,T_0], H^{s_A-3}(m) \cap H^{s_A-3+m}(0)\right), \\ Y_A &\in C([0,T_0], H^{s_A-6}(m) \cap H^{s_A-6+m}(0)). \end{aligned}$$

for the internal dynamics terms and,

$$\partial_1\Omega_{A,1}, \partial_1\Omega_{B,1}, \partial_{Z_B}\psi_A, \partial_{Z_A}\psi_B, \mathrm{Im}\Omega_{A,2}, \mathrm{Im}\Omega_{B,2} \in C([0,T_0], H^{s_A}(m) \cap H^{s_A+m}(0)),$$

$$\Omega_{A,1}, \Omega_{B,1}, \mathrm{Re}\Omega_{A,2}, \mathrm{Re}\Omega_{B,2}, \psi_A, \psi_B \in C([0,T_0], C_b^{s_A+m})$$

for the interaction dynamics terms.

Since the estimate of the residual in Lemma 2.10 is the same as that in Lemma 2.4 for the NLS 1-soliton case, the justification follows immediately:

Theorem 2.11. *Let $s \geq 2, m \geq 2, s_A \geq s+10, k_A \neq k_B, k_A, k_B > 0$, and let $A_1|_{T=0}, B_1|_{T=0} \in H^{s_A}(m) \cap H^{s_A+m}(0)$. Then for all $T_0 > 0$ there exist $\varepsilon_0 > 0, C > 0$ such that for all $\varepsilon \in (0, \varepsilon_0)$ we have*

$$\sup_{t\in[0,T_0/\varepsilon^2]} \|u(x,t) - u_{\text{general}}(x,t)\|_{C_b^{s-1}} \leq C\varepsilon^{7/2}, \tag{2.100}$$

where u_{general} is defined in Eq. (2.95) *with variables defined by Eqs.* (2.98)

Proof. The proof is the same as for Theorem 2.3 where the residual condition is satisfied via Lemma 2.10. □

Remark 2.12. There is no associated breather to this general modulated pulse solution since the envelope function is time dependent.

Conclusion

Through the use of the numerical study explained in Sec. 2.3 and the analysis presented in this section, we have an almost complete description of two modulated pulse interaction in the NKG equation (2.1). It was previously known (cf. Ref. [CBSU07]) that for NLS 1-soliton modulated pulse interaction,

- there are approximations with an error of $\mathcal{O}(\varepsilon^3)$ and that
- the corresponding phase and envelope shifts are $\mathcal{O}(\varepsilon)$.

Also, formulas for the envelope shift were derived formally in Ref. [OY74]. Contrary to expectations (cf. [CBSU07, Remark 4.1]) the numerical results suggested that,

- the NLS 1-soliton conjecture was incorrect,
- the estimate was optimal in orders of ε and,
- the formally derived envelope shift formula is correct in the NLS 1-soliton case *and* in the general NLS case.

With insight gained from the numerics, a general result was formulated, i.e. for general NLS envelope functions we have,

- improved error approximation, cf. Theorem 2.11,
- justified formula for the envelope shift, and
- separation of internal and interaction dynamics:
  - the terms A_1, A_2 and Y_A account for internal dynamics
  - the terms $\Omega_{A,1}, \Omega_{A,2}$ and ψ_A contribute to interaction dynamics.

Such estimates of pulse interaction in nonlinear wave equations could be useful for applications in fiber optic communication systems that utilize wavelength division multiplexing, such as those discussed in Appendix A.1.

Chapter 3

The discrete cubic-quintic nonlinear Schrödinger equation

In the continuous setting the existence of breathers is not generic. Indeed, the breathers discussed in Sec. 2.1 were only approximate solutions (albeit good approximations). Introducing discreteness in the spatial coordinate allows the possibility of breather solutions, or "discrete breathers", which are time-periodic, localized solutions of some underlying equations of motion [MA94].

In this chapter we study discrete breathers (also called discrete solitons) in the context of a discrete nonlinear Schrödinger equation with competing cubic and quintic nonlinearities (called the CQDNLS equation). It is shown in Appendix A.2 that this model could be relevant for the description of pulses in nonlinear waveguide arrays. Our study is done in the space of one and two dimensions. In particular, we focus on (A) existence, (B) stability and (C) bifurcations. Each of these three features is investigated with (i) analytical techniques, (ii) numerical methods and (iii) variational approximations.

Discrete soliton solutions of the CQDNLS equation in one spatial dimension were first studied numerically in Ref. [CGTCM06]. We reexamine the one-dimensional problem using tools (i)-(iii) mentioned above. For (i), we make rigorous some of the claims made in Ref. [CGTCM06]. Specifically, (a) the existence and uniqueness of discrete solitons is proved, (b) an exact expression for the essential spectrum of the operator determining stability is provided and (c) we prove the existence of saddle-node and pitchfork bifurcations based on the number of zero eigenvalues of linearized stationary problem using a Lyapunov-Schmidt reduction. The numerical computations (ii) are consistent with what is found in Ref. [CGTCM06], but additionally, we prove the persistence of eigenvalues of the truncated problem in the infinite dimensional problem. The so-called variational approximation (iii) is derived to describe the bifurcations and estimate the spectrum determining stability. This is an extension of the work in Ref. [Kau05] where a variational approximation of discrete solitons was formulated but the stability was not estimated.

An entirely new development presented here is the study of discrete solitons in the two-dimensional CQDNLS equation. In this case, the bifurcation structure is much richer due to the existence of so-called hybrid solutions (which have no counterpart in the 1D model). For (i) we are able to prove existence of the solutions. We formulate a number of conjectures summarizing the observed stability and bifurcation structure, which are supported by the numerical solutions (ii). A variational approximation (iii) of the two-dimensional dis-

crete solitons is also presented, however the spectrum determining stability is not estimated. Finally, the mobility of two-dimensional discrete solitons is also explored with the use of numerical simulations.

3.1 One-dimensional model

The cubic-quintic discrete nonlinear Schrödinger (CQDNLS) equation is,

$$\mathrm{i}\partial_t\psi_n + C\Delta\psi_n + B|\psi_n|^2\psi_n - Q|\psi_n|^4\psi_n = 0, \tag{3.1}$$

where $n \in \mathbb{Z}$ is the lattice site, $\psi_n = \psi_n(t) \in \mathbb{C}$, the parameters $C, B, Q \in \mathbb{R}$ and,

$$\Delta\psi_n \equiv \psi_{n+1} + \psi_{n-1} - 2\psi_n.$$

The CQDNLS is a Hamiltonian system,

$$\mathrm{i}\partial_t\psi_n = \frac{\delta H}{\delta\psi_n^*}, \tag{3.2}$$

with Hamiltonian,

$$H = \sum_{n\in\mathbb{Z}} C\left(\psi_n^*\psi_{n+1} + \psi_n\psi_{n+1}^* - 2|\psi_n|^2\right) + \frac{B}{2}|\psi_n|^4 - \frac{Q}{3}|\psi_n|^6, \tag{3.3}$$

where ψ^* is the complex conjugate. The Hamiltonian (3.3) and the power,

$$M = \sum_{n\in\mathbb{Z}} |\psi_n|^2, \tag{3.4}$$

are conserved quantities of Eq. (3.1). The later is interpreted as power in optics.

As shown in Appendix A.2, the CQDNLS equation describes light propagation in waveguide arrays. In this context C represents coupling strength between adjacent waveguides and so we take $C > 0$. We also assume $B, Q > 0$ so that the nonlinearities have competing signs. One can make the change of variables,

$$\psi_n = \sqrt{\frac{B}{Q}}\psi_n', \qquad t = \frac{B^2}{Q}t', \qquad C = \frac{B^2}{Q}C', \tag{3.5}$$

which has the effect of dropping the B and Q from the equation. For this reason we perform the bifurcation analysis with these values fixed. For included computations we take $B = 2$ and $Q = 1$.

3.1.1 Existence and uniqueness of steady-state solutions

We consider $2\pi/\mu$ time-periodic solutions of the form,

$$\psi_n = u_n e^{-\mathrm{i}\mu t}, \tag{3.6}$$

with $\mu \in \mathbb{R}$. Substitution of Eq. (3.6) in Eq. (3.1) yields a lattice equation for u_n,

$$\mu u_n + C\Delta u_n + 2u_n^3 - u_n^5 = 0. \tag{3.7}$$

Since u_n satisfies the above time independent problem, the solutions are also called steady-states. We seek solutions $\mathbf{u} = \{u_n\}_{n\in Z}$ of (3.7) in the following space:

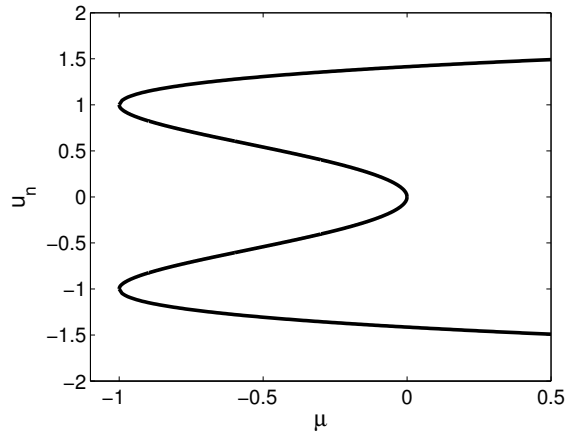

Figure 3.1: Plot of u_n^{tall} and u_n^{short} vs. μ. There are a total of four solutions for $\mu \in (-1, 0)$ and two for $\mu \in (0, \infty)$.

Definition 3.1. The Hilbert space $\Omega = l^2(\mathbb{Z}, \mathbb{C})$ consists of square-summable bi-infinite complex sequences, equipped with the inner product $(\mathbf{v}, \mathbf{w})_\Omega = \sum_{n\in\mathbb{Z}} \bar{v}_n w_n$ and norm $\|\mathbf{v}\|_\Omega = \left(\sum_{n\in\mathbb{Z}} |v_n|^2\right)^{1/2} < \infty$.

The so-called anti-continuum limit equation ($C = 0$) is,

$$\mu u_n + 2u_n^3 - u_n^5 = 0, \tag{3.8}$$

which for fixed $n \in \mathbb{Z}$ has five solutions:

$$u_n^{\text{tall}} = \sqrt{1 + \sqrt{1+\mu}}, \qquad u_n^{\text{short}} = \sqrt{1 - \sqrt{1+\mu}}, \tag{3.9}$$

the negative counterparts, and $u_n = 0$ (see Fig. 3.1). Since $u_n \in \mathbb{R}$ we first restrict $-1 < \mu$. Let $\mathbf{u}^{\text{anticont}}$ denote a sequence where a finite number of points take on one of the values defined in (3.9) while the remaining points are zero. The choice of the space Ω restricts sequences with infinitely many excited sites. Clearly, $\mathbf{u}^{\text{anticont}}$ is a solution to Eq. (3.8). We want to show that such a sequence can be "continued" for $C > 0$ and that these solutions are localized with tails decaying to zero exponentially.

Proposition 3.2. *Let $\mu \in (-1, 0)$. There exists a $C^* > 0$ such that for all $C \in (0, C^*)$ there exists $\kappa > 0$ and $\delta > 0$ such that the lattice equation* (3.7) *has solutions u_n with the following properties:*

$$\text{(i)} \qquad \lim_{C\to 0^+} u_n = u_n^{\text{anticont}}, \tag{3.10}$$

$$\text{(ii)} \qquad \lim_{|n|\to\infty} e^{\kappa|n|}|u_n| = \delta, \tag{3.11}$$

Proof. We prove the above proposition by applying ideas introduced by Mackay and Aubry for discrete breathers (see review [Aub06]).

Part (i). Solutions of Eq. (3.7) correspond to fixed points (FPs) of the operator $F : \Omega \times \mathbb{R} \to \Omega$ which is defined by,

$$F(\mathbf{u}, C) = (\mu u_n + C\Delta u_n + 2u_n^3 - u_n^5)_{n\in Z}. \tag{3.12}$$

Clearly, $F(\mathbf{u}^{\text{anticont}}, 0) = 0$. We can use the implicit function (cf. Ref. [Die69]) to prove that the fixed point $(\mathbf{u}, C) = (\mathbf{u}^{\text{anticont}}, 0)$ has locally unique continuation $\mathbf{u}(C)$ for $C \in (0, C^*)$ for some C^* satisfying $F(\mathbf{u}(C), C) = 0$. We need $F \in C^1$ and that $(DF)^{-1}$ exists and is continuous which is true in our case if DF has trivial kernel due to the explicit form of DF, which is in tridiagonal form with,

$$\begin{aligned} [DF]_{(n,n)} &= \mu - 2C + 6u_n^2 - 5u_n^4, \\ [DF]_{(n-1,n)} &= C, \\ [DF]_{(n,n+1)} &= C. \end{aligned}$$

The eigenvalues of DF evaluated at $(\mathbf{u}^{\text{anticont}}, 0)$ are given by,

$$\begin{aligned} \lambda_n &= -4(\mu + 1 \pm \sqrt{1+\mu}), && \text{if } u_n^{\text{anticont}} = \sqrt{1 \pm \sqrt{1-\mu}}\,, \\ \lambda_n &= \mu, && \text{otherwise.} \end{aligned}$$

Since $\mu \notin \{-1, 0\}$ by hypothesis, the linearization DF has trivial kernel. This proves (i).

Part (ii). Solutions of Eq. (3.7) can be viewed as trajectories of the map $H : \mathbb{R}^2 \to \mathbb{R}^2$ defined by,

$$H : \begin{cases} u_{n+1} &= au_n - v_n - 2C^{-1}u_n^3 + C^{-1}u_n^5, \\ v_{n+1} &= u_n, \end{cases} \tag{3.13}$$

where $a \equiv 2 - \mu/C$. The inverse is,

$$H^{-1} : \begin{cases} u_{n+1} &= v_n \\ v_{n+1} &= av_n - u_n - 2C^{-1}v_n^3 + C^{-1}v_n^5. \end{cases} \tag{3.14}$$

The stable and unstable manifolds of the origin fixed point $(v_n, u_n) = \mathbf{0} = (0, 0)$ are,

$$\begin{aligned} W^{\text{s}} &= \{\mathbf{x} \in \mathbb{R}^2 : H^n(\mathbf{x}) \to \mathbf{0} \text{ as } n \to \infty\}, \\ W^{\text{u}} &= \{\mathbf{x} \in \mathbb{R}^2 : H^{-n}(\mathbf{x}) \to \mathbf{0} \text{ as } n \to \infty\}, \end{aligned}$$

respectively, where H^n denotes n iterations of the map H and H^{-n} denotes n iterations of the inverse map H^{-1}. The solutions $\mathbf{u}$ of Eq. (3.7) described in part (i) have tails decaying to zero as $n \to \pm\infty$ (since only a finite number of nonzero points were taken, and our space Ω consists of sequences which have bounded l^2 norm) and so each point in the solution $u_n \in \mathbf{u}$ satisfies $(v_n, u_n) \in W^{\text{s}} \cap W^{\text{u}}$. A point that is a member of both the stable and unstable manifold is called a homoclinic point. The corresponding trajectory is called a homoclinic orbit. Thus, any solution of Eq. (3.7) with tails decaying to zero can be interpreted as homoclinic orbits of the 2D map (3.13).

Since H is a diffeomorphism, the Stable Manifold Theorem (cf. Ref. [ASY96, Chapter 10]) allows us to obtain the rate at which the origin is approached by studying the linearized system.

The linearized system of H about $\mathbf{0}$ is,

$$DH(\mathbf{0}) = \begin{pmatrix} a & -1 \\ 1 & 0 \end{pmatrix}, \tag{3.15}$$

where $a = 2 - \mu/C$. The eigenvalues of (3.15) are,

$$\lambda_{\mathrm{u,s}} = \frac{a}{2} \pm \sqrt{\left(\frac{a}{2}\right)^2 - 1}. \tag{3.16}$$

The eigenvalues satisfy $\lambda_s < 1 < \lambda_u$. In the linear system, points along the stable eigenvector $(\lambda_\mathrm{s}, 1)$ undergo the dynamics $H^n(\mathbf{x}) = \lambda_\mathrm{s}^n \mathbf{x}$. We can transfer this to dynamics on the stable manifold in a neighborhood of the origin since the hypothesis of the stable manifold theorem are satisfied. By inspection of (3.16) we see that $\lambda_s = 1/\lambda_u$, and thus points along the unstable eigenvector will undergo the dynamics $H^{-n}(\mathbf{x}) = \lambda_\mathrm{s}^n \mathbf{x}$ upon iteration of H^{-1}. Thus, the decay rates for $n \to \pm\infty$ are exponential and given by $\lambda_\mathrm{s}^{|n|}$. This proves (ii).

□

Remark 3.3. Uniqueness is in the sense implied by Proposition 3.2 part (i), i.e. the solutions have locally unique continuation in respect to the parameter C.

Remark 3.4. We represent the stationary CQDNLS equation as $F(\mathbf{u}) = 0$, $F(\mathbf{u}, C) = 0$, or $F(\mathbf{u}, C, \mu) = 0$ depending on the whether the dependence on the parameters is important or not for the particular topic being discussed.

Remark 3.5. The solutions ψ_n of the CQDNLS equation (3.1) and solutions u_n of the stationary CQDNLS equation (3.7) posses the following symmetries

- Solutions do not depend on the location of the lattice.
- Gauge invariance: If ψ_n is a solution then $\psi_n e^{\mathrm{i}\phi}, \phi \in \mathbb{R}$ is a solution.
- Reflection symmetry: If u_n a solution then the corresponding solution after the transformation $n \leftrightarrow -n$ is a solution.

3.1.2 Classification of the steady-states

There are many species of solutions of DNLS equations. They can be characterized based on their properties in the anti-continuum limit. We consider solutions with tails that decay exponentially to zero, and hence correspond to homoclinic orbits of the origin. Solutions of this type are called bright discrete solitons, which are opposed to dark solitons[1] which correspond to heteroclinic orbits. In addition to the asymptotic decay behavior, we require that $u_{|n|} > u_{|n+1|}$ for all $n \in \mathbb{Z}$. This excludes multi-humped solutions. Finally, we require that all the amplitudes are non-negative (which excludes the so-called staggered solutions which have amplitudes with an oscillating sign). These positive amplitude, single humped solutions, approach their continuous counterpart in the limit of infinite coupling strength [CGTCM06], and hence are called fundamental solutions. From herein, we only study *fundamental bright discrete solitons*.

Now that we have reduced our interests to a single species, we look into the families that are possible. If the solution is symmetric about a lattice site, it is called *site-centered*. If it

[1] Dark solitons are also called kinks or fronts.

$S_s:$	$\{\dots,0,u^{\text{short}},0,\dots\}$	$B_{ss}:$	$\{\dots,0,u^{\text{short}},u^{\text{short}},0,\dots\}$
$S_t:$	$\{\dots,0,u^{\text{tall}},0,\dots\}$	$B_{tt}:$	$\{\dots,0,u^{\text{tall}},u^{\text{tall}},0,\dots\}$
$S_{sts}:$	$\{\dots,0,u^{\text{short}},u^{\text{tall}},u^{\text{short}},0,\dots\}$	$B_{stts}:$	$\{\dots,0,u^{\text{short}},u^{\text{tall}},u^{\text{tall}},u^{\text{short}},0,\dots\}$
$S_{ttt}:$	$\{\dots,0,u^{\text{tall}},u^{\text{tall}},u^{\text{tall}},0,\dots\}$	$B_{tttt}:$	$\{\dots,0,u^{\text{tall}},u^{\text{tall}},u^{\text{tall}},u^{\text{tall}},0,\dots\}$
$A_{ts}:$	$\{\dots,0,u^{\text{tall}},u^{\text{short}},0,\dots\}$	$A_{tts}:$	$\{\dots,0,u^{\text{tall}},u^{\text{tall}},u^{\text{short}},0,\dots\}$

Table 3.1: Table of initial configurations used for the numerical continuation explained in Sec. 3.2 to generate the solution branches (see Tables 3.2 and 3.3 and Fig. 3.5). The S stands for site-centered, the B for bond-centered and the A for asymmetric. The number of characters in the subscript indicates the number of adjacent excited sites and the letters t and s stand for tall and short respectively.

is symmetric about the midpoint of two lattice sites, we say it is *bond-centered*. Otherwise it is *asymmetric.* There are subclassifications that are also possible. We define them based on the excited sites in the anti-continuum limit. For example, a solution that has one non-zero node defined by u^{tall} would be a site-centered solution which we call S_t, where the S stands for "site-centered" and the subscript t for "tall". An example of a bond-centered solution would be B_{ss} which has two adjacent excited sites defined by u^{short}. Table 3.1 shows the list of subfamilies that we study here. These solutions are the set of initial configurations used to perform the numerical continuation described in Sec. 3.2. There are sequences available that are not listed in Table 3.1, e.g.,

$$\{\dots,0,u^{\text{short}},u^{\text{short}},u^{\text{short}},0,\dots\}.$$

We exclude them from our study since these configurations become multi-humped for $C>0$. For the sequences listed in Table 3.1 the powers are joined at the boundaries, creating a "snake" like pattern (see Fig. 3.2 for an example using the site-centered family). We are interested in *bifurcations* of the solutions listed in Table 3.1 as the underlying parameters (μ, C) are varied. We say a fixed point undergoes a bifurcation if the solutions near the fixed point are qualitatively different then those at the fixed point. This is somewhat general, but a more precise definition is given in Sec. 3.2.3.

Remark 3.6. Due to the larger number of possible parameter dependent solutions we use the following phrases consistently:

- *Family*: Specifies symmetry type only: site-centered, bond-centered, or asymmetric.
- *Subfamily*: Specifies symmetry type and excited nodes (e.g. S_t).
- *Branch*: A collection of a single subfamily for various μ and fixed C.

3.1.3 Spectral stability

In this section, we consider the stability of the above described solutions with respect to small perturbations. Therefore, we make the following ansatz,

$$\psi_n(t) = (u_n + V_n(t))\, e^{-i\mu t}, \quad n\in\mathbb{Z}, \tag{3.17}$$

where $V_n(t)\in\mathbb{C}$ represents the perturbation. We take the perturbation to be in the same rotating frame with frequency μ to simplify calculations (cf. [CE85]). Substitution of Eq. (3.17)

Branch	Profile	Spectrum
S_s	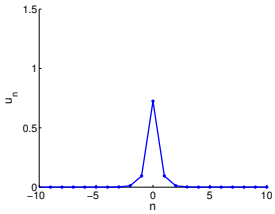	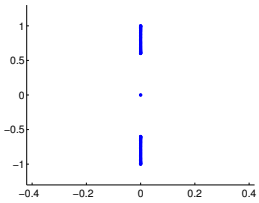
S_t	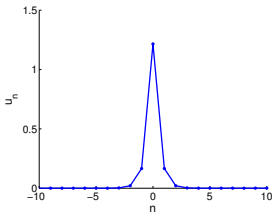	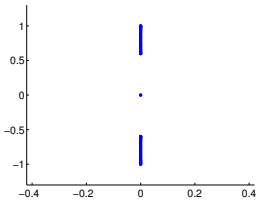
S_{sts}	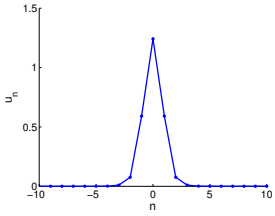	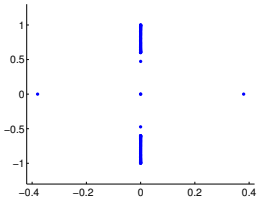
S_{ttt}	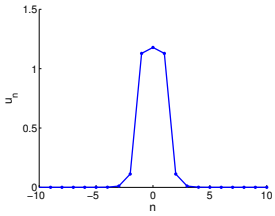	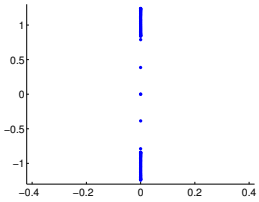

Table 3.2: The site-centered solutions of Table 3.1 with $\mu = -0.6$ continued to $C = 0.1$. Numerical continuation is explained in Sec. 3.2. The solutions only take on values at the lattice sites $n \in \mathbb{Z}$ but are connected by lines to illustrate similarity to continuous solitons. The spectra, which are discussed in Sec. 3.1.3, are given in the right column.

Branch	Profile	Spectrum
B_{ss}	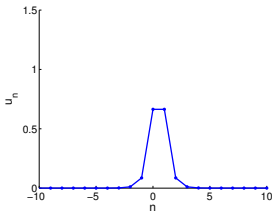	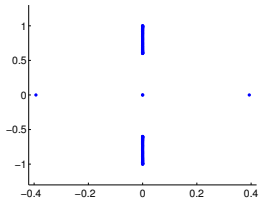
B_{tt}	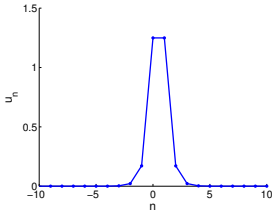	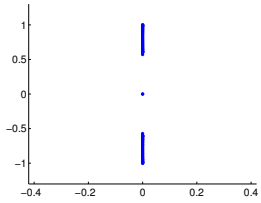
B_{stts}	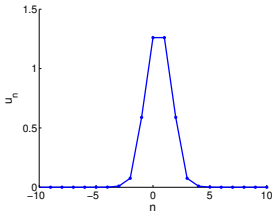	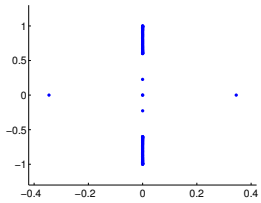
A_{ts}	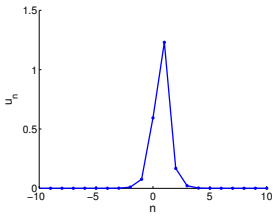	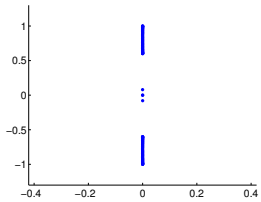
A_{tts}	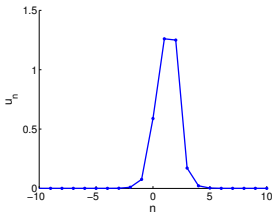	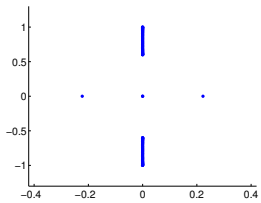

Table 3.3: The bond-centered and asymmetric solutions of Table 3.1 with $\mu = -0.6$ continued to $C = 0.1$. The corresponding spectra are given in the right column.

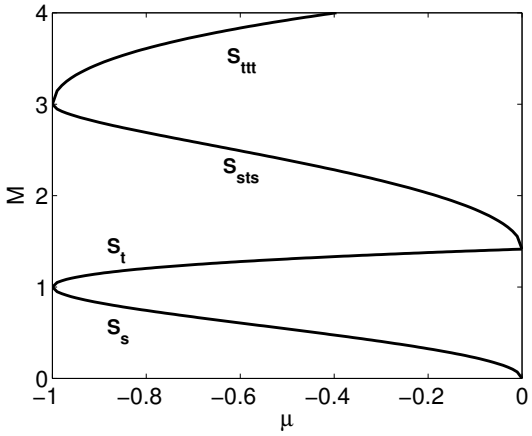

Figure 3.2: Power vs. μ for $C = 0$ of the site-centered family specified in Table 3.1. The power of the bond-centered and asymmetric families have a similar "snaking" pattern.

into Eq. (3.1) yields a system of nonlinear ODEs for the evolution of the perturbation which has the form,

$$\partial_t \mathbf{V} = G(\mathbf{u}, \mathbf{V}), \tag{3.18}$$

where $\mathbf{V} = \{V_n\}_{n\in\mathbb{Z}}$ and $\mathbf{u}$ corresponds to a solution described in Proposition 3.2. At this point, we leave G unspecified. We are interested in stability of FPs $V_n = 0$ of Eq. (3.18). We linearize system (3.18) by taking,

$$V_n(t) = \varepsilon(v_n + iw_n)e^{\lambda t} + \varepsilon(\bar{v}_n + i\bar{w}_n)e^{\bar{\lambda}t}, \quad v_n, w_n, \lambda_n \in \mathbb{C}.$$

Keeping terms linear in ε leads to the non self-adjoint eigenvalue problem,

$$\begin{cases} -\mu v_n - C(v_{n+1} + v_{n-1} - 2v_n) - 6u_n^2 v_n + 5u_n^4 v_n = -\lambda w_n, \\ -\mu w_n - C(w_{n+1} + w_{n-1} - 2w_n) - 2u_n^2 w_n + u_n^4 w_n = \lambda v_n, \end{cases} \quad n \in \mathbb{Z}. \tag{3.19}$$

For the form of the perturbation chosen, if there exists at least one eigenvalue such that $\mathrm{Re}(\lambda) > 0$, then the corresponding solution $\mathbf{u}e^{\mathrm{i}\mu t}$ is unstable. Otherwise, the solution is called spectrally stable. Problem (3.19) can be written in the form,

$$\mathcal{A}\Psi = \lambda\Psi \tag{3.20}$$

where Ψ is the infinite dimensional eigenvector consisting of 2-blocks of $(v_n, w_n)^T$ and $\mathcal{A}$ is the infinite dimensional matrix which consists of 2-by-2 blocks of

$$\mathcal{A}_{n,m} = \begin{pmatrix} 0 & (\mathcal{L}_+)_{n,m} \\ (\mathcal{L}_-)_{n,m} & 0 \end{pmatrix}, \tag{3.21}$$

where $\mathcal{L}_\pm$ are infinite dimensional symmetric tridiagonal matrices consisting of the elements,

$$\begin{cases} (\mathcal{L}_+)_{n,n} = 2C - \mu - 6u_n^2 + 5u_n^4, \\ (\mathcal{L}_-)_{n,n} = 2C - \mu - 2u_n^2 + u_n^4, \\ (\mathcal{L}_+)_{n,n\pm1} = (\mathcal{L}_-)_{n\pm1,n} = -C. \end{cases} \tag{3.22}$$

We seek solutions of (3.20) in the following space:

Definition 3.7. The Hilbert space $\Omega^2 = l^2(\mathbb{Z}, \mathbb{C}^2)$ consists of square-summable bi-infinite complex sequences, equipped with the inner product $(\mathbf{v}, \mathbf{w})_{\Omega^2} = \sum_{n\in\mathbb{Z}} \bar{v}_n w_n$ and norm $\|\mathbf{v}\|_{\Omega^2} = \left(\sum_{n\in\mathbb{Z}} |v_n|^2\right)^{1/2} < \infty$.

We use of the following definitions concerning the non self-adjoint operator $\mathcal{A}$, see [HS95, Def. 1.4]

Definition 3.8. The *resolvent* $\rho(\mathcal{A})$, is the set of $\lambda \in \mathbb{C}$ such that $(\mathcal{A} - \lambda I)$ has continuously bounded inverse in Ω^2, where I is the identity element of Ω^2.

Definition 3.9. The *spectrum* $\sigma(\mathcal{A})$, is the complement of $\rho(\mathcal{A})$ in $\mathbb{C}$; $\sigma(\mathcal{A}) = \mathbb{C}\backslash\rho(\mathcal{A})$.

Definition 3.10. The value λ is an eigenvalue of $\mathcal{A}$ if $\ker(\mathcal{A} - \lambda I)$ is nontrivial in Ω^2, such that there exists a non-zero vector $(\mathbf{v}, \mathbf{w})^T \in \ker(\mathcal{A} - \lambda I)$ called an eigenvector of $\mathcal{A}$.

Definition 3.11. The *discrete spectrum* $\sigma_{\text{dis}}(\mathcal{A})$, is the set of all eigenvalues of $\mathcal{A}$ with finite algebraic multiplicity which are isolated points of $\sigma(\mathcal{A})$.

Definition 3.12. The *essential spectrum* $\sigma_{\text{ess}}(\mathcal{A})$ is the complement of $\sigma_{\text{dis}}(\mathcal{A})$ in $\sigma(\mathcal{A})$; $\sigma_{\text{ess}}(\mathcal{A}) = \sigma(\mathcal{A})\backslash\sigma_{\text{dis}}(\mathcal{A})$.

In the trivial case, we can compute the spectrum exactly:

Lemma 3.13. *Let $\mathcal{A}_0 \equiv \mathcal{A}_{u_n=0}$ correspond to the trivial solution $\mathbf{u} = \mathbf{0}$. The spectrum is,*

$$\sigma(\mathcal{A}_0) = \sigma_{\text{ess}}(\mathcal{A}_0) = \mathrm{i}[\mu - 4C, \mu] \cup \mathrm{i}[-\mu, 4C - \mu].$$

Proof. If we make the change of variables,

$$a_n = v_n + \mathrm{i}w_n, \quad b_n^* = v_n - \mathrm{i}w_n, \quad \omega = \mathrm{i}\lambda, \tag{3.23}$$

then we can rewrite the eigenvalue problem for $\mathcal{A}_0$ as,

$$\begin{cases} \mathcal{H}_0\mathbf{a} = \omega\mathbf{a}, \\ \mathcal{H}_0\mathbf{b} = -\omega\mathbf{b}, \end{cases} \tag{3.24}$$

where $\mathcal{H}_0 = C\Delta + \mu$, $\mathbf{a} = \{a_n\}_{n\in\mathbb{Z}}$ and $\mathbf{b} = \{b_n\}_{n\in\mathbb{Z}}$. Eigenvalues of the operator $\mathcal{H}_0$ satisfy the equation,

$$\mu u_n + C(u_{n+1} + u_{n-1} - 2u_n) \quad = \quad \omega u_n.$$

The associated eigenfunctions are of the form $u_n = p_1\alpha^n + p_2\beta^n$ where $p_1, p_2 \in \mathbb{C}$ and where α and β are roots of the quadratic equation in z,

$$Cz^2 + (\mu - \omega - 2C)z + C = 0.$$

The corresponding eigenfunctions are bounded for $\omega \in [\mu - 4C, \mu]$, which is nonempty since $C > 0$. We know the spectrum of $\mathcal{H}_0$ is composed completely of eigenvalues: suppose $\omega \notin [\mu - 4C, \mu]$. We can apply the discrete Fourier transform in space so that the operator $\mathcal{H}_0$ becomes $\mu - 2(1 - \cos k)$ where k is the spectral variable. Clearly $\mu - 2(1 - \cos k) - \omega$ is invertible for $k \in \mathbb{R}$ and so $\omega \in \rho(\mathcal{H}_0)$.

Due to Eq. (3.24) and $\omega = \mathrm{i}\lambda$, we know $\lambda \in \mathrm{i}[\mu - 4C, \mu] \cup \mathrm{i}[-\mu, 4C - \mu]$. Also there are no isolated eigenvalues and so,

$$\sigma(\mathcal{A}_0) = \sigma_{\text{ess}}(\mathcal{A}_0) = \mathrm{i}[\mu - 4C, \mu] \cup \mathrm{i}[-\mu, 4C - \mu].$$

□

The spectrum of the operator $\mathcal{A}$ is related to unperturbed operator $\mathcal{A}_0$ since the solutions considered have exponentially decaying tails. Before we can relate the two, we will need the following theorem first:

Theorem 3.14. *Suppose X is a Banach space, $T : D(T) \subset X \to X$ is a closed linear operator, $S : D(S) \subset X \to X$ is linear with $D(S) \supset D(T)$ and $S(\lambda_0 - T)^{-1}$ is compact for some λ_0. Let U be an open connected set in $\mathbb{C}$ consisting entirely of points from $\rho(T) \cup \sigma_{\text{dis}}(T)$; then either U consists entirely of points from $\rho(T+S) \cup \sigma_{\text{dis}}(T+S)$, or entirely of eigenvalues of $T + S$.*

Proof. This is [Hen81, Theorem A.1].

□

Theorem 3.15. *Let* **u** *be a solution described in Proposition 3.2. Then,*

$$\sigma_{\text{ess}}(\mathcal{A}) = \sigma_{\text{ess}}(\mathcal{A}_0).$$

Proof. Define S as,

$$S = \begin{pmatrix} 0 & 6 \\ -2 & 0 \end{pmatrix} \mathbf{P} + \begin{pmatrix} 0 & 5 \\ -1 & 0 \end{pmatrix} \mathbf{R}, \tag{3.25}$$

where $\mathbf{P} = \{P_n\}_{n\in\mathbb{Z}}$ with $P_n = u_n^2$ and where $\mathbf{R} = \{R_n\}_{n\in\mathbb{Z}}$ with $R_n = u_n^4$. Clearly $\mathcal{A} = \mathcal{A}_0 + S$. We know Ω is a Banach space and that A_0 is a closed linear operator since it is bounded. Since S decays exponentially to zero it defines a map $S : l^2 \to l^2(s)$ for $s > 0$ where $l^2(s)$ is compactly embedded in l^2. Since $\mathcal{A}_0$ is bounded there exists a λ_0 such that $(\lambda_0 - \mathcal{A}_0)^{-1}$ is bounded and so $S(\lambda_0 - \mathcal{A}_0)^{-1}$ is compact.

Let $U = \mathbb{C}/\sigma_{\text{ess}} = \rho(\mathcal{A}_0)$, which is open and connected in $\mathbb{C}$, (see Lemma 3.13). Since $\mathcal{A}$ is bounded there is a $z \in \rho(\mathcal{A}_0) \cap \rho(\mathcal{A})$ and so $U \subset \rho(\mathcal{A}) \cup \sigma_{\text{dis}}(\mathcal{A})$ due to Theorem 3.14. The other inclusion is obtained by applying the same argument with the roles of A_0 and $A_0 + S$ switched. Thus,

$$\rho(\mathcal{A}_0) = \rho(\mathcal{A}) \cup \sigma_{\text{dis}}(\mathcal{A}).$$

It follows from the definition of the essential spectrum that,

$$\sigma_{\text{ess}}(\mathcal{A}_0) = \sigma_{\text{ess}}(\mathcal{A}).$$

□

Figure 3.3 shows a typical example of the spectrum. Numerical estimates of the spectrum are discussed in Sec. 3.2.2 and examples are given in Tables 3.2 and 3.3.

Remark 3.16. Since we know the essential spectrum, and that it lies on the imaginary axis, only eigenvalues in the discrete spectrum could create instability (i.e. have positive real part).

Remark 3.17. There is always at least one double zero eigenvalue in the stability problem (3.20) which is related to the gauge symmetry $\psi_n \leftrightarrow \psi_n e^{\mathrm{i}\phi}$ for $\phi \in \mathbb{R}$. This double zero eigenvalue corresponds to the eigenvectors $(v_n, w_n) = (0, u_n)$ and $(v_n, w_n) = (\partial_\mu u_n, 0)$ of system (3.20).

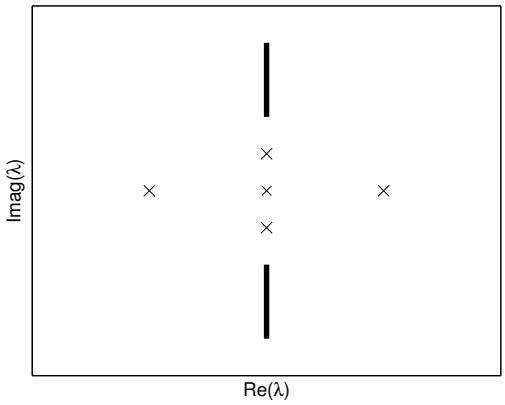

Figure 3.3: Example of spectrum for the eigenvalue problem (3.20). The essential spectrum is indicated by the solid lines whereas the discrete spectrum is indicated by markers.

3.1.4 Bifurcations

Before discussing bifurcations of the CQDNLS, we need to make some definitions. Consider ODEs of the form,

$$\dot{x} = f(x, \alpha), \tag{3.26}$$

with $x = x(t)$ and the system parameter $\alpha \in \mathbb{R}$, and $f \in C^3(\mathbb{R} \times \mathbb{R}, \mathbb{R})$. We define the following bifurcations in the standard way, see [Wig03, Chapter 20].

Definition 3.18. A *saddle-node* bifurcation is a local bifurcation in which two fixed points collide and annihilate each other.

Equation (3.26) undergoes a saddle-node bifurcation at the point (x_0, α_0) if,

$$\begin{cases} f(x_0, \alpha_0) & = 0, \\ \partial_x f(x_0, \alpha_0) & = 0, \end{cases} \tag{3.27}$$

and,

$$\partial_\alpha f(x_0, \alpha_0) \neq 0 \tag{3.28}$$

$$\partial_x^2 f(x_0, \alpha_0) \neq 0. \tag{3.29}$$

Equation (3.27) specifies that the fixed point (x_0, α_0) is non-hyperbolic, which is a necessary condition for a point to be a bifurcation point. This along with Eqs. (3.28) and (3.29) indicate that the function $f(x, \alpha)$ is qualitatively the same as the normal form of the saddle-node bifurcations,

$$\dot{x} = \alpha \pm x^2,$$

near $(x_0, \alpha_0) = (0, 0)$. See the left of panel Fig. 3.4 for an example.

Definition 3.19. A *pitchfork* bifurcation is a local bifurcation where the bifurcation point defines intervals which consist of either a single fixed point or three fixed points which collide at the bifurcation point.

Equation (3.26) undergoes a pitchfork bifurcation at the point (x_0, α_0) if,

$$\begin{cases} f(x_0, \alpha_0) & = 0, \\ \partial_x f(x_0, \alpha_0) & = 0, \end{cases}$$

and,

$$\partial_\alpha f(x_0, \alpha_0) = 0, \tag{3.30}$$

$$\partial_x^2 f(x_0, \alpha_0) = 0, \tag{3.31}$$

$$\partial_x \partial_\alpha f(x_0, \alpha_0) \neq 0, \tag{3.32}$$

$$\partial_x^3 f(x_0, \alpha_0) \neq 0. \tag{3.33}$$

Again we must have that the fixed point (x_0, α_0) is non-hyperbolic. This along with Eqs. (3.30)–(3.33) indicate that the function $f(x, \alpha)$ is qualitatively the same as the normal form of the pitchfork bifurcations,

$$\dot{x} = x(\alpha \pm x^2),$$

near $(x_0, \alpha_0) = (0, 0)$. See the right panel of Fig. 3.4 for an example.

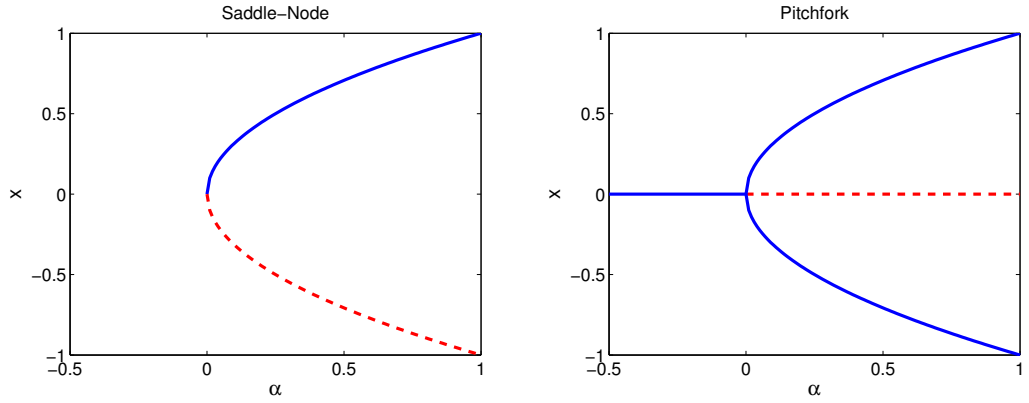

Figure 3.4: Left: Plot of fixed points of $f(x) = \alpha - x^2$. A saddle-node bifurcation occurs at $(x, \alpha) = (0, 0)$. Right: Plot of fixed points of $f(x) = x(\alpha - x^2)$. A pitchfork bifurcation occurs at $(x, \alpha) = (0, 0)$.

It can be shown that the CQDNLS stationary equation $F(\mathbf{u}, \mu) = 0$ undergoes the bifurcations defined above if certain criteria are met.

Theorem 3.20. *Suppose $F(\mathbf{u^0}, \mu_0) = 0$ (defined in (3.7)) for some fixed C and the linearization $L = DF(\mathbf{u^0}, \mu_0)$ has a one-dimensional kernel. Let $\mathbf{k} \in \ker L$. The following holds:*

(i) If $\partial_\mu F(\mathbf{u^0}, \mu_0)$ and $\partial_{\mathbf{u}}^2 F(\mathbf{u^0}, \mu_0)(\mathbf{k}, \mathbf{k})$ are both nonzero and are not in range *L then the point $(\mathbf{u^0}, \mu_0)$ is a saddle-node bifurcation point.*

(ii) If $\partial_\mu F(\mathbf{u^0}, \mu_0)$ and $\partial_{\mathbf{u}}^2 F(\mathbf{u^0}, \mu_0)(\mathbf{k}, \mathbf{k})$ are both nonzero and belong to range *L and if $\partial_\mu(\partial_{\mathbf{u}} F(\mathbf{u^0}, \mu_0)(\mathbf{k}))$ and $\partial_{\mathbf{u}}^3 F(\mathbf{u^0}, \mu_0)(\mathbf{k}, \mathbf{k}, \mathbf{k})$ are both nonzero and not in* range *L then the point $(\mathbf{u^0}, \mu_0)$ is a pitchfork bifurcation point.*

Proof. We prove the above statement using a Lyapunov-Schmidt reduction (cf. [Chi99, GSS88]) to reduce the problem to a one-dimensional one. In this setting we can deduce which kind of bifurcation occurs using Definitions 3.18 and 3.19 based on the derivatives of the reduced function. The explanation of the derivatives that appear in the theorem (e.g. $\partial^2_{\mathbf{u}} F(\mathbf{u^0}, \mu_0)(\mathbf{k}, \mathbf{k})$) can be found in Corollary 3.22.

Recall $\Omega = l^2(\mathbb{Z}, \mathbb{C})$. We can use the splittings,

$$\Omega = \ker L \oplus (\ker L)^{\perp}, \tag{3.34}$$

$$\Omega = (\text{range } L)^{\perp} \oplus \text{range } L, \tag{3.35}$$

where the orthogonal complement is taken with respect to the inner product $< \cdot, \cdot >_{\Omega}$. Let $\Pi : \Omega \to \text{range } L$ denote the projection of Ω onto range L and $\Pi^{\perp} : \Omega \to (\text{range } L)^{\perp}$ the corresponding complementary projection. We can re-write the stationary CQDNLS equation (3.7) as,

$$\Pi F(\mathbf{u}, \mu) = 0, \tag{3.36}$$

$$\Pi^{\perp} F(\mathbf{u}, \mu) = 0. \tag{3.37}$$

Due to the splitting (3.34) we can decompose elements $\mathbf{u} \in \Omega$ in the form $\mathbf{u} = v + w$ where $v \in \ker L$ and $w \in (\ker L)^{\perp}$. Thus we can write Eq. (3.36) as,

$$\Pi F(v + w, \mu) = 0.$$

It follows from the implicit function theorem that Eq. (3.36) can be solved uniquely for w near $(\mathbf{u^0}, \mu_0)$ with solution $w = W(v, \mu)$ such that,

$$\Pi F(v + W(v, \mu), \mu) = 0. \tag{3.38}$$

Using this W we can obtain a one dimensional mapping,

$$\Pi^{\perp} F(v + W(v, \mu), \mu) = 0.$$

In order to obtain information about the reduced function, we introduce nonzero coordinates $\mathbf{k} \in \ker L$ and $\mathbf{k}^{\perp} \in (\text{range } L)^{\perp}$ such that $v = x\mathbf{k}$ and $w = x\mathbf{k}^{\perp}$ for some $x \in \Omega$. This allows us to define the desired reduced mapping,

$$g(x, \mu) =< \mathbf{k}^{\perp}, F(x\mathbf{k} + W(x\mathbf{k}, \mu), \mu) >_{\Omega} . \tag{3.39}$$

part (i). To show that $(\mathbf{u^0}, \mu_0)$ is a saddle-node bifurcation point we need that $g_{xx} \neq 0$ and $g_{\mu} \neq 0$ where the derivatives are evaluated at the fixed point (see Def. 3.18). It can be shown (see Ref. [GSS88, Part I.3]) that,

$$g_{xx} = < \mathbf{k}^{\perp}, \partial^2_{\mathbf{u}} F(\mathbf{k}, \mathbf{k}) >_{\Omega}, \tag{3.40}$$

$$g_{xxx} = < \mathbf{k}^{\perp}, \partial^3_{\mathbf{u}} F(\mathbf{k}, \mathbf{k}, \mathbf{k}) - 3\partial^2_{\mathbf{u}} F(\mathbf{k}, L^{-1}\Pi \partial^2_{\mathbf{u}} F(\mathbf{k}, \mathbf{k})) >_{\Omega}, \tag{3.41}$$

$$g_{\mu} = < \mathbf{k}^{\perp}, \partial_{\mu} F >_{\Omega}, \tag{3.42}$$

$$g_{x\,\mu} = < \mathbf{k}^{\perp}, \partial_{\mu} F \cdot \mathbf{k} >_{\Omega} . \tag{3.43}$$

Thus, if the conditions specified in (i) of the theorem are met, the reduced function satisfies $g_{xx} \neq 0$ and $g_{\mu} \neq 0$. The non-hyperbolic fixed point condition (3.27) is satisfied by construction and so $(\mathbf{u^0}, \mu_0)$ is a saddle-node bifurcation point.

part (ii). Using the formulas (3.40)-(3.43) and assuming the conditions specified in (ii) of the theorem are met, we see that $g_{xx} = g_\mu = 0$ and $g_{xxx} \neq 0 \neq g_{\mu x}$ and so $(\mathbf{u^0}, \mu_0)$ is a pitchfork bifurcation point.

□

Remark 3.21. The solutions of $F(\mathbf{u}) = 0$ do not correspond to fixed points of the ODE $\partial_t \mathbf{u} = F(\mathbf{u})$ but rather periodic solutions of the CQDNLS equation. Therefore, the above theorem only applies to the number of solutions and not the corresponding stability. All eigenvalues of L can be mapped to imaginary eigenvalues of $\mathcal{A}$ which, as expected, do not determine stability.

Corollary 3.22. *The CQDNLS possesses pitchfork and saddle-node bifurcations points.*

Proof. We verify the hypothesis of Theorem 3.20 numerically. In this finite setting, we can estimate coordinates $\mathbf{k} \in \ker L$ and $\mathbf{k}^\perp \in (\text{range } L)^\perp$ using the singular-value decomposition (cf. [TB97, HJ90]) of the linearization,

$$U\Sigma V^* = L.$$

We choose $\mathbf{k}$ to be the column vector from the left singular value matrix U that corresponds to the smallest (near zero) singular value (i.e. smallest magnitude value of Σ). Using the fact that $(\text{range } L)^\perp = \ker L^*$ where L^* is the adjoint of L, we can choose $\mathbf{k}^\perp$ to be the column vector of the right singular value matrix V that corresponds to the smallest (near zero) singular value. The singular value decomposition can be obtained numerically using the *svd* routine in MATLAB. Calculating the derivatives of the functions is straightforward due to the structure of the map F. We illustrate the procedure to calculate $\partial^2_{\mathbf{u}} F(\mathbf{k}, \mathbf{k})$. Here $(\mathbf{k}, \mathbf{k})$ indicates the direction the derivative being taken in, not evaluation. First we compute $\partial_{\mathbf{u}} F(\mathbf{k}) = [DF] \cdot \mathbf{k}$,

$$[DF] \cdot \mathbf{k} = (k_{n-1}C + k_n(\mu - 2C + 6u_n^2 - 5u_n^4) + k_{n+1}C)_{|n|/2<N}, \tag{3.44}$$

where N is the chosen lattice size. To compute the second derivative, we find the Jacobian of Eq. (3.44) and multiply by $\mathbf{k}$,

$$\partial^2_{\mathbf{u}} F(\mathbf{k}, \mathbf{k}) = [D([DF] \cdot \mathbf{k})] \cdot \mathbf{k} = (k_n^2(12u_n - 20u_n^3))_{|n|/2<N}. \tag{3.45}$$

The higher order derivatives can be computed in the same way. Thus we have a way computing the derivatives of the reduced function g (i.e. Eqs. (3.40)–(3.43)). Values of the numerical estimates of the derivatives are given in Table. 3.4. This requires numerical estimates of the solutions, which is discussed in the next section.

3.2 Numerical approximations

To complement the above analysis and to get a better understanding of the phenomenology and overall bifurcation structure, we conduct a numerical study. Numerical solutions of the CQDNLS were already studied in Ref. [CGTCM06], however our approach and focus is different. That is, we (a) prove that discrete eigenvalues of the truncated spectral problem (3.20) persist in the infinite-dimensional problem (see Sec. 3.2.2), (b) we study the numerical bifurcations in the (μ, M) plane, which reveals how the different subfamilies are related in a clearer way and (c) the numerical results are combined with Theorem 3.22 to make a precise classification of the bifurcation scenario.

3.2.1 Numerical steady-states

Numerical steady-states can be found by solving the stationary CQDNLS equation (3.7) using a Newton method for some small $C > 0$ with the $C = 0$ solution as the initial guess (see Table 3.1 for the initial configurations used). The processes halts when the desired value of C is reached, or if Newton's method fails to converge (the first value of C where failure occurs is an approximation of C^* in Proposition 3.2). This process is called *numerical continuation*. This is how the profiles shown in Tables 3.2 and 3.3 were obtained. We take a grid size of $N = 101$.

3.2.2 Numerical estimates of spectral stability

To numerically estimate the spectrum determining stability corresponding to some steady-state $\mathbf{u}^N$ with a lattice size of N, we solve the truncated eigenvalue problem,

$$M\Psi = \lambda\Psi, \tag{3.46}$$

where Ψ is the $2N$ dimensional eigenvector consisting of 2-blocks of $(v_n, w_n)^T$ and where M is a $2N$-by-$2N$ matrix which consists of 2-by-2 blocks of,

$$M_{n,m} = \begin{pmatrix} 0 & (\mathcal{L}_+)_{n,m} \\ (\mathcal{L}_-)_{n,m} & 0 \end{pmatrix},$$

where $(\mathcal{L}_\pm)_{n,m}$ is given by Eq. (3.22) with $m, n \in [-N/2, N/2]$. This representation assumes zero boundary conditions. The truncated problem (3.46) can be easily solved using MATLAB's *eig* routine. The spectra shown in Tables 3.2 and 3.3 were obtained in this way. We know the eigenvalues determining instability (i.e. those with positive real part) persist in the infinite dimensional problem (3.20) due to the following theorem:

Theorem 3.23. *Let* $\mathbf{u}$ *be a solution of the stationary CQDNLS equation* (3.7) *with the properties described in Proposition 3.2. If* γ *is an eigenvalue of the truncated system* (3.46) M *with fixed lattice size* N *and* γ *bounded away from* $\sigma_{\text{ess}}(\mathcal{A})$ *then there exists a* $\lambda \in \sigma_{\text{dis}}(\mathcal{A})$ *and a* $C^{**} > 0$ *such that for all* $C \in (0, C^{**})$ *we have,*

$$|\gamma - \lambda| \leq cC^2,$$

where $c > 0$ *is independent of* C.

Proof. Let x be the N dimensional vector corresponding to the coordinates of the truncated system and y be the coordinates of the infinite-dimensional remaining part such that the eigenvalue problem (3.20) has the form,

$$Mx + C_1 y = \lambda x, \tag{3.47}$$

$$C_2 x + Ay = \lambda y, \tag{3.48}$$

where M is the matrix defined in Eq. (3.46), and C_1, C_2 and A are matrices with entries consisting of 2-by-2 blocks defined by Eq. (3.21), where the indices are respectively,

$$\begin{aligned} C_1 &: n \in [-N/2, N/2], \quad m \in (-\infty, -N/2 - 1) \cup (N/2 + 1, \infty), \\ C_2 &: n \in (-\infty, -N/2 - 1) \cup (N/2 + 1, \infty), \quad m \in [-N/2, N/2], \\ A &: n \in (-\infty, -N/2 - 1) \cup (N/2 + 1, \infty),\ m \in (-\infty, -N/2 - 1) \cup (N/2 + 1, \infty). \end{aligned}$$

Since the solutions $\mathbf{u}$ described in Proposition 3.2 have tails that decay exponentially toward zero, i.e. $u_n = \mathcal{O}(e^{-\kappa|n|})$ for $\kappa > 0$ and $n \to \infty$, the matrix A is $\mathcal{O}(e^{-\kappa|N|})$ close to the linearization around the trivial solution, i.e.

$$A = A_0 + \mathcal{O}(e^{-\kappa N}), \tag{3.49}$$

where A_0 is the linearization around the trivial solution. First we want to show that for all $\varepsilon > 0$ there is a lattice size N such that $\sigma(A) \subset U_\varepsilon(\sigma(A_0))$, where $U_\varepsilon(X)$ is an ε neighborhood of X. Define $Q = U_R(0)$ with $R > 0$ such that $\sigma(A) \cup U_\varepsilon(\sigma(A_0)) \subset Q$.

Suppose $\lambda \in Q/U_\varepsilon(\sigma(A_0))$. We can write,

$$\begin{aligned}(A - \lambda I)^{-1} &= (A_0 + \mathcal{O}(e^{-\kappa N}) - \lambda I)^{-1} \\ &= (A_0 - \lambda I)^{-1}(I + \mathcal{O}(e^{-\kappa N})(A_0 - \lambda I)^{-1})^{-1}.\end{aligned}$$

We have $\mathcal{O}(e^{-\kappa N})(A_0 - \lambda I)^{-1} < 1$ for N sufficiently large (or C sufficiently small since $\kappa = \mathcal{O}(1/C)$) and so $\lambda \in Q/\sigma(A)$. We know $\sup_{\lambda \in Q \cap \rho(A)} \|(A-\lambda I)^{-1}\|_\Omega$ exists due to the continuity of $\lambda \mapsto \|(A - \lambda I)^{-1}\|_\Omega$ in $\rho(A)$, the compactness of $Q/U_\varepsilon(\sigma(A_0))$ and $\|(A - \lambda I)^{-1}\|_\Omega \leq C/|\lambda|$ for $C > 0, \lambda \in \mathbb{C}/Q$, and $R > 0$ sufficiently large. Thus, $\sigma(A) \subset U_\varepsilon(\sigma(A_0))$. We also have $U_\varepsilon(\sigma(A_0)) \subset U_\varepsilon(\sigma_{\text{ess}}(\mathcal{A}))$ due to Lemma 3.25.

Since γ is bounded away from $\sigma_{\text{ess}}(\mathcal{A})$ we look for λ bounded away from $\sigma_{\text{ess}}(\mathcal{A})$. Hence λ is bounded away from $\sigma(A)$ by the above argument and Eq. (3.48) can be solved w.r.t y,

$$y = -(A - \lambda I)^{-1} C_2 x,$$

with $(A - \lambda I)^{-1}$ uniformly bounded independent of λ and C. Inserting this expression into Eq. (3.47) yields the reduced eigenvalue problem,

$$Mx - C_1(A - \lambda I)^{-1} C_2 x = \lambda x. \tag{3.50}$$

Let γ be an eigenvalue of M. Suppose that for all $\lambda \in \sigma_{\text{dis}}(\mathcal{A})$ the following holds,

$$|\gamma - \lambda| > \mathcal{O}(C^2). \tag{3.51}$$

Since $(M - \lambda I)^{-1} \propto (\lambda - \gamma)^{-1}$ we immediately have that $\lambda \notin \sigma(M)$ due to assumption (3.51). We know,

$$(I + \mathcal{O}(C^2)(M - \lambda I)^{-1})^{-1},$$

exists since $\mathcal{O}(C^2)|\gamma - \lambda|^{-1} < 1$ (by assumption). It follows that λ is in the resolvent set of,

$$(M - \lambda I)(I + \mathcal{O}(C^2)(M - \lambda I)^{-1}).$$

Additionally, since $\lambda \notin \sigma(A)$ and $C_1(A - \lambda I)^{-1} C_2 = \mathcal{O}(C^2)$, we have,

$$\begin{aligned}(M - \lambda I)(I + \mathcal{O}(C^2)(M - \lambda I)^{-1}) &= (M + \mathcal{O}(C^2) - \lambda I) \\ &= (M - C_1(A - \lambda I)^{-1} C_2).\end{aligned}$$

Since this is the left hand side of Eq. (3.50) it follows that $\lambda \in \rho(\mathcal{A})$ which contradicts the assumption that $\lambda \in \sigma_{\text{dis}}(\mathcal{A})$. Thus, there exists a $\lambda \in \sigma_{\text{dis}}(\mathcal{A})$ such that,

$$|\gamma - \lambda| < \mathcal{O}(C^2).$$

□

Remark 3.24. For $C = 0$, we have $2r$ zero eigenvalues if r sites are excited. These eigenvalues move away from the origin as C is increased. By numerical experiments, we estimated that eigenvalues γ that move along the real axis do so at $\mathcal{O}(C)$. Thus for C sufficiently small, if $\mathrm{Re}(\gamma) > 0$ then $\mathrm{Re}(\lambda) > 0$.

The above tells us that eigenvalues indicating instability in the truncated system have unstable siblings in the full problem for small C.

Lemma 3.25. *The spectrum of the matrix A_0 defined in Eq.* (3.49) *is a part of the essential spectrum of $\mathcal{A}$, i.e.,*

$$\sigma(A_0) \subset \sigma_{\text{ess}}(\mathcal{A}).$$

Proof. The eigenvalue problem for A_0 is identical to that of $\mathcal{A}_0$ (see Lemma 3.13) with the additional condition that the eigenfunctions satisfy,

$$\begin{cases} p_1\alpha^{N/2+1} + p_2\beta^{N/2+1} & = 0, \\ p_1\alpha^{-N/2-1} + p_2\beta^{-N/2-1} & = 0, \end{cases} \tag{3.52}$$

where $p_1, p_2 \in \mathbb{C}$ and α, β are roots of the quadratic equation in z,

$$Cz^2 + (\mu - \omega - 2C)z + C = 0.$$

Since $\alpha^{N/2+1} = \beta^{-N/2-1}$, Eq. (3.52) becomes,

$$\begin{pmatrix} \alpha^{N/2+1} & \beta^{N/2+1} \\ \beta^{N/2+1} & \alpha^{N/2+1} \end{pmatrix} \begin{pmatrix} p_1 \\ p_2 \end{pmatrix} = 0.$$

The above has non-trivial solutions only if $\alpha^{N+2} - \beta^{N+2} = 0$, or equivalently,

$$\alpha^{2N+4} = 1. \tag{3.53}$$

Independent of this condition, in order to have bounded solutions for $|n| \to \infty$ we also need $|\alpha| = |\beta| = 1$ which is exactly true for $\omega \in [\mu - 4C, \mu]$ which corresponds to $\sigma(\mathcal{A}_0)$ (after transformation (3.23) is applied). Thus,

$$\sigma(A_0) \subset \sigma(\mathcal{A}_0) = \sigma_{\text{ess}}(\mathcal{A}),$$

where the last equality comes from Lemma 3.15.

□

3.2.3 Numerical approximations of the bifurcations

As described in Ref. [CGTCM06], we expect the existence of a large family of solutions at low values of C, which gradually annihilate, through a series of bifurcations, as $C \to \infty$. For example it is observed that for C large enough $B_{ss} = B_{tt}$, see below. See Ref. [ABK04] for a detailed description of the termination scenario in the cubic DNLS equation, which typically occurs through saddle-node or pitchfork, for the various families of the basic discrete solitons as the coupling parameter is increased.

To start, we take the B_{ss} initial configuration,

$$B_{ss}: \quad \{\dots, 0, u^{\text{short}}, u^{\text{short}}, 0, \dots\}$$

	$\mu \approx -0.9092$	$\mu \approx -0.9065$
g_x	$5.93{\cdot}10^{-9}$	$7.04{\cdot}10^{-9}$
g_{xx}	5.57	$2.37{\cdot}10^{-9}$
g_{xxx}	-23.56	-22.01
g_μ	-1.42	$-2.13{\cdot}10^{-10}$
$g_{\mu x}$	0.99	0.96

Table 3.4: Two points along the B_{ss} branch where L has non-trivial kernel. Derivatives of the reduced function are computed using the procedure described in Corollary 3.22. Due to Theorem 3.20 we conclude that $(\mu, C) \approx (-0.9092, 0.1)$ is a saddle-node bifurcation (middle column) and $(\mu, C) \approx (-0.9065, 0.1)$ is a pitchfork bifurcation (right column). This is also illustrated in Fig. 3.5.

and perform the numerical continuation process until $C = 0.1$. We then vary the remaining parameter μ. We consider the μ dependent branch B_{ss} for the fixed value of $C = 0.1$. Since we use a Newton method, we must compute the linearization $L = DF$ for each solution along the branch. We were able to find two points along the B_{ss} branch where L had nontrivial kernel. Using Theorem 3.20 we were able to deduce what type of bifurcation points they are (see Table 3.4).

We repeat the same procedure for the remaining initial configurations specified in Table 3.1 (e.g. S_s). To better visualize the bifurcation structure we plot slices of $(\mu, C, M(\mu, C))$ space. In particular we first fix $C = 0.1$ and plot the (μ, M) plane of the three solution families (bond- and site-centered and asymmetric). See Fig 3.5. Spectral stability, based on the computations explained in Sec. 3.2.2, is also depicted. Solid blue lines indicate spectral stability and dashed red lines indicate instability. The connection of the branches no longer

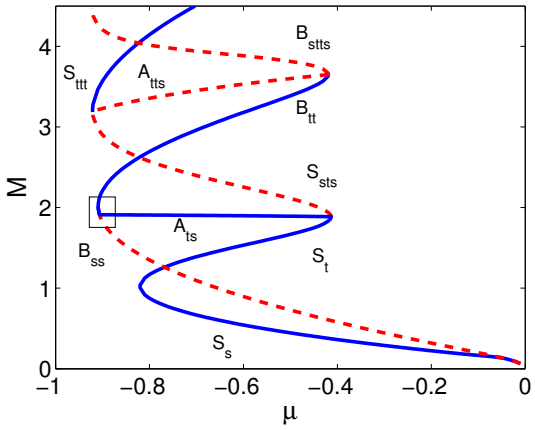

Figure 3.5: Numerical solutions in the (μ, M) plane corresponding to the branches listed in Table 3.1 for $C = 0.1$. Stable branches are represented by solid blue lines and unstable by dashed red lines. The two principle branches, one corresponding to site-centered solutions and one for bond-centered solutions, are connected via asymmetric solutions. The boxed area corresponds to the bifurcation described in Table 3.4. A zoom of the boxed area is shown in Fig. 3.7.

occurs on the boundaries $\mu = -1$ or $\mu = 0$ as in the $C = 0$ case (cf. Fig. 3.2). Indeed, as the coupling strength C increases, the snake like curve of the power looks as though it is being stretched from above, slowly eliminating the number of solutions until only a single profile is left, which corresponds to the well known continuous cubic-quintic NLS solution (see Eq. (2.23) and Fig. 3.6). It is worthwhile to highlight here the increased level of complexity of the relevant $M(\mu)$ curves in the cubic-quintic model (due to the interplay of short and tall solution branches) in comparison to its cubic counterpart of Ref. [Kev08], which features a single change of monotonicity (and correspondingly of stability) between narrow and tall (stable) and wide and short (unstable) solutions.

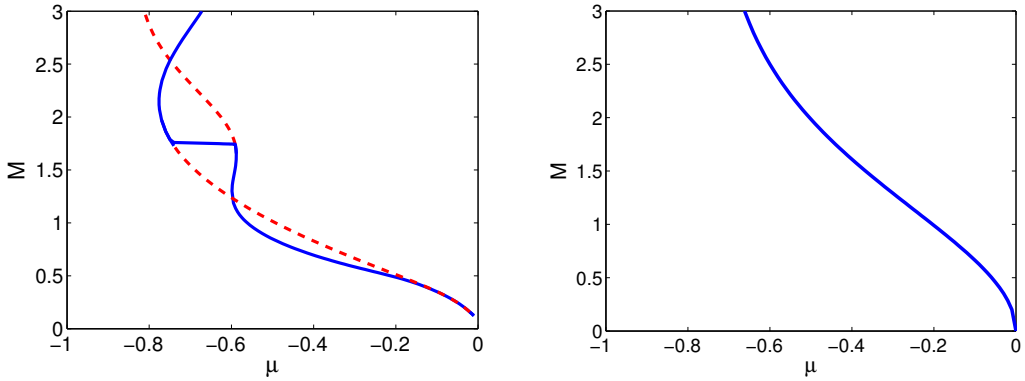

Figure 3.6: Left: Plot of the numerical solutions in the (μ, M) plane for $C = 0.3$. Right: As C increase, the $M(\mu)$ curve approaches that one corresponding to the continuous solution (see Eq. 2.23).

In Fig. 3.5 it looks as if the asymmetric solutions connect exactly at turning points. As already shown (cf. Table 3.4) this is not the case. The stability exchange occurs at the pitchfork where the asymmetric solutions emanate. In terms of stability, the saddle-node bifurcation point is not as interesting as no stability change occurs. It was observed that there are four zero eigenvalues of the spectral problem (3.20) at the pitchfork bifurcation points (see panel (b) in Fig. 3.7). This observation could be proved using a Lyapunov-Schmidt reduction similar to the one described in Theorem 3.20, however we do not do so here.

Although the focus of the numerical study performed in Ref. [CGTCM06] was different that done here, areas where there is overlap are consistent. The major point being that asymmetric solutions emanate via pitchfork bifurcations from symmetric solutions.

Besides numerical approximations, it is possible to study discrete solitons of the CQDNLS using another approximation technique which is based on the Lagrangian formulation of the problem. We address this in the next section.

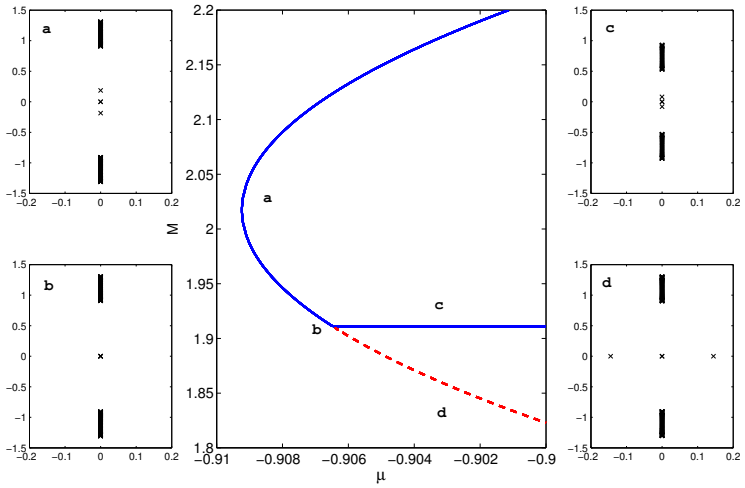

Figure 3.7: Center: Zoom of the boxed area in Fig. 3.5. This area corresponds to the bifurcations described in Table 3.4. The saddle-node bifurcation of the bond-centered solutions B_{ss} and B_{tt} occurs near **a** and a pitchfork bifurcation is shown near **b** which includes the asymmetric solutions A_{st}, A_{ts} and the bond-centered solution B_{ss}. The asymmetric solutions are represented by only one branch in the figure since the powers are identical (which due to the symmetry properties, see Remark 3.5). The spectra determining stability (not of L) corresponding to the labels **a-d** are shown in the surrounding panels.

3.3 Variational approximations

The variational approximation (VA) has long been used as a semi-analytic technique to approximate solitary wave solutions of nonlinear evolution equations with an underlying Hamiltonian structure [Mal02]. The main idea is to pose an ansatz with a fixed number of parameters which are then chosen to satisfy a number of equations (typically fewer then the dimension of the problem). The set of equations are derived based on a reduced version of the Lagrangian and is explained below.

There have been a number of papers exploring the VA with four parameters as a relevant approximation of localized modes in DNLS equations [MW96, PKMF03, CKFM09]. Kaup [Kau05] extended the variational approximation with six parameters that allowed him to construct not only site-centered solutions (as done previously in [MW96]) but also the bond-centered solutions for the cubic DNLS equation ($Q = 0$). We use Kaups method to study bifurcations in the CQDNLS ($Q \neq 0$).

A variational approximation was already derived in [CGTCM06] for the stationary CQDNLS problem (3.7). We derive the approximation within the context of the *time dependent* problem (3.1) and therefore we are also able to approximate the spectrum determining stability. Stability was not predicted in [Kau05].

3.3.1 Variational approximations of steady-states

The CQDNLS equation, which has a Hamiltonian structure, has a Lagrangian formulation,

$$\mathcal{L} = \sum_{n\in\mathbb{Z}} \frac{i}{2}\left(\psi_n^*\partial_t\psi_n - \psi_n\partial_t\psi_n^*\right) + H, \tag{3.54}$$

where H is the Hamiltonian defined in (3.3). Consider the action,

$$S = \int_{t_0}^{t_1} \mathcal{L}\, dt. \tag{3.55}$$

It can be shown (cf. [SS99, Chapter 2]) that functions ψ that satisfy the so-called Euler-Lagrange equations will be extrema of the action S. If the Lagrangian (3.54) is chosen, the Euler-Lagrange equations reduce to the CQDNLS equation (3.1). This provides the heuristic justification for the variational approximation. Namely, we solve Euler-Lagrange equations for a truncated version of the Lagrangian equation (3.54) (called the effective Lagrangian). A detailed account of the variational approximation can be found in review [Mal02].

To find approximate solutions for fundamental bright discrete solitons, we pose a trial function of the form,

$$\psi_n^{\text{ansatz}} = Ae^{i\phi_n}e^{-\eta|n-n_0|}, \quad \phi_n = \alpha + k(n-n_0) + \frac{\beta}{2}(n-n_0)^2, \tag{3.56}$$

where each of the six parameters are dependent on t. Substituting Eq. (3.56) into the Lagrangian (3.54) and evaluating the sum yields the effective Lagrangian,

$$\begin{aligned}\mathcal{L}_{\text{eff}} &= -A^2\left(\frac{\mathrm{d}\alpha}{\mathrm{d}t} - \frac{k}{2}\frac{\mathrm{d}\chi}{\mathrm{d}t}\right)S_0 - A^2\left(\frac{\mathrm{d}k}{\mathrm{d}t} - \frac{\beta}{2}\frac{\mathrm{d}\chi}{\mathrm{d}t}\right)S_1 - \frac{A^2}{2}\frac{\mathrm{d}\beta}{\mathrm{d}t}S_2 \\ &\quad + CA^2\left(e^{ik}S_\beta + e^{-ik}S_\beta^* - 2S_0\right) + A^4S_4 - \frac{1}{3}A^6S_6,\end{aligned} \tag{3.57}$$

where $\chi = 2n_0 - 1$ and,

$$\begin{aligned}S_0(\eta,\chi) &= \frac{\cosh\chi\eta}{\sinh\eta}, \\ S_1(\eta,\chi) &= \frac{\cosh\eta\sinh\chi\eta}{2\sinh^2\eta} + \frac{\chi}{2}S_0, \\ S_2(\eta,\chi) &= \left(\frac{2}{\sinh^2\eta} + \frac{1}{4}\right)S_0 - \frac{\chi}{2}\frac{\cosh\eta\sinh\chi\eta}{\sinh^2\eta} - \frac{\chi^2}{4}S_0, \\ S_4(\eta,\chi) &= S_0(2\eta,\chi), \\ S_6(\eta,\chi) &= S_0(3\eta,\chi), \\ S_\beta(\eta,\chi,\beta) &= e^{-\eta}e^{-\frac{i}{2}\beta\chi}\left(1 + \frac{e^{-\eta\chi}}{e^{i\beta}e^{\eta} - e^{-\eta}} + \frac{e^{\eta\chi}}{e^{-i\beta}e^{\eta} - e^{-\eta}}\right).\end{aligned}$$

Since the center n_0 of the ansatz (3.56) can be arbitrarily chosen on $[0,1]$ module the discrete group of translations in n, $n\in\mathbb{Z}$, we shall consider χ on $[-1,1]$ (this restriction was used already in the derivation of (3.57)). The solution with $\chi = 0$ is centered between lattice sites and hence corresponds to bond-centered solutions. The solution with $\chi = \pm 1$ is centered on a

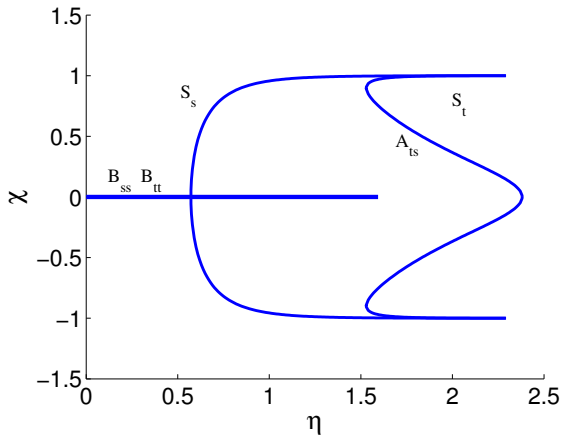

Figure 3.8: Solutions of Eqs. (3.61) and (3.62) for $C = 0.1$.

lattice site and hence corresponds to site-centered solutions. Solutions for $\chi \in (-1, 0) \cup (0, 1)$ are *asymmetric*.

The Euler-Lagrange equations for the effective Lagrangian $\mathcal{L}_{\text{eff}}$ are,

$$\frac{\partial \mathcal{L}_{\text{eff}}}{\partial p_j} - \frac{d}{dt}\left[\frac{\partial \mathcal{L}_{\text{eff}}}{\partial \dot{p}_j}\right] = 0, \tag{3.58}$$

where p_j represents a parameter of ansatz (3.56). The above system of six ODEs represents the finite dimensional space where we search for approximate solutions. Applying (3.58) to α yields the conservation law,

$$A^2 S_0 = M, \tag{3.59}$$

which corresponds to the dynamical invariant (3.4) of the power. Varying A yields,

$$\begin{aligned} \frac{\mathrm{d}\alpha}{\mathrm{d}t} &= \frac{\mathrm{d}\chi}{\mathrm{d}t}\frac{k}{2} - \frac{\mathrm{d}k}{\mathrm{d}t}\frac{S_1}{S_0} + \frac{\beta}{2}\frac{S_1}{S_0}\frac{\mathrm{d}\chi}{\mathrm{d}t} - \frac{1}{2}\frac{\mathrm{d}\beta}{\mathrm{d}t}\frac{S_2}{S_0} + \frac{C}{S_0}(e^{ik}S_\beta + e^{-ik}S_\beta^* - 2S_0) \\ &+ 2M\frac{S_4}{S_0^2} - M^2\frac{S_6}{S_0^3}\,. \end{aligned} \tag{3.60}$$

Before writing the remaining equations, it will be more convenient to make use of the fact that we seek steady-state solutions. This corresponds to $\beta = k = \frac{\mathrm{d}\chi}{\mathrm{d}t} = \frac{\mathrm{d}\eta}{\mathrm{d}t} = 0$ and $\frac{d\alpha}{dt} = -\mu$, where μ is the frequency (see (3.6)). With this assumption the equations corresponding to the variation of k and β are identically satisfied. Varying χ and η and making use of Eq. (3.60) leads to the following two equations respectively,

$$\frac{A^2\eta\sinh\eta\chi}{\sinh\eta\cosh\eta\chi}\left(\frac{A^4 2\cosh\eta\cosh\eta\chi}{4\cosh^2\eta - 1} - A^2 + Ce^{-\eta}\sinh 2\eta\right) = 0, \tag{3.61}$$

and,

$$\begin{aligned} &-Ce^{-\eta}\left(1 + \frac{\cosh\eta\chi - \cosh\eta}{\sinh\eta} + \frac{\chi\sinh\eta\chi}{\cosh\eta\chi}\right) + \frac{A^2\chi\sinh\eta\chi}{\sinh 2\eta\cosh\eta\chi} \\ &+ \frac{A^2\cosh 2\eta\chi}{\sinh^2 2\eta} - A^4\left(\frac{\chi\sinh\eta\chi}{\sinh 3\eta} + \frac{\cosh\eta\cosh 3\eta\chi}{\sinh^2 3\eta}\right) = 0. \end{aligned} \tag{3.62}$$

Note these equations with $Q = 0$ correspond to those in Ref. [Kau05]. When $\chi = 0$ (bond-centered solutions), Eq. (3.61) is identically satisfied and Eq. (3.62) becomes,

$$\frac{-Ce^{-\eta}(1+e^{-\eta})\sinh^2 2\eta}{\sinh\eta} + A^2 - \frac{A^4\cosh\eta\sinh^2 2\eta}{\sinh^2 3\eta} = 0, \tag{3.63}$$

which is easily solved for in A^2, giving an existence condition in terms of the parameter η. There exists exactly two bond-centered solutions (B_{ss} and B_{tt}) for $\eta \in (0, \eta_{\rm cr})$, which disappear as a result of the saddle–node bifurcation at $\eta = \eta_{\rm cr}$. See Fig. 3.8, where solutions of Eqs. (3.61) and (3.62) are plotted for $C = 0.1$, with $\eta_{\rm cr} \approx 1.56$.

For $\chi \neq 0$, the term in parenthesis of Eq. (3.61) can be used as condition for A^2, which can then be substituted into (3.62) yielding a root finding problem in (η, χ) parameter space. We find exactly three pairs of solutions for $C = 0.1$, which correspond to the S_s, S_t, and A_{ts} solutions. In Fig. 3.8 the branches (S_s, S_t) and (S_t, A_{ts}) are connected by means of the saddle-node bifurcations. Branch S_s arises as a result of the supercritical pitchfork bifurcation, while branches S_t and A_{ts} arise as a result of the subcritical pitchfork bifurcation. Note, the bifurcations we refer to here correspond to Eq. (3.61), and not the CQDNLS stationary problem, which is discussed in Sec. 3.3.3.

The VA solution branches S_s and S_t have values of χ that rapidly approach (in respect to η) $\chi = 1$, so that they correspond to the site-centered solitons slightly disturbed by the variational approximation. The solution branch A_{ts} is a true asymmetric solution that connects the bond-centered and site-centered solitons. Only one branch of site-centered solutions and only one branch of bond-centered solutions exist in the cubic case $Q = 0$, where these two branches extend for any $\eta > 0$ (see Ref. [Kau05]).

To test the validity of the variational approximations we compare them against the direct numerical simulations described in the previous section. The numerical solutions are obtained using the Newton method with the VA solutions as initial seeds and $\frac{d}{dt}\alpha = -\mu$. The profiles of the discrete solitons that are obtained via the VA and the corresponding numerical solutions are shown in Fig. 3.9 for $C = 0.1$. We note, for larger C solutions of the full problem become smoother (they approach the continuous counterpart) and so the ansatz, which is based on an exponential cusp, becomes irrelevant.

3.3.2 Variational approximations of spectral stability

In order to approximate the spectrum and hence determine stability within the VA we return to the variational equations (3.58) but this time without the assumption that $\beta = k = \frac{\mathrm{d}\chi}{\mathrm{d}t} = \frac{\mathrm{d}\eta}{\mathrm{d}t} = 0$. Let $\vec{x} = (\beta, \chi, \eta, k)^T$ represent the four parameters of ansatz (3.56) after Eqs. (3.59) and (3.60) are used. To perform a linear stability analysis we substitute,

$$\vec{x} = \vec{x}_0 + \varepsilon\vec{y}_0 e^{\lambda t}, \quad \lambda \in \mathbb{C},$$

into the four variational equations, where the stationary solution is defined by $\vec{x}_0 = (0, \chi_0, \eta_0, 0)^T$ and (χ_0, η_0) satisfy Eqs. (3.61) and (3.62). Keeping only the terms linear in ε leads to the generalized eigenvalue problem,

$$\lambda\mathbf{A}\vec{y}_0 = \mathbf{B}\vec{y}_0, \tag{3.64}$$

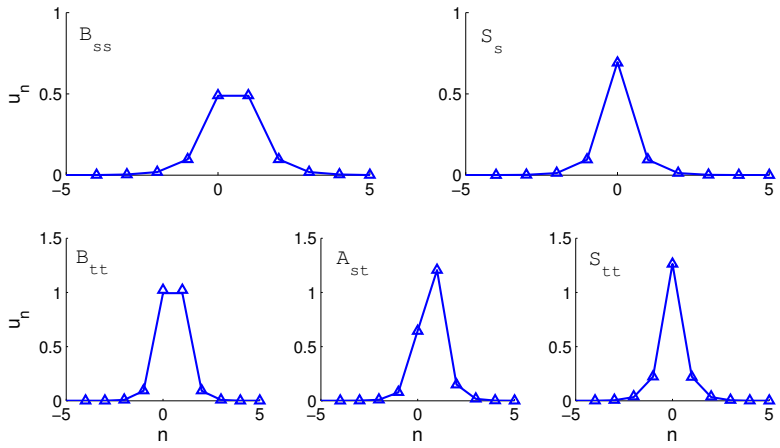

Figure 3.9: Five subfamilies that are captured by the VA using ansatz (3.56). Numerical solutions are shown as a solid line and the variational solutions are indicated by markers. Here $C = 0.1$.

where the entries of the 4×4 matrices $\mathbf{A}$ and $\mathbf{B}$ are given by,

$$a_{11} = 0, \qquad a_{21} = 0,$$
$$a_{12} = \frac{M}{2} + M\frac{\partial}{\partial\chi}\left[\frac{S_1}{S_0}\right], \qquad a_{22} = \frac{M}{2}\left(\frac{S_1}{S_0} + \frac{\partial}{\partial\chi}\left[\frac{S_2}{S_0}\right]\right),$$
$$a_{13} = M\frac{\partial}{\partial\eta}\left[\frac{S_1}{S_0}\right], \qquad a_{23} = \frac{M}{2}\frac{\partial}{\partial\eta}\left[\frac{S_2}{S_0}\right],$$
$$a_{14} = 0, \qquad a_{24} = 0,$$

$$a_{31} = \frac{M}{2S_0}\left(\frac{\partial S_0}{\partial\chi}\frac{S_2}{S_0} - \frac{\partial S_2}{\partial\chi} - S_1\right), \qquad a_{41} = \frac{M}{2S_0}\left(\frac{\partial S_0}{\partial\eta}\frac{S_2}{S_0} - \frac{\partial S_2}{\partial\eta}\right),$$
$$a_{32} = 0, \qquad a_{42} = 0,$$
$$a_{33} = 0, \qquad a_{43} = 0,$$
$$a_{34} = \frac{M}{S_0}\left(\frac{\partial S_0}{\partial\chi}\frac{S_1}{S_0} - \frac{\partial S_1}{\partial\chi}\right) - \frac{M}{2}, \qquad a_{44} = \frac{M}{S_0}\left(\frac{\partial S_0}{\partial\eta}\frac{S_1}{S_0} - \frac{\partial S_1}{\partial\eta}\right),$$

and,

$$b_{11} = \frac{CM}{S_0}\left(\frac{\sinh\eta\chi}{\sinh^2\eta} - \chi e^{-\eta}(1+S_0)\right), \qquad b_{21} = \frac{-CM}{S_0}\left(\frac{\partial^2 S_\beta}{\partial\beta^2} + \frac{\partial^2 S^*_\beta}{\partial\beta^2}\right),$$
$$b_{12} = 0, \qquad b_{22} = 0,$$
$$b_{13} = 0, \qquad b_{23} = 0,$$
$$b_{14} = \frac{2CM}{S_0}e^{-\eta}(1+S_0), \qquad b_{24} = \frac{CM}{S_0}\left(\frac{\sinh\eta\chi}{\sinh^2\eta} - \chi e^{-\eta}(1+S_0)\right),$$

$$
\begin{aligned}
b_{31} &= 0, & b_{41} &= 0,\\
b_{32} &= -\frac{\partial}{\partial\chi}\left[\frac{\partial R}{\partial\chi}+\frac{\partial S_0}{\partial\chi}P\right], & b_{42} &= -\frac{\partial}{\partial\chi}\left[\frac{\partial R}{\partial\eta}+\frac{\partial S_0}{\partial\eta}P\right],\\
b_{33} &= -\frac{\partial}{\partial\eta}\left[\frac{\partial R}{\partial\chi}+\frac{\partial S_0}{\partial\chi}P\right], & b_{43} &= -\frac{\partial}{\partial\eta}\left[\frac{\partial R}{\partial\eta}+\frac{\partial S_0}{\partial\eta}P\right],\\
b_{34} &= 0, & b_{44} &= 0.
\end{aligned}
$$

Here we have defined,

$$
\begin{aligned}
R &= \frac{CM}{S_0}\left(S_\beta + S_\beta^* - 2S_0\right) + \frac{M^2}{S_0^2}S_4 - \frac{M^3}{3S_0^3}S_6,\\
P &= \frac{-CM}{S_0^2}\left(S_\beta + S_\beta^* - 2S_0\right) - \frac{2M^2}{S_0^3}S_4 + \frac{M^3}{S_0^4}S_6,
\end{aligned}
$$

and each entry is evaluated at the fixed point $\vec{x_0}$. For the form of the perturbation chosen, $\mathrm{Re}(\lambda) > 0$ corresponds to instability.

Since **A** and **B** are real-valued matrices, both λ and λ^* are eigenvalues. Since **A** and **B** has a clear block structure, if λ is an eigenvalue with the eigenvector $\vec{y}_0$, then $-\lambda$ is an eigenvalue with the eigenvector $S\vec{y}_0$, where $S = \mathrm{diag}(1,-1,-1,1)$. Therefore, eigenvalues of (3.64) occur as pairs of real or imaginary eigenvalues or as quartets of complex eigenvalues. A typical example of eigenvalues of (3.64) is shown on the left panel of Fig. 3.10 for the unstable solution B_{ss} with a pair of real and a pair of imaginary eigenvalues.

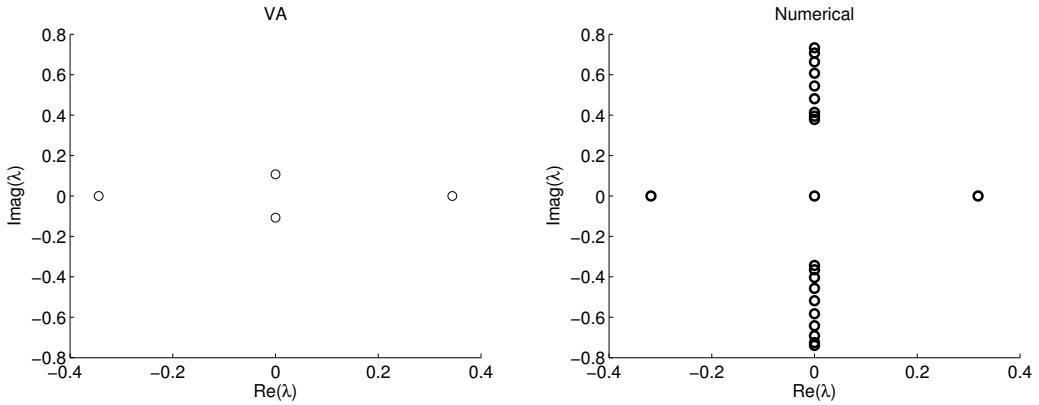

Figure 3.10: Eigenvalues corresponding to the bond-centered solution B_{ss} at $M \approx 0.5$ in the variational system (left) and the full system (right).

The spectrum for each of the variational branches S_s, S_t, A_{ts}, B_{ss}, and B_{tt}, is plotted in the left panels of Fig. 3.11. Only the bond-centered solution B_{ss} has a branch that is predicted to be unstable. The bottom left panel of the figure is a zoom of small eigenvalues in the top left panel. Where the asymmetric solution A_{ts} meets the bond-centered solution B_{ss} corresponds to stability exchange, whereas the connection to the site-centered solution S_t occurs at $\lambda^2 < 0$ and hence no stability change takes place. Note that each branch of VA solutions has exactly two pairs of real or imaginary eigenvalues of the generalized problem (3.64).

The double zero eigenvalue is captured by the variational approximation and it results in the conservation law (3.59) and the variational equation (3.60).

Small non-zero eigenvalues of the operator $\mathcal{A}$ in Eq. (3.20) which determines stability, is shown for six branches of solutions B_{ss}, B_{tt}, S_s, S_t, S_{sts}, and A_{ts} are shown in the right panels of Fig. 3.11. The overall "look" of the top panels of Fig. 3.11 are quite similar, but more importantly, the stability is correctly predicted. An interesting difference is seen in the bottom right panel of the figure. In the full problem, the collision of branches of the asymmetric A_{ts} and site-centered S_t solutions occurs at $\lambda^2 = 0$. Note that the right panels of Fig. 3.11 contains fewer eigenvalues than the left panels of Fig. 3.11 because some of the purely imaginary eigenvalues of the VA solutions approximate the essential spectrum of the full solutions. A typical example is illustrated in Fig. 3.10 for the bond-centered solution B_{ss}, where it is clear that a pair of imaginary eigenvalues of the VA solution on the left panel does not correspond to isolated eigenvalues of the full solution on the right panel.

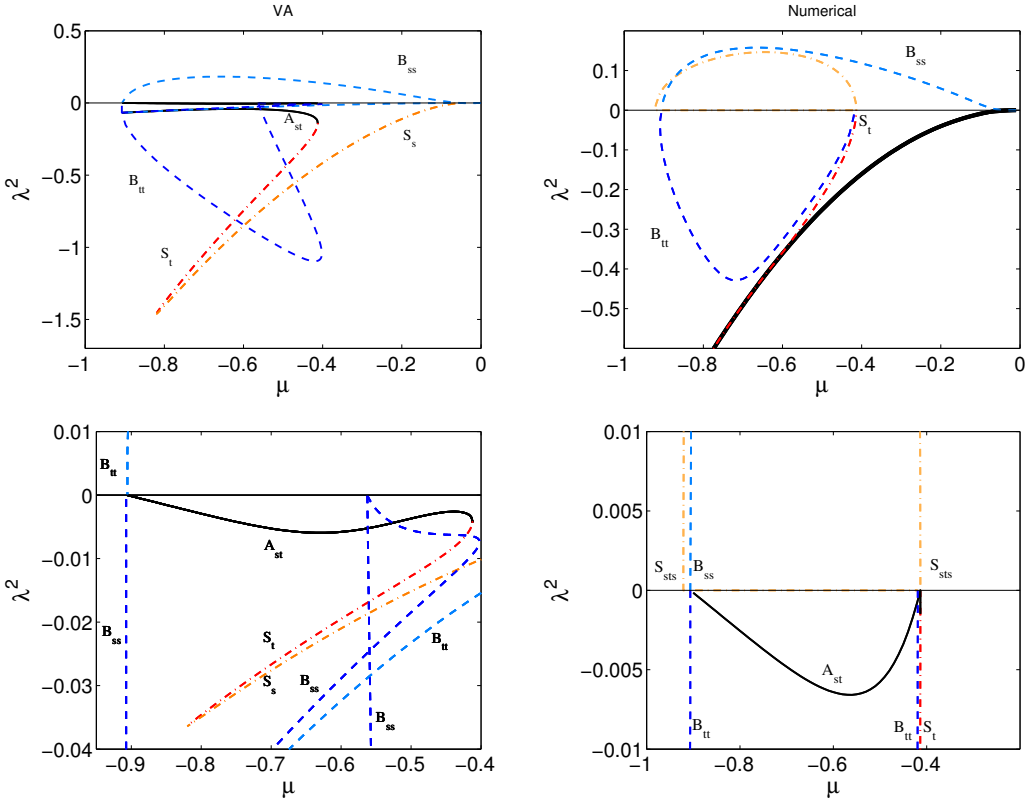

Figure 3.11: Top: plot of eigenvalues for the three families at $C = 0.1$ for the VA (left) and numerical (right) solutions. Site-centered branches are plotted as dashed-dot lines (in various shades of red for each branch) and bond-centered branches as dashed lines (in various shades of blue). The asymmetric solution is shown as a solid black line. The thick solid black line shows the boundary of the essential spectral band in the full problem. Bottom: zooms of the top panels near $\lambda^2 \approx 0$.

3.3.3 Variational approximation of the bifurcations

As before in the other sections concerning bifurcations, it is more instructive for comparison to plot the solution branches in the (μ, M) plane, where M is defined in Eq. (3.59) for the VA solutions, see Fig. 3.12. The predicted stability is also depicted.

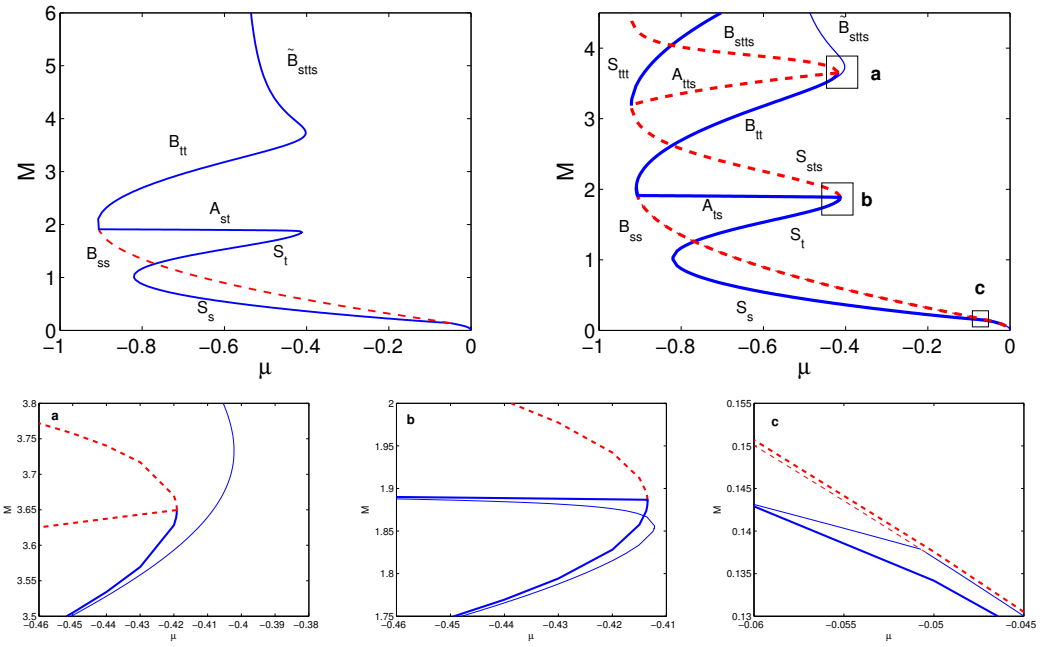

Figure 3.12: Top Left: Power of the VA solutions. Top Right: Power of the VA solutions (as shown in the left panel) superimposed with Fig. 3.5 (with thicker lines). Only the branches S_s, S_t, A_{ts}, B_{ss}, and B_{tt}, are captured by the VA. The agreement is quite good. The branch labeled $\tilde{B}_{stts}$ corresponds to the VA that fails to capture B_{stts}, as expected due to the nature of the ansatz (3.56). Bottom: Other differences between the VA and numerical power are more visible in the zooms labeled 'a', 'b' and 'c'.

As explained in Sec. 3.2.3 bifurcations occur in saddle-node, pitchfork pairs (see Fig. 3.7 for an example with the B_{ss}, B_{tt} and A_{ts} solutions). Interestingly, the VA is able to accurately capture this subtle bifurcation scenario. Figure 3.13 shows the variational approximation of the bifurcation shown in Fig. 3.7.

On the other hand, bifurcations including the site-centered solutions are not captured by the VA as well. This should not be surprising since site-centered solutions are never *truly* represented (see Fig. 3.8). We point out other minor discrepancies between the variational approximations and the numerical results in the zooms of Fig. 3.12. Zoom (a) shows where the VA (labeled $\tilde{B}_{stts}$) departs from the corresponding numerically exact solution (B_{stts} in the figure). This is expected as the ansatz (3.56) is only valid for "narrow" solutions, i.e. those that have at most two initially excited sites. Zoom (b) shows that the bifurcation of the site-centered solution S_t with the asymmetric solution A_{ts} is slightly underestimated. The S_{sts} solution is not captured by the VA (it has too many initially excited sites). Finally, zoom (c) shows that the VA falsely predicts collision of the bond B_{ss} and site-centered S_s solutions for a non-zero value of μ, similar to the cubic case discussed in [Kau05].

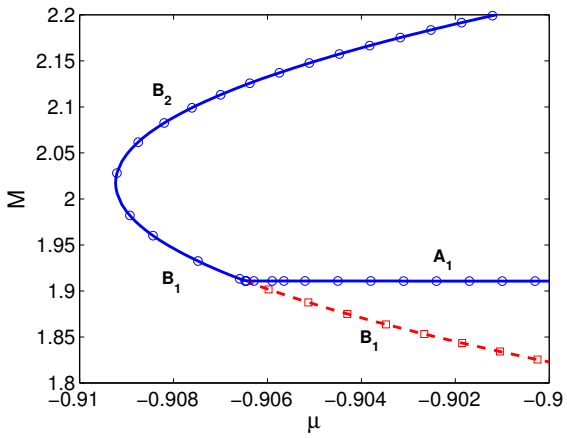

Figure 3.13: The bifurcation shown in Fig. 3.7 with the variational approximation superimposed. The power of the numerical solutions are shown as lines and whereas the power of the VA is shown as markers. Stable solutions of the VA are indicated by circles and instability by squares (see Sec. 3.3.2 for details).

We have extended the results of Ref. [Kau05] to show that not only does the VA faithfully represent the fundamental localized modes, but is also able to correctly predict the corresponding stability for small coupling constant C and power M. We showed this in the context of the cubic–quintic DNLS equation, which exhibits a family of discrete solitons, five of which were accurately captured by the variational approximation. It would be interesting to derive the variational equations in the context of time-dependent perturbations, although, the resulting equations would be far more complex and may undermine the utility of the method.

3.4 Two-dimensional model

In this section we investigate fundamental bright discrete solitons in the two-dimensional CQDNLS equation using the same structure as in the one-dimensional study.

We first establish existence and uniqueness (Sec. 3.4.1) and the subfamilies of interest (Sec. 3.4.2). The spectral problem determining stability with respect to small perturbations is defined in Sec. 3.4.3. Conjectures concerning the bifurcation structure are formulated in Sec. 3.4.4. Support for these conjectures is provided via the numerical computations described in Sec. 3.5.1. A variational approximation is also developed (Sec. 3.6), however it is in the time-independent setting so that stability cannot be predicted (in contrast to the 1D case). Finally, we investigate the mobility of the 2D discrete solitons in Sec. 3.7. A conjecture supported by numerical computations stating that mobility is related to energy differences between the solution families is formulated.

The two-dimensional cubic-quintic discrete nonlinear Schrödinger (called the 2D CQDNLS) has the following form,

$$i\partial_t \psi_{n,m} + C\Delta^{(2)}\psi_{n,m} + B|\psi_{n,m}|^2\psi_{n,m} - Q|\psi_{n,m}|^4\psi_{n,m} = 0, \tag{3.65}$$

where $\psi_{n,m}$ is the complex field at site $\{n, m\}$ and the two-dimensional discrete Laplacian is taken as,

$$\Delta^{(2)}\psi_{n,m} \equiv \psi_{n+1,m} + \psi_{n-1,m} + \psi_{n,m+1} + \psi_{n,m-1} - 4\psi_{n,m}. \tag{3.66}$$

Like the one-dimensional model the two-dimensional one has Hamiltonian structure (see Eq. (3.2)), with Hamiltonian,

$$\begin{aligned} H &= \sum_{n,m} \Big[C(|\psi_{n+1,m} - \psi_{n,m}|^2 + |\psi_{n,m+1} - \psi_{n,m}|^2) - \\ &\qquad \frac{B}{2}|\psi_{n,m}|^4 + \frac{Q}{3}|\psi_{n,m}|^6 \Big]. \end{aligned} \tag{3.67}$$

The power is defined as,

$$M = \sum_{n,m} |\psi_{n,m}|^2. \tag{3.68}$$

The Hamiltonian (3.67) and the power (3.68) are conserved quantities of the 2D CQDNLS (3.65). The conserved quantities play an important role in the study of the mobility of discrete solitons, see Sec. 3.7 below.

Scaling (3.5) can also be applied to Eq. (3.65) so that $B, Q > 0$ can be arbitrarily chosen. For included computations $B = 2$ and $Q = 1$.

Remark 3.26. The notational conventions used for the one-dimensional problem in Secs. 3.1–3.3 are used for the two-dimensional problem. In order to keep the number of symbols used for notation low, similar quantities will maintain the same name. For example, the Hamiltonian in 1D *and* 2D is H. Any reference made to the 1D analogue will be made explicitly, otherwise the 2D version should be assumed.

Remark 3.27. The model in the space of three dimensions is briefly studied in Ref. [CCGMK09]. This model is not relevant for waveguide arrays, since the time t is interpreted as a spatial coordinate (dimension of propagation), and thus an additional spatial dimension is not possible.

3.4.1 Existence and uniqueness of steady-state solutions

As before, solutions of the form,

$$\psi_{n,m} = u_{n,m} e^{-\mathrm{i}\mu t},$$

are sought, where μ is the real frequency, and the real stationary lattice field $u_{n,m}$ satisfies the following discrete equation:

$$\mu u_{n,m} + C\Delta^{(2)} u_{n,m} + 2u_{n,m}^3 - u_{n,m}^5 = 0. \tag{3.69}$$

Solutions for which the stationary field $u_{n,m}$ is complex are called discrete vortex solitons. Such solutions are discussed in review [Kev08].

We seek solutions $\mathbf{u} = \{u_{n,m}\}_{(n,m)\in\mathbb{Z}^2}$ of (3.7) in the following space:

Definition 3.28. The Hilbert space $\Omega = l^2(\mathbb{Z}^2, \mathbb{C})$ consists of square-summable bi-infinite complex sequences, equipped with the inner product $(\mathbf{v}, \mathbf{w})_\Omega = \sum_{(n,m)\in\mathbb{Z}^2} \bar{v}_{n,m} w_{n,m}$ and norm $\|\mathbf{v}\|_\Omega = \left(\sum_{(n,m)\in\mathbb{Z}^2} |v_{n,m}|^2\right)^{1/2} < \infty$.

As in the one-dimensional model, the solutions are constructed starting from the anti-continuum limit,

$$\mu u_{n,m} + 2u_{n,m}^3 - u_{n,m}^5 = 0, \tag{3.70}$$

which for fixed $\{n, m\} \in \mathbb{Z}^2$ has two non-negative solutions:

$$u_{n,m}^{\text{tall}} = \sqrt{1 + \sqrt{1+\mu}}, \qquad u_{n,m}^{\text{short}} = \sqrt{1 - \sqrt{1+\mu}}. \tag{3.71}$$

Let $\mathbf{u}^{\text{anticont}}$ denote a sequence where a finite number of points take on one of the values defined in (3.71) while the remaining points are zero.

Proposition 3.29. *Let $\mu \in (-1, 0)$. There exist a $C^* > 0$ such that for all $C \in (0, C^*)$ the lattice equation* (3.69) *has solutions that satisfy* $\lim_{C\to 0^+} u_{n,m} = u_{n,m}^{\text{anticont}}$.

Proof. We can use the same argument used to prove part (i) of Proposition 3.2 since for zero coupling the one dimensional stationary equation (3.7) and the two-dimensional one (3.69) are the same with u_n replaced by $u_{n,m}$.

□

Remark 3.30. The argument used to prove the exponential decay in part (ii) of Proposition 3.2 can not be applied for lattices of spatial dimensional greater then one.

As an alternative, it would seem natural to prove the existence of solutions in the weighted space $\tilde{\Omega}$ which consists of bi-infinite $\mathbf{u} = \{u_{n,m}\}$ sequences such that $\sum_{n,m\in\mathbb{Z}} |u_{n,m}|^2 e^{\kappa(|n|+|m|)} < \infty$. The corresponding map is,

$$\begin{aligned} F(\mathbf{v}, C) =& (\mu v_{n,m} + C\Delta v_{n,m} + 2u_{n,m}^3 - v_{n,m}^5)_{n,m\in Z}, \\ =& (\mu u_{n,m} e^{\kappa(|n|+|m|)} + 2v_{n,m}^3 e^{3\kappa(|n|+|m|)} - v_{n,m}^5 e^{5\kappa(|n|+|m|)} \\ &+ C(u_{n+1,m} e^{\kappa(|n+1|+|m|)} + u_{n-1,m} e^{\kappa(|n-1|+|m|)} + u_{n,m+1} e^{\kappa(|n|+|m+1|)} \\ &+ u_{n,m-1} e^{\kappa(|n|+|m-1|)} - 4u_{n,m} e^{\kappa(|n|+|m|)}))_{n,m\in Z} \end{aligned}$$

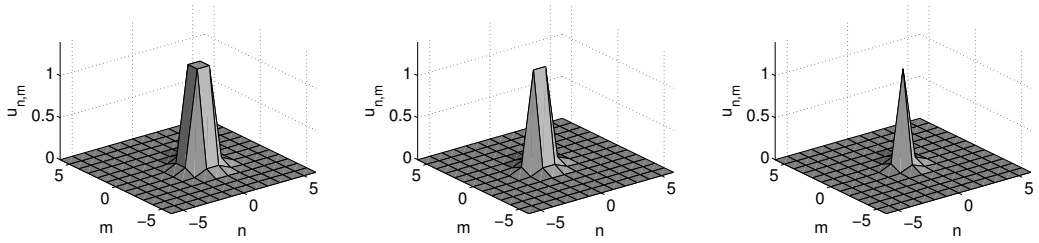

Figure 3.14: The two-dimensional B_{ss} (left), H_{ss} (middle) and S_s (left) subfamilies continued to $(\mu, C) = (-0.7, 0.1)$.

with $v_{n,m} = u_{n,m} e^{\kappa(|n|+|m|)}$. The eigenvalues of F linearized at the anticontinuum fixed point are,

$$\lambda = \mu e^{\kappa(|n|+|m|)}$$

at zero sites and,

$$\lambda = \mu e^{\kappa(|n|+|m|)} + 6(1+\sqrt{1+\mu}) e^{3\kappa(|n|+|m|)} - 4(1+\sqrt{1+\mu})^2 e^{5\kappa(|n|+|m|)}$$

at the nonzero sites. However, these can become zero valued for $\mu \in (-1, 0)$ and thus the implicit function theorem cannot be applied.

3.4.2 Classification of the steady-states

We modify the definition of the solution families in two dimensions. A solution that is symmetric in both the n and m dimensions in respect to a lattice point has site-centered symmetry. A solution that is symmetric in both the n and m dimensions in respect to the center point of four adjacent lattice point has bond-centered symmetry. For example, S_s represents a solution that has site-centered symmetry, in which the central lattice point has the value u^{short} for $C = 0$. This is the two-dimensional analogue of the 1D S_s. Another example is B_{tt} in which four excited sites form a square where each value is u^{tall}. Another fundamental type of solution that arises in higher-dimensional lattices is a hybrid between the site-centered and the bond-centered solutions along the two spatial directions. For example, we write H_{tt} to represent a solution that has two adjacent sites along the n axis defined by u^{tall}. Tables 3.5 and 3.6 shows the list of subfamilies considered for the 2D problem. These solutions are the set of initial configurations used to perform the numerical continuation (see Fig. 3.14).

3.4.3 Spectral stability

Proceeding in a way similar to the one-dimensional case, we derive equations describing the evolution of small perturbations of the steady-state solutions. Using the 2D analogue of the linearization ansatz (3.17) we obtain the non self-adjoint eigenvalue problem,

$$\begin{cases} \mu v_{n,m} - C\Delta^{(2)} v_{n,m} - 6u_{n,m}^2 v_{n,m} + 5u_{n,m}^4 v_{n,m} = -\lambda w_{n,m}, \\ \mu w_{n,m} - C\Delta^{(2)} w_{n,m} - 2u_{n,m}^2 w_{n,m} + u_{n,m}^4 w_{n,m} = \lambda v_{n,m}, \end{cases} \qquad (n,m) \in \mathbb{Z}^2. \tag{3.72}$$

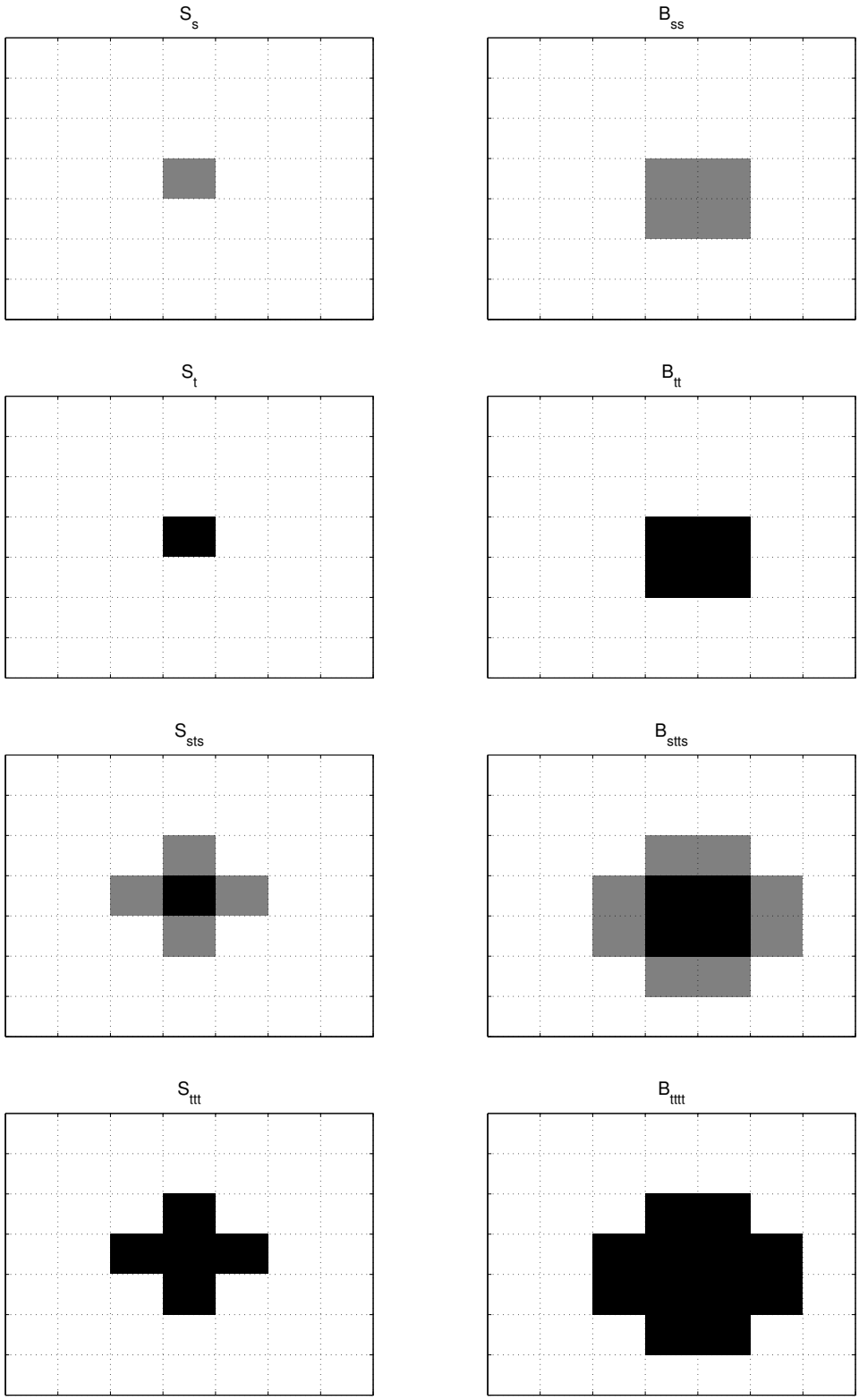

Table 3.5: Table of initial conditions ($C = 0$) for the two-dimensional site-centered and bond-centered subfamilies. Black squares represent sites defined by $u^{\text{tall}}_{n,m}$, gray squares represent sites defined by $u^{\text{short}}_{n,m}$, and white squares are zero.

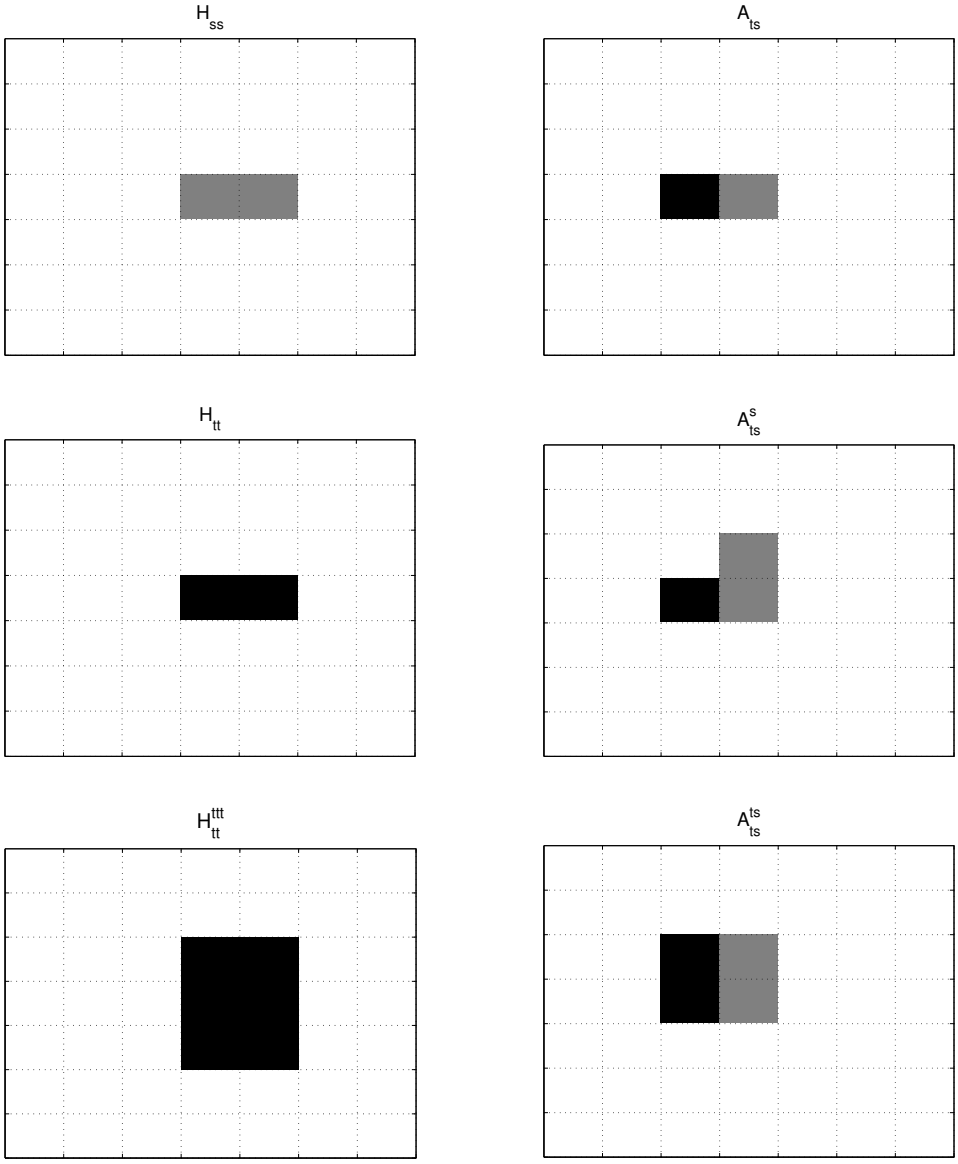

Table 3.6: Table of initial conditions for the two-dimensional hybrid and asymmetric subfamilies. Black squares represent sites defined by $u^{\text{tall}}_{n,m}$, gray squares represent sites defined by $u^{\text{short}}_{n,m}$, and white squares are zero.

As before, if there exists at least one eigenvalue such that $\mathrm{Re}(\lambda) > 0$, then the corresponding solution $\mathbf{u}e^{i\mu t}$ is unstable. Otherwise, the solution is called spectrally stable.

We seek solutions of (3.72) in the following space:

Definition 3.31. The Hilbert space $\Omega^2 = l^2(\mathbb{Z}^2, \mathbb{C}^2)$ consists of square-summable bi-infinite complex sequences, equipped with the inner product $(\mathbf{v}, \mathbf{w})_{\Omega^2} = \sum_{(n,m)\in\mathbb{Z}^2} \bar{v}_n w_n$ and norm $\|\mathbf{v}\|_{\Omega^2} = \left(\sum_{(n,m)\in\mathbb{Z}^2} |v_{n,m}|^2\right)^{1/2} < \infty$.

3.4.4 Bifurcations

It was shown in Sec. 3.4.4 that zero eigenvalues of the linearized map DF (where F is defined as the left hand side of the stationary problem Eq. (3.69)) correspond to bifurcation points and that the derivatives of the reduced function resulting from the Lyapunov-Schmidt reduction indicate the bifurcation type.

The two-dimensional case is more complicated due to the large number of symmetries. We are unable to directly apply the technique used in the one-dimensional setting to prove the existence of the interesting bifurcations resulting from the extra spatial dimensional. However, we make the following analogous conjectures:

Conjecture 3.32. *There is a pitchfork bifurcation point including the hybrid solution H_{tt} and the A^{ts}_{ts} solution and its four rotated asymmetric counter parts (see 'b' in Fig. 3.16). The associated linearization $L = DF(\mathbf{u^0}, \mu_0, C_0)$ has a one-dimensional kernel.*

There is a pitchfork bifurcation point including the hybrid solution H_{tt} and the A_{ts} solution and its four rotated counter parts (see 'd' in Fig. 3.16). The associated linearization $L = DF(\mathbf{u^0}, \mu_0, C_0)$ has a one-dimensional kernel.

Conjecture 3.33. *There is a bifurcation point including the site-centered solution S_{sts}, the A_{ts} solution (and its four rotated counter parts) and the A^s_{ts} solution (and its four rotated counter parts). The associated linearization $L = DF(\mathbf{u^0}, \mu_0, C_0)$ has a two-dimensional kernel, (see 'c' in Fig. 3.16).*

There is a bifurcation point including the bond-centered solution B_{tttt}, the A^{ts}_{ts} solution (and its four rotated counter parts) and the A^s_{ts} solution (and its four rotated counter parts). The associated linearization $L = DF(\mathbf{u^0}, \mu_0, C_0)$ has a two-dimensional kernel (see 'a' in Fig. 3.16). Moreover, the spectral problem (3.72) has 6 zero eigenvalues at this point.

This conjecture is investigated using numerical approximations of the two-dimensional discrete solitons, which is described in the next section.

3.5 Numerical approximations

To find numerical solutions in a N by N lattice we solve the equivalent one-dimensional problem,

$$\mu u_n + C(u_{n+1} + u_{n-1} + u_{n+N} + u_{n-N} - 4u_n) + 2u_n^3 - u_n^5 = 0, \tag{3.73}$$

for $|n|/2 < N^2$ with periodic boundary conditions. In this case, the solution is a N^2 dimensional vector, where the corresponding initial condition is constructed by taking a N by N initial condition, as defined in Table 3.5 and 3.6, and concatenating the N rows together. Numerical estimates of the spectrum are computed in a similar way as in the one-dimensional problem, where the 2D discrete Laplacian $\Delta^{(2)}$ is replaced by $(u_{n+1} + u_{n-1} + u_{n+N} + u_{n-N} - 4u_n)$.

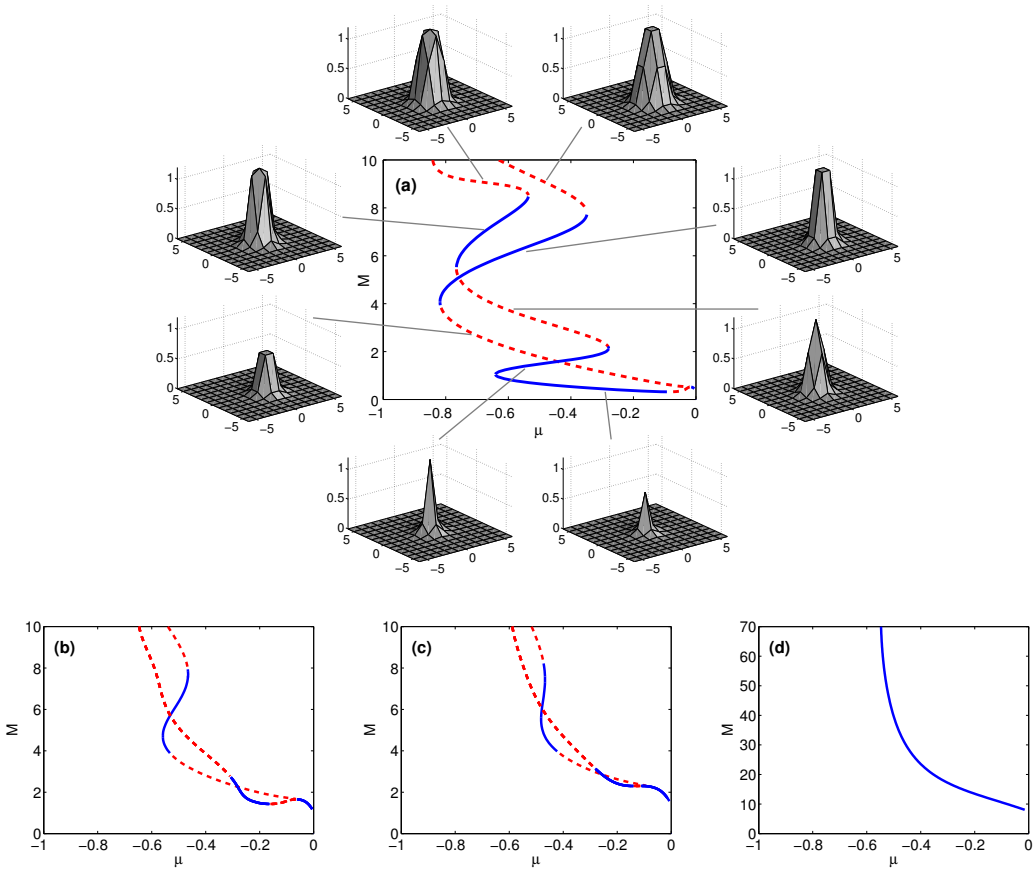

Figure 3.15: (a) Power (M) versus μ for $C = 0.1$, and respective profiles. Bottom (from left to right): Plots of the power for (b) $C = 0.3$, (c) $C = 0.4$, and (d) $C = 2.0$, of the bond-centered and site-centered solutions. For low values of C the co-existence of multiple solutions at different values of μ is obvious. The "snaking" pattern gets stretched as C increases, slowly diminishing the number of solutions. Stable and unstable solutions are represented by solid blue and dashed red curves, respectively.

3.5.1 Numerical approximations of the bifurcations

Using the numerical continuation procedure as described in Sec. 3.2.1 we can generate solution branches in the $(\mu, M(\mu))$ plane for fixed C. The snake like patterns are also present in the two-dimensional setting, as seen in Fig. 3.15. In the larger center panel (a) a plot of the $(\mu, M(\mu))$ plane is plotted for $C = 0.1$ for the bond-centered and site-centered families (other families left out for clarity). Examples of the corresponding profiles surround the center panel. As expected, as C is increased, it is observed that the curve is being "stretched" from above, eliminating the number of subfamilies (e.g. $B_{ss} = B_{tt}$ for C large enough).

Similar to what was found in the cubic DNLS equation in Ref. [FKM97] the fundamental bright discrete solitons in the 2D CQDNLS model also bifurcate from plane waves (near $\mu \approx 0$ for the CQ model). This is in contrast to the one-dimensional case, where the solutions approach the trivial solution $\mathbf{u} = 0$ for $\mu \to 0$. Additionally, Ref. [FKM97] provides heuristic arguments for the existence of energy thresholds for a large class of discrete systems with spatial dimension higher than some critical value. This claim was later proved in Ref. [Wei99] for

DNLS models with the nonlinearities of the form $|\psi_n|^{2\sigma+1}\psi_n$ and for coupled NLS equations. As can be discerned in Fig. 3.15, such thresholds seem to exist in the case of the cubic-quintic nonlinearity in two-dimensions (since as the power and energy (i.e. Hamiltonian) do not vanish at the boundary $\mu = 0$).

To find points that are described in Conjectures 3.32 and 3.33 we continue the configurations listed in Tables 3.5 and 3.6 to $C = 0.4$. After varying μ we were able to generate the bifurcation diagram shown in the top panel of Fig. 3.16.

The points labeled 'b' and 'd' in the figure correspond to bifurcations involving the hybrid solution. To approximate the dimension of the kernel we compute the singular values. The number of singular values smaller then some tolerance is an estimate of the dimension of the kernel, see [TB97, Chapter 5]. At points 'b' and 'd' there was one singular value σ_s such that $\sigma_s <$ tol where tol $= \sigma_l \cdot N \cdot 10^{-14}$ where σ_l is the largest singular value. This supports Conjecture 3.32.

The point labeled 'c' in the top panel of Fig. 3.16 corresponds to the bifurcation involving the site-centered solution. The presence of the two different types of asymmetric solutions is clear (since the powers are different). In this case, the kernel was estimated to have dimension two. The point labeled 'a' corresponds to bifurcation involving the bond-centered solution. The presence of the two different asymmetric is also clear. Again, the kernel was estimated to have dimension two. The bottom panel of Fig. 3.16 shows the relevant eigenvalues of the spectral problem (3.72) corresponding to the bifurcation labeled '**a**' in the top panel. The square of the eigenvalue is shown, so that negative values correspond to stability (purely imaginary eigenvalue) and positive values to instability (pairs of opposite signed real eigenvalues). For values of μ less than the bifurcation point $\mu \approx -0.415$ the bond-centered solution is stable. However, as the bifurcation point is approached, a *double* pair of eigenvalues of this bond-centered solution approaches the origin. As the instability threshold is crossed, two new branches of solutions also emerge through the non-standard pitchfork bifurcation scenario described above. The two bifurcating branches of asymmetric solutions are represented by dashed lines, indicating their instability. This is because of the double multiplicity of the relevant eigenvalue pair (of the bond-centered solution) which leads, for each of the newly arising branches, to a splitting to one real and one imaginary pair, as is clearly illustrated in the bottom panel of Fig. 3.16. The double pair of zero eigenvalues for the bond-centered solution plus the two zero eigenvalues due to the gauge invariance (see Remark 3.17) gives 6 zero eigenvalues, as claimed in Conjecture 3.33.

Remark 3.34. For the chosen value of C, the saddle node bifurcations of the first three narrow order solutions have vanished, e.g. $S_s = S_t = S_{sts}$ (see Fig. 3.15). The same is true for the hybrid solution so that $H_{ss} = H_{tt}$.

As a general comment, it should be noted that many of the features of the 2D cubic-quintic model (such as e.g., the existence of unstable asymmetric solutions, and their connecting of the symmetric modes) can also be observed in the case of the saturable model [VJ06], although in the present case of the cubic-quintic model, the relevant phenomenology is even richer due to, for instance, the existence of multiple (i.e., tall and short) steady states.

3.6 Variational approximation

Following the pattern of the variational approximation (VA) developed in [CGTCM06, Sec. 5] for 1D discrete solitons in the *stationary* CQDNLS model, it is possible to construct analytical

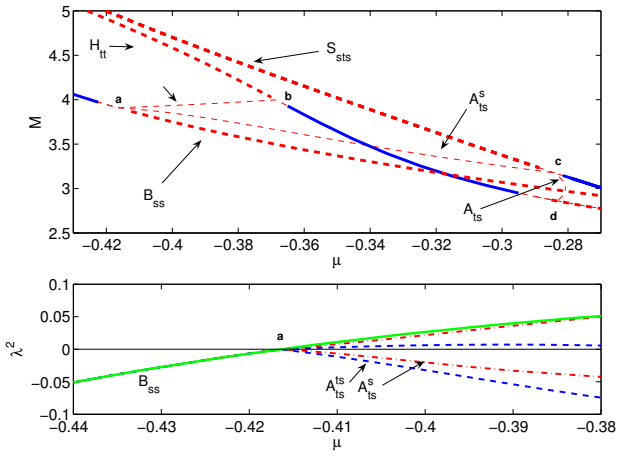

Figure 3.16: Top: The bifurcations described in Conjectures 3.32 and 3.33 for $C = 0.4$. Two families of asymmetric solutions are created where the bond-centered solution loses stability at the bifurcation point labeled by '**a**' in the diagram. One of these asymmetric solutions is connected to the hybrid solution at '**b**' and the other is connected to the site-centered solution at '**c**'. A third type of asymmetric solution also emanates from the bifurcation point '**c**' which is connected to the hybrid solution at '**d**'. Bottom: The four smallest magnitude eigenvalues of each solution corresponding to the bifurcation labeled '**a**' in the top panel. Each asymmetric solution (red dash-dot lines and blue dashed lines) has two branches, one positive and one negative. The bond-centered branch (green solid line) changes sign where the asymmetric branches are created showing that the bifurcation is that described in Conjecture 3.33.

approximations for the two-dimensional discrete solitons, and compare them to the numerical solutions described above. Unlike the 1D model, we do not perform the approximation within the context of the time-dependent problem, and therefore, we cannot estimate the spectrum determining stability.

The Lagrangian corresponding to the stationary 2D CQDNLS (3.69) is

$$\begin{aligned} \mathcal{L} &= \sum_{n,m=-\infty}^{\infty} \mu u_{n,m}^2 + u_{n,m}^4 - \frac{1}{3} u_{n,m}^6 \\ &- C\left[(u_{n+1,m} - u_{n,m})^2 + (u_{n,m+1} - u_{n,m})^2\right]. \end{aligned} \tag{3.74}$$

Similar as to what was described in the 1D case, the 2D steady-state solutions are local extrema of this Lagrangian.

3.6.1 Variational approximation of steady-states

Each family, (site-centered, bond-centered, hybrid, and asymmetric) is approximated by a localized ansatz, First, the following ansatz is used for the site-centered (sc) solution:

$$u_{m,n}^{(\mathrm{sc})} = \begin{cases} \beta & \text{if } m = n = 0, \\ A e^{-\alpha(|m|+|n|)} & \text{otherwise} \end{cases} \tag{3.75}$$

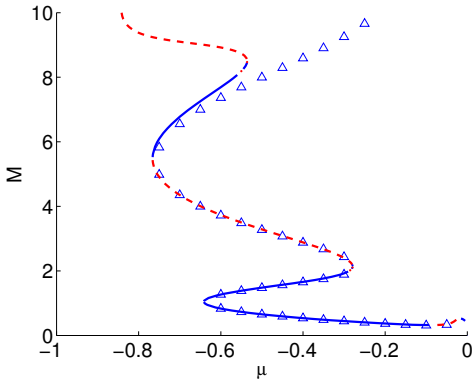

Figure 3.17: Power of the numerical solutions (solid line) and the variational approximation (triangles) for the site-centered solitons at $C = 0.1$ in the 2D lattice model. The approximation based on ansatz (3.75) is able to capture the S_s, S_t and S_{sts} subfamilies.

where A, β, and α are real constants to be found from the Euler-Lagrange equations,

$$\frac{\partial L_{\text{eff}}}{\partial A} = \frac{\partial L_{\text{eff}}}{\partial \alpha} = \frac{\partial L_{\text{eff}}}{\partial \beta} = 0, \tag{3.76}$$

L_{eff} standing for Lagrangian (3.74) evaluated with ansatz (3.75). In particular, α is treated here as one of the variational parameters. In the 1D case, the decay rate can be expressed in terms of μ and C by means of a relation obtained from the consideration of the linearized stationary equation for decaying "tails" of the soliton (see part(ii) of Proposition 3.2). We have observed, based on numerous calculations, that treating α as a variational parameter yields the same relation for α. Thus, although we do not provide an exponential decay rate for the 2D solutions, the VA suggests that it is the same as in the 1D case.

Solutions predicted by the VA based on ansatz (3.75) provide for a good fit to the S_s and S_t subfamilies and, unlike in the 1D section, the S_{sts} subfamily (see Fig. 3.17). This is due to the extra parameter b in the ansatz.

At larger values of C, the VA-predicted solutions depart from the numerical ones, which is not surprising, as the exponential cusp implied by the ansatz is not featured by the discrete solitons in the strong-coupling (quasi-continuum) model.

Other solution types can be approximated by appropriately modified *ansätze*[2]. In particular, the bond-centered (bc) soliton is based on a frame built of four points with equal amplitudes, whereas the hybrid (hy) soliton has just two points in its frame. Accordingly, the solitons of these types can be modeled by the following modifications of ansatz (3.75):

$$u_{m,n}^{(\text{bc})} = \begin{cases} \beta & m, n \in \{0, 1\} \\ Ae^{-\alpha(|m|+|n|)} & \text{if } m, n < 0 \\ Ae^{-\alpha(|m-1|+|n|)} & \text{if } m > 1, n < 0 \\ Ae^{-\alpha(|m|+|n-1|)} & \text{if } m < 0, n > 1 \\ Ae^{-\alpha(|m-1|+|n-1|)} & \text{otherwise} \end{cases} \tag{3.77}$$

[2]ansätze is the plural form of the German word ansatz.

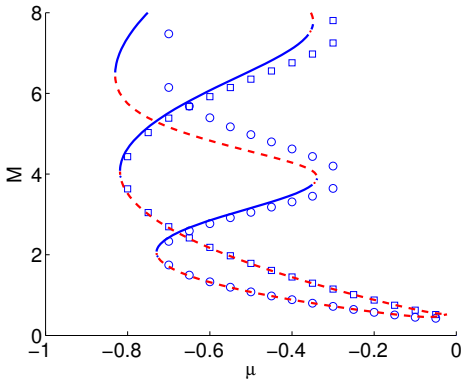

Figure 3.18: Power of the numerical solutions (solid line) and the variational approximation for the bond-centered (squares) and hybrid (circles) solitons at $C = 0.1$ in the 2D lattice model. The approximations based on the *ansätze* given in (3.77) and (3.78) respectively are able to capture subfamilies of tall and short narrow solitons.

and

$$u_{m,n}^{(\mathrm{hy})} = \begin{cases} \beta & n = 0, m \in \{0, 1\} \\ Ae^{-\alpha(|m|+|n|)} & \text{if } m, |n| < 0 \\ Ae^{-\alpha(|m-1|+|n|)} & \text{otherwise} \end{cases} \tag{3.78}$$

Further inspection demonstrates that the modified *ansätze* produce a good approximation for the short and tall narrow solutions at small C but not any of the wide families (see Fig. 3.18).

3.6.2 Variational approximations of the bifurcations

We were also able predict one of the pitchfork bifurcation scenarios of the system by introducing the appropriately chosen asymmetric (asym) ansatz:

$$u_{m,n}^{(\mathrm{asym})} = \begin{cases} \beta_1 & n = 0, m = 0 \\ \beta_2 & n = 0, m = 1 \\ \beta_3 & n = 1, m = 0 \\ \beta_4 & n = 1, m = 1 \\ Ae^{-\alpha(|m-\zeta|+|n-\zeta|)} & \text{otherwise} \end{cases} \tag{3.79}$$

The intention here is to capture the bifurcations where the site-centered and bond-centered solutions are connected via an asymmetric solution. Therefore we have some idea *a priori* what the asymmetric solutions should look like and have chosen ansatz (3.79) accordingly. For $\zeta = 0$ the ansatz has the form of a site-centered solution whereas for $\zeta = 0.5$ it will represent a bond-centered solution. All intermediate values of ζ represent asymmetric solutions that are somewhere between a site-centered and bond-centered solution. Indeed, the computed value of ζ based on the variational approximation starts near $\zeta = 0.5$ for parameter values where the asymmetric solution is almost connected to the bond-centered solution, and slowly decreases to $\zeta = 0$ as we alter the parameters until it collides with the site-centered solution

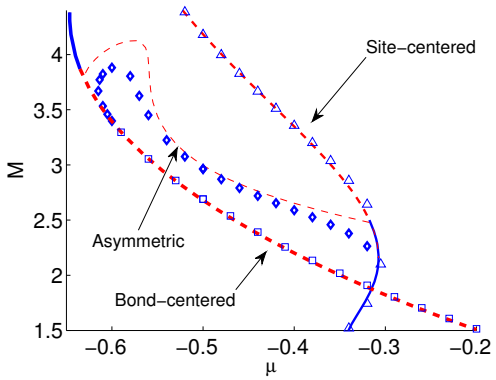

Figure 3.19: Bifurcations featuring the bond-centered, site-centered, and asymmetric solutions for $C = 0.22$ in the 2D DNLS. Numerical solutions (lines) and its predicted counterparts using the VA based on the ansatz (3.79) (markers) are in good agreement. The asymmetric VA solution captures the main qualitative features of the $M(\mu)$ curve (e.g. the dramatic increase of power around $\mu \approx -0.55$) but slightly underestimates the power at the bifurcation points.

(see Fig. 3.19). The bifurcation depicted in Fig. 3.16 is not captured by the VA, due most likely to the large coupling constant chosen.

3.7 Numerical traveling solutions

Unlike the continuous situation, traveling solutions do not generically exist in the discrete setting. In one spatial dimension, traveling breathers in DNLS equations have been found in special regions of parameter space. This was done, for example, in the context of the so-called saturable DNLS equation [MCKC06] and a DNLS with a general cubic off and onsite nonlinearities [PMC07]. Such solutions have not been found in the context of any higher dimensional DNLS type model. In fact, it is an important open question whether such solutions exist typically, since the single tail resonance appropriately made to vanish (see Ref. [MCKC06]) to obtain such exponentially localized traveling solutions in 1D settings, acquires infinite multiplicity in higher dimensional settings. Effectively mobile lattice solitons have been found in 2D models in regions of the parameter space where the so-called PN barrier is low (defined below). This has been explored numerically in the case both for quadratic nonlinearities [SKCG+07] and in the vicinity of stability exchanges for saturable models [VJ06]. The resulting mobile solutions radiate energy and eventually come to a halt.

The goal is to "kick" the stationary solutions into motion. From a Hamiltonian point of view, the real part of the solution corresponds to position and the imaginary part to momentum (see Eq. 3.3). Therefore, in order to set it into motion one should apply a perturbation that will alter the imaginary part of the solution in an asymmetric way, and thus providing it with the necessary momentum to move. This motivates the form of the perturbation,

$$\psi_{n,m}(0) = u_{n,m} e^{i(k_n n + k_m m)}, \tag{3.80}$$

where $u_{n,m}$ is a solution of the stationary problem (3.69), and k_n, and k_m are real wavenumbers. This method has been used in numerous studies in one-dimensional settings (cf. Refs. [ÖJ09, BM96]) and recently in two-dimensions [VJ06]. Bright mobile solutions were studied in this

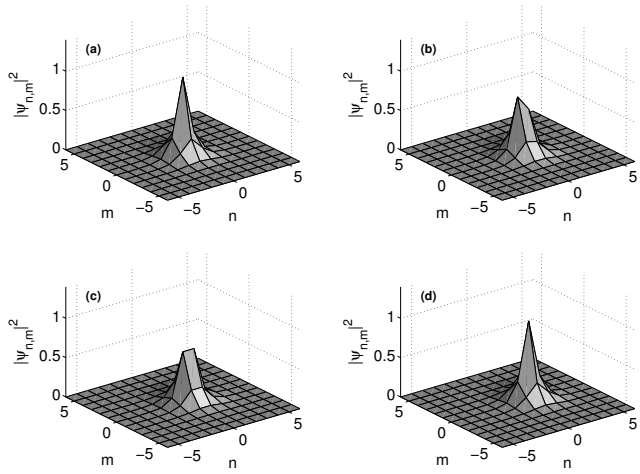

Figure 3.20: Evolution a S_{sts} solution kicked along the n axis. In the course of its motion, the traveling object takes on the (a) S_{sts}, (b) H_{tt}, and (c) A_{ts} profiles. This progression repeats starting again with the (d) S_{sts} profile until motion ceases.

way in the 1D CQDNLS model in Ref. [Cho06] and in greater detail in Ref. [MHM08]. For this reason, we start our study with the 2D model.

We define the maximum distance traveled as

$$D_{\max}(k) = \sup_{t\in[0,T_0]} \lfloor \langle n \rangle(t) \rfloor - \lfloor \langle n \rangle(0) \rfloor, \tag{3.81}$$

where the center of mass is defined as,

$$\langle n \rangle(t) = \sum_{n,m} n|\psi_{n,m}(t)|^2 / \sum_{n,m} |\psi_{n,m}(t)|^2. \tag{3.82}$$

The free energy of a solution of the form $\psi_n = u_n \exp(-\mathrm{i}\mu t)$ is defined as,

$$G = H - \mu M, \tag{3.83}$$

where H and M are the Hamiltonian and power defined in Eqs. (3.67) and (3.68) respectively. We sometimes explicitly write the corresponding solution, i.e. the free energy of the narrow site-centered solution can be written as $G(S_t)$. For simplicity, we only consider mobility along an axis ($k_n = 0 \neq k_m$ or $k_m = 0 \neq k_n$). Let us consider the S_{sts} solution traveling along the n axis. The deformations that are possible due to perturbing the S_{sts} along the n axis are the A_{ts} and H_{tt} configurations (see Fig. 3.20).

Definition 3.35. (Peierls-Nabarro barrier)
The Pierels-Nabbaro barrier for fixed (μ, C) for the S_{sts} solution with $k_n \neq 0 = k_m$ is defined as

$$PN(S_{sts}) = \max\{G(S_{sts}) - G(A_{ts}), G(S_{sts}) - G(H_{tt})\}$$

where the free energy G is defined by Eq. (3.83).

Definition 3.36. The threshold k_{depin} is defined such that if $k < k_{\text{depin}}$ then $D_{\max}(k) = 0$.

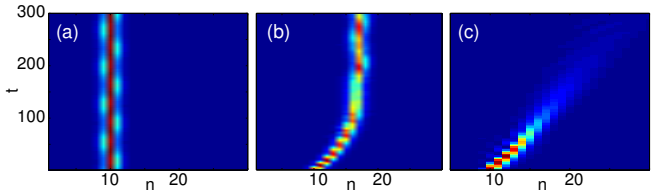

Figure 3.21: Resulting density plots, of a one-dimensional slice along the axis of propagation, from imprinting momentum to a stationary soliton by means of the "kick" defined in Eq. (3.80). (a) $k < k_{\text{depin}}$: The solution remains pinned at its initial position. (b) $k_{\text{depin}} < k_n < k_{\text{disperse}}$: The solution becomes mobile, but eventually comes to a halt due to radiation loss. (c) $k > k_{\text{disperse}}$: The kick is so strong that the solution disperses.

Definition 3.37. The threshold k_{disperse} is defined such that if $k > k_{\text{disperse}}$ then there is a τ such that for $t > \tau$, $M(\psi(t)) < \varepsilon$ where $\varepsilon << 1$. For the numerical computations, $\varepsilon = 10^{-4}$.

For physical applications (like optical switching, cf. [VMK06]) the kicking strength is only of interest for $k_{\text{depin}} < k < k_{\text{disperse}}$. Identifying these values numerically is tedious (as done below). Therefore, the following relationship between the free energy (which is easily computed) and the mobility is helpful:

Conjecture 3.38. *There is a $\tilde{C}$ such that if $(S_{sts}; \mu_a)$ and $(S_{sts}; \mu_b)$ are site-centered solutions at $\tilde{C}$ the following holds: If*

$$PN(S_{sts}; \mu_a) \leq PN(S_{sts}; \mu_b)$$

then,

$$(k_{\text{depin}}; \mu_a) \leq (k_{\text{depin}}; \mu_a).$$

We test the above conjecture by kicking the S_{sts} solutions for various μ and k_n. We first estimate the corresponding threshold values k_{depin} and k_{disperse} (see Figs. 3.21 and 3.22). There are three qualitative scenarios that we have observed as result of the kick: (a) the kick is below some threshold value, $k_n < k_{\text{depin}}$, and so the corresponding energy increase is too low to depin the solution, (b) the kick is greater than this threshold value, $k_n > k_{\text{depin}}$, and the solution is set in motion eventually halting, or (c) the initial kick is so strong, $k_n > k_{\text{disperse}}$, that the solution disperses. See Fig. 3.21 for examples of these three scenarios.

The left panel in Fig. 3.23 shows the difference in free energy, $\Delta G = G(S_t) - G(H_{tt}^t)$ between the site-centered solution and the hybrid solution for fixed $C = 0.4$ and $\mu \in [-0.3, -0.1]$. In each subpanel of the figure $D_{\max}$, as defined in Eq. (3.81), is plotted against the kicking strength for $t \in [0, 800]$ for fixed μ. In panel (i) the site-centered solution has more energy than the hybrid solution but is unstable and moves away from its initial position even for $k_n = 0$. Panel (ii) represents parameter values where the site-centered solution has greater energy and is stable. In this small "transparency window" (region between change of stability of the corresponding solutions) of parameter space, there is also a pair of unstable asymmetric solutions. In this region, we observed the best mobility (see Fig. 3.24). This is consistent with what was found in the saturable 2D DNLS [VJ06] where good mobility was observed where asymmetric solutions exist. In panel (iii) the threshold k_{disperse} is visible and the sign of ΔG has switched. In (iv) we see that the value of k_{depin} is increasing and k_{disperse} is decreasing as the PN barrier increases. Panel (v) corresponds to the maximum PN barrier. This is also where the largest k_{depin} occurs, as implied in Conjecture 3.38. As the energy difference

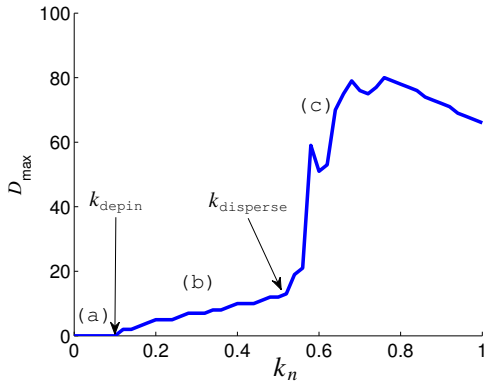

Figure 3.22: The maximum distance traveled as a function of the kicking strength k_n for $(\mu, C) = (-0.225, 0.4)$ and $t \in [0, 800]$. The area labeled (a) in the graph represents values of k_n that could not depin the solution (see Fig. 3.21.a). The area labeled by (b) consists of values of k_n that yield a mobile solution (see Fig. 3.21.b) and in (c) the kick is so strong that the solution disperses (see Fig. 3.21.c). The threshold values, k_{depin} and k_{disperse} are also shown.

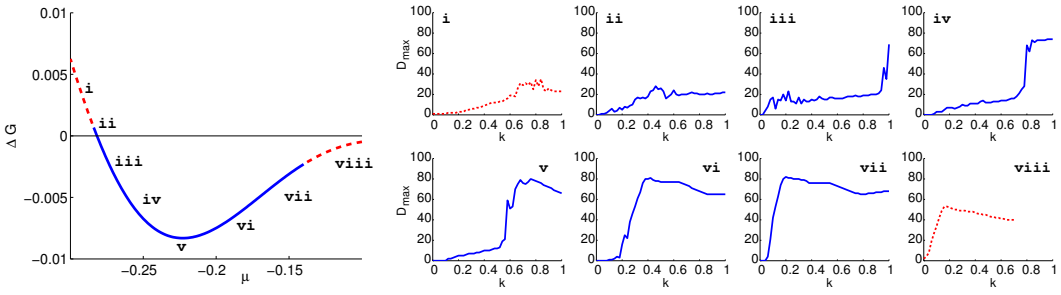

Figure 3.23: Left: Plot of ΔG for various values of μ and fixed $C = 0.4$. The remaining panels (i)–(viii) correspond to the maximum distance traveled versus kicking strength plots. See text for more details.

decreases once again as seen in (vi) the threshold k_{disperse} continues to decrease. This is also the case in panel (vii) as both thresholds approach $k_n = 0$. Finally, for the unstable region in (viii) k_{depin} is once again zero.

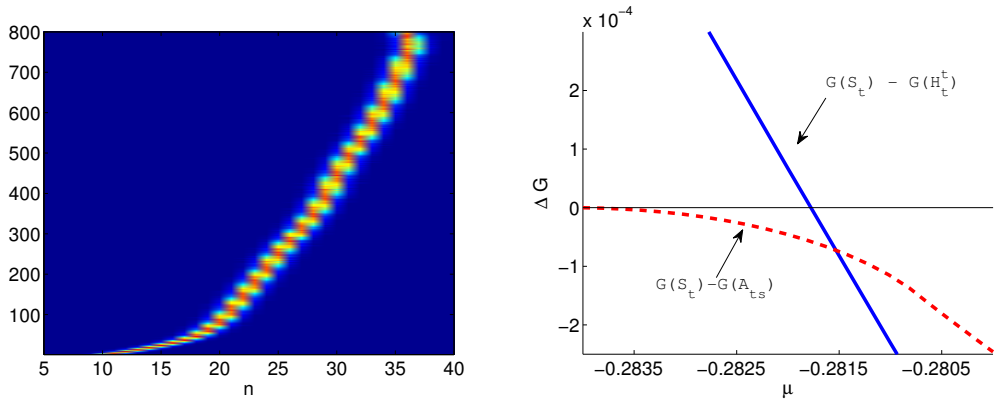

Figure 3.24: Left: Density plot for the site-centered soliton set in motion along the lattice axis for $(\mu, C) = (-0.282, 0.4)$ and $k_n = 0.5$. The choice of parameters falls in a "transparency window" where good mobility is observed, possibly due to the existence of a pair of asymmetric solutions. A one-dimensional slice along the axis of propagation (at $m = 10$) is shown here. Right: Zoom of the left panel of Fig. 3.23 near the "transparency window" where $\Delta G_{\text{hybrid}} = G(S_t) - G(H^t_{tt})$. The difference of free energy of the site-centered solution and the pair of asymmetric solutions $\Delta G_{\text{asymm j}} = G(S_t) - G(A_{st})$ is also shown. The energy added from the kick exceeds both of these differences.

The numerical results support the claim in Conjecture 3.38. Namely, that the depining strength is related to the PN barrier, which is easily computed. This was done for the S_{sts} solution for fixed $C = 0.4$. The moving states gradually lose energy and eventually get trapped at some position in the lattice. The other main result is that, the best mobility properties were found in regions were asymmetric solutions exist. This last result is consistent with what was found in the 2D DNLS model with a saturable nonlinearity [VJ06]. The authors are unaware of *any* rigorous results concerning the mobility of discrete solitons in higher dimensional DNLS equations. It is worth mentioning in passing that the energy loss in the 1D discrete sine-Gordon lattice has been recently described using an averaged Lagrangian approach in Ref. [CM08].

Appendix A

Physical setting and background

Although the focus of this thesis is the mathematical analysis and numerical simulation of the underlying *equations* describing optical phenomena, this chapter is dedicated to the physical aspect of the problem, and how the equations we study are relevant. Understanding what the models describe and how the analysis is related to the physical system is important in many ways. This serves as *one* possible justification for the mathematics, as well as motivation for new problems, and helps make clear what (if anything) is (or could be) relevant for the technology.

The physical laws that govern electromagnetic phenomena provide our starting point. These laws are referred to as the Maxwell[1] equations and in the SI units (see Table A.1) they are,

$$\nabla \times \mathcal{E} = -\frac{\partial \mathcal{B}}{\partial t}, \tag{A.1}$$

$$\nabla \times \mathcal{H} = \mathcal{J}_f + \frac{\partial \mathcal{D}}{\partial t}, \tag{A.2}$$

$$\nabla \cdot \mathcal{D} = \rho_f, \tag{A.3}$$

$$\nabla \cdot \mathcal{B} = 0, \tag{A.4}$$

where we take $\mathbf{r} = (x, y, z) \in \Omega \subset \mathbb{R}^3$ and,

$$\begin{array}{llll} \mathcal{H} : \Omega \times [0,\infty) \to \mathbb{R}^3, & \mathcal{H} = \mathcal{H}(\mathbf{r},t), & \mathcal{B} : \Omega \times [0,\infty) \to \mathbb{R}^3, & \mathcal{B} = \mathcal{B}(\mathbf{r},t), \\ \mathcal{M} : \Omega \times [0,\infty) \to \mathbb{R}^3, & \mathcal{M} = \mathcal{M}(\mathbf{r},t), & \mathcal{J}_f : \Omega \times [0,\infty) \to \mathbb{R}^3, & \mathcal{J}_f = \mathcal{J}_f(\mathbf{r},t), \\ \mathcal{E} : \Omega \times [0,\infty) \to \mathbb{R}^3, & \mathcal{E} = \mathcal{E}(\mathbf{r},t), & \mathcal{D} : \Omega \times [0,\infty) \to \mathbb{R}^3, & \mathcal{D} = \mathcal{D}(\mathbf{r},t), \\ \mathcal{P} : \Omega \times [0,\infty) \to \mathbb{R}^3, & \mathcal{P} = \mathcal{P}(\mathbf{r},t), & \rho_f : \Omega \times [0,\infty) \to \mathbb{R}, & \rho_f = \rho_f(\mathbf{r},t). \end{array}$$

Here $\mathcal{E}$ and $\mathcal{H}$ represent the electric and magnetic field vectors, respectively, and $\mathcal{D}$ and $\mathcal{B}$ are the corresponding electric displacement and magnetic flux density vectors. The vector quantity $\mathcal{J}_f$ is the free electric current density and the scalar quantity ρ_f is the free electric charge density. The quantities $\mathcal{D}$ and $\mathcal{B}$ can be expressed in terms of $\mathcal{E}$ and $\mathcal{H}$ through appropriate constitutive relations that describe the material of interest. In general, these are,

$$\mathcal{D} = \varepsilon_0 \mathcal{E} + \mathcal{P}, \tag{A.5}$$

$$\mathcal{B} = \mu_0 \mathcal{H} + \mathcal{M}, \tag{A.6}$$

[1] James Clerk Maxwell modified Ampère's law (A.2) in his seminal work *On Physical Lines of Force*.

Symbol	Description	SI unit
$\mathcal{E}$	Electric field	V/m
$\mathcal{D}$	Electric displacement	c/m^2
$\mathcal{H}$	Magnetic field	A/m
$\mathcal{B}$	Magnetic flux density	$T = Vs/m^2$
$\mathcal{J}_f$	Free electric current density	A/m^2
ρ_f	Free electric charge density	C/m^3
ε_0	Electric permittivity of free space	As/Vm
μ_0	Magnetic permeability of free space	Vs/Am

Table A.1: Table of quantities and corresponding units.

where ε_0 is the electric permittivity of free space, μ_0 is magnetic permeability of free space, and $\mathcal{P}$ and $\mathcal{M}$ are the induced polarization and magnetization. A more detailed description of the Maxwell equations can be found in Ref. [Gri99].

A.1 Derivation of continuous models

We give a brief physical description of optical fibers in Sec. A.1.1 and show how they can be modeled with continuous equations in Secs. A.1.2-A.1.4.

A.1.1 Optical fibers

The first technology we are interested in is fiber optics. They are used to guide light from one point to another, and are useful in communication applications [Hec02]. A simple example is shown in Fig. A.1. The core is usually made of silica glass and is surrounded by a cladding that has a slightly lower refractive index. Fibers of this type are called step-index fibers. In general, such a fiber can support several modes but for cores with a small radius, only a single mode can be supported. Our model equations will be based on these so-called *single mode* fibers. How we model light propagation through the fiber will depend on several features of

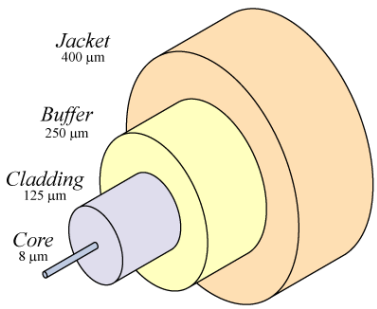

Figure A.1: Example of a single mode optical fiber[2].

the fiber, which we describe throughout Secs. A.1.2-A.1.4.

[2]This image was taken from **http** : //**en.wikipedia.org/wiki/Optical_fiber** under the terms of the *GNU Free Documentation License.*

One conceivable application is to send light pulses through the fiber which would represent a binary signal, where each state of the binary encoding is represented by the presence or absence of a light pulse (see Fig. A.2). Several of these optical signals can be sent simulta-

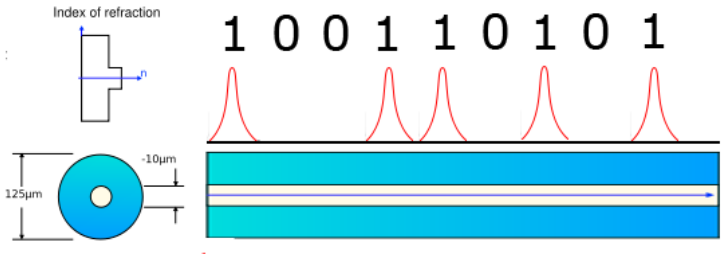

Figure A.2: Example of a binary signal in a single mode optical fiber[3].

neously through a single fiber using a wavelength division multiplexer [Lau93]. The idea is that a *multiplexed* signal consisting of pulses with different wavelengths won't interfere with each other too much, and so the integrity of the original signal will be intact. See Fig. A.3 for an illustrative example. The above description of optical communications is quite simpli-

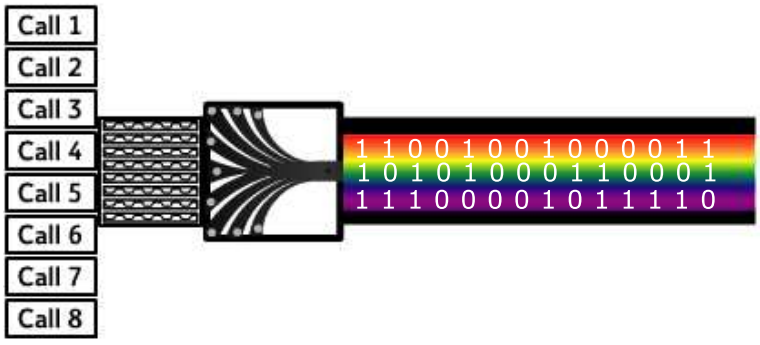

Figure A.3: Example of wavelength division multiplexing. Several signals are encoded with a multiplexer and sent through a single optical fiber and decoded at the opposite end with a de-multiplexer[4].

fied. Nonetheless, it illustrates the basic principle and motivates Chapter 2, where interaction effects of modulated pulses with different wavelengths are characterized precisely.

A.1.2 The electromagnetic wave equation

In Secs. A.1.2-A.1.4 we outline the derivation of the nonlinear Schrödinger equation in the context of single mode fibers from the Maxwell equations. By doing so, the interpretation of

[3]This is a modified version of the image found at **http : //en.wikipedia.org/wiki/Optical_fiber** under the terms of the *GNU Free Documentation License*.

[4]This is a modified version of the image found at **http : //en.wikipedia.org/wiki/Optical_fiber** under the terms of the *GNU Free Documentation License*.

the variables and parameters is clear, and we also know in what physical situations the NLS equation would be a relevant model. The derivation we outline can found in most standard physics texts on the subject, in particular we follow Ref [Agr01, Chapter 2]. We cite additional texts where the description is more detailed, as there are several items are not discussed in Ref. [Agr01].

As explained in the preceding section, the core of an optical fiber is commonly made of silica glass, which is a dielectric (i.e. an insulator). In other words, there are no free charges or currents present and so $\rho_f = \mathcal{J}_f = 0$. The material is also nonmagnetic, and thus $\mathcal{M} = 0$. With these assumptions, taking the curl of Eq. (A.1) yields,

$$\begin{aligned} \nabla \times \nabla \times \mathcal{E} &= -\nabla \times \partial_t \mathcal{B}, \\ &= -\mu_0 \partial_t \nabla \times \mathcal{H}, \\ &= -\mu_0 \partial_t^2 \mathcal{D}, \\ &= -\mu_0 \partial_t^2 \left[\varepsilon_0 \mathcal{E} + \mathcal{P}\right], \end{aligned}$$

and finally

$$\nabla \times \nabla \times \mathcal{E} = -\frac{1}{c^2}\partial_t^2 \mathcal{E} - \mu_0 \partial_t^2 \mathcal{P}, \tag{A.7}$$

where $\mu_0 \varepsilon_0 = 1/c^2$ and c is the speed of light in free space[4]. Equation (A.7) is sometimes called the electromagnetic wave equation or the Maxwell wave equation. It is *the* fundamental equation for describing wave propagation in dielectrics.

A.1.3 The Helmholtz equation

We need to supplement Eq. (A.7) with a constitutive relation between the induced polarization $\mathcal{P}$ and the electric field $\mathcal{E}$. Choosing this relationship is a delicate matter, especially if one is willing to take nonlinear responses into account. A standard expression used in the context of fiber optics, cf. [BC90, Sec. 2.1], is

$$\begin{aligned} \mathcal{P}(\mathbf{r}, t) =& \varepsilon_0 \int_{-\infty}^{\infty} \boldsymbol{\chi}^{(1)}(t - t') \cdot \mathcal{E}(\mathbf{r}, t')\, dt' \\ &+ \varepsilon_0 \int_{-\infty}^{\infty}\int_{-\infty}^{\infty} \boldsymbol{\chi}^{(2)}(t - t_1, t - t_2) \cdot \mathcal{E}(\mathbf{r}, t_1) \otimes \mathcal{E}(\mathbf{r}, t_2) dt_1\, dt_2 \\ &+ \varepsilon_0 \int_{-\infty}^{\infty}\int_{-\infty}^{\infty}\int_{-\infty}^{\infty} \boldsymbol{\chi}^{(3)}(t - t_1, t - t_2, t - t_3) \\ &\qquad \cdot \mathcal{E}(\mathbf{r}, t_1) \otimes \mathcal{E}(\mathbf{r}, t_2) \otimes \mathcal{E}(\mathbf{r}, t_3)\, dt_1\, dt_2\, dt_3 + \cdots \end{aligned} \tag{A.8}$$

where $\boldsymbol{\chi}^{(j)}$ is a $j+1$ order susceptibility tensor. The use of contracted tonsorial product $\cdot$ and the tensor product $\otimes$ allows us to avoid the use of several subscripts and thus simplify notation. There are various heuristic justifications for expressing the polarization in this way, see Ref. [Mil91, Chapter 3] and references therein for a detailed treatment.

[4]This relationship was first shown by Maxwell in his work *A Dynamical Theory of the Electromagnetic Field*. The quantities μ_0 and ε_0 were measured independently before Maxwell and it wasn't clear at that time that such a relationship exists.

For single mode fibers, we have homogeneous media along the axis of propagation of the fiber (which we take to be z). The fact that the response of the medium to the electric field at time t is also dependent on previous times is also taken into account. Due to the causality, the $\boldsymbol{\chi}^{(j)}$ vanish for $t > t'$. One must also, in principle, account for the response of the electric field of points near $\mathbf{r}$. We assume however, that the response is local and thus ignore this dependence. Because of the symmetries of the fiber and the material the odd order susceptibility tensors vanish. Thus, if we only consider one nonlinear term, we have

$$\mathcal{P}(\mathbf{r},t) = \mathcal{P}_{\mathrm{L}} + \mathcal{P}_{\mathrm{NL}}, \tag{A.9}$$

where the linear part $\mathcal{P}_{\mathrm{L}}$ is,

$$\mathcal{P}_{\mathrm{L}} = \varepsilon_0 \int_{-\infty}^{\infty} \boldsymbol{\chi}^{(1)}(t-t')\mathcal{E}(\mathbf{r},t')\,dt', \tag{A.10}$$

and,

$$\mathcal{P}_{\mathrm{NL}} = \varepsilon_0 \boldsymbol{\chi}^{(3)} \cdot \mathcal{E}(\mathbf{r},t) \otimes \mathcal{E}(\mathbf{r},t) \otimes \mathcal{E}(\mathbf{r},t), \tag{A.11}$$

where it was assumed that nonlinear response is instantaneous which amounts to ignoring the contribution of molecular vibrations to $\boldsymbol{\chi}^{(3)}$ (the Raman effect). This is a standard simplification found in the physics literature, cf. [Agr01, Sec. 2.3.1].

For polarization maintaining fibers the electric field will dominant in one component. For our choice of coordinates (propagation is along the z axis) can assume the x component dominates. Assuming all frequencies are near some center frequency ω_0 we can write,

$$\mathcal{E}(\mathbf{r},t) = \overrightarrow{\mathbf{e}_x}\left\{\frac{1}{2}E(\mathbf{r},t)e^{-\mathrm{i}\omega_0 t} + \text{c.c.}\right\}, \tag{A.12}$$

$$\mathcal{P}_{\mathrm{L}} = \overrightarrow{\mathbf{e}_x}\left\{\frac{1}{2}P_{\mathrm{L}}(\mathbf{r},t)e^{-\mathrm{i}\omega_0 t} + \text{c.c.}\right\}, \tag{A.13}$$

$$\mathcal{P}_{\mathrm{NL}} = \overrightarrow{\mathbf{e}_x}\left\{\frac{1}{2}P_{\mathrm{NL}}(\mathbf{r},t)e^{-\mathrm{i}\omega_0 t} + \text{c.c.}\right\}, \tag{A.14}$$

where $\overrightarrow{\mathbf{e}_x}$ is xth component unit vector and $E(\mathbf{r},t)$ is a slowly varying function of time. Using Eqs. (A.12),(A.13) and (A.10) the linear polarization becomes,

$$\begin{aligned} P_{\mathrm{L}}(\mathbf{r},t)e^{-\mathrm{i}\omega_0 t} &= \varepsilon_0 \int_{-\infty}^{\infty} \chi^{(1)}(t-t')E(\mathbf{r},t')e^{-\mathrm{i}\omega_0 t'}\,dt', \\ P_{\mathrm{L}}(\mathbf{r},t) &= \varepsilon_0 \int_{-\infty}^{\infty} \chi^{(1)}(t-t')E(\mathbf{r},t')e^{\mathrm{i}\omega_0 (t-t')}\,dt', \end{aligned} \tag{A.15}$$

where $\chi^{(1)} = \boldsymbol{\chi}^{(1)}_{x,x}$ is the $\overrightarrow{\mathbf{e}_x}\otimes\overrightarrow{\mathbf{e}_x}$ component of the second order tensor $\boldsymbol{\chi}^{(1)}$. Using Eqs. (A.12), (A.14) and (A.11) we obtain,

$$\frac{1}{2}P_{\mathrm{NL}}e^{-\mathrm{i}\omega_0 t} + \text{c.c.} = \varepsilon_0 \chi^{(3)}\left(\frac{1}{2}Ee^{-\mathrm{i}\omega_0 t} + \text{c.c.}\right)^3, \tag{A.16}$$

where $\chi^{(3)} = \boldsymbol{\chi}^{(3)}_{x,x,x,x}$ is the $\overrightarrow{\mathbf{e}_x} \otimes \overrightarrow{\mathbf{e}_x} \otimes \overrightarrow{\mathbf{e}_x} \otimes \overrightarrow{\mathbf{e}_x}$ component of the fourth order tensor $\boldsymbol{\chi}^{(3)}$. Expanding the cubic term gives us,

$$\left(\frac{1}{2}Ee^{-\mathrm{i}\omega_0 t} + \text{c.c.}\right)^3 = \frac{1}{8}(E^3 e^{-3\mathrm{i}\omega_0 t} + 3E^2\bar{E}e^{-\mathrm{i}\omega_0 t} + 3E\bar{E}^2 e^{\mathrm{i}\omega_0 t} + \bar{E}^3 e^{3\mathrm{i}\omega_0 t}).$$

It can be argued from a physical point of view that the terms oscillating at the frequency $3\omega_0$ are negligible in optical fibers, see Ref. [Agr01, Sec. 2.3.1], and so we can write,

$$P_{\mathrm{NL}}(\mathbf{r},t) \approx \varepsilon_0 \varepsilon_{\mathrm{NL}} E, \qquad \varepsilon_{\mathrm{NL}} = \frac{3}{4}\chi^{(3)}|E|^2. \tag{A.17}$$

Writing the polarization in this way makes the analogy to the linear situation obvious. The goal is to substitute *ansätze*[5] (A.12)-(A.14) along with the corresponding polarizations into the electromagnetic wave equation (A.7) which should result in a simplified equation, since many assumptions and implications are encapsulated in said ansätze. However, calculations will be easier if we move things over to the Fourier domain w.r.t. time,

$$\mathcal{F}\{u\}(\omega-\omega_0) = \int_{-\infty}^{\infty} u e^{\mathrm{i}(\omega-\omega_0)t} = \hat{u}(\omega-\omega_0).$$

The linear polarization (A.15) is a convolution with respect to time,

$$P_{\mathrm{L}}(\mathbf{r},\cdot) = \varepsilon_0 \left\{ \chi^{(1)}(\cdot) e^{-\mathrm{i}\omega_0 \cdot} \right\} * E(\mathbf{r},\cdot),$$

and so it follows that,

$$\begin{aligned} \hat{P}_{\mathrm{L}}(\mathbf{r},\omega-\omega_0) &= \varepsilon_0 \mathcal{F}\left\{ \chi^{(1)}(\cdot) e^{\mathrm{i}\omega_0 \cdot} \right\}(\omega-\omega_0)\ \hat{E}(\mathbf{r},\omega-\omega_0), \\ &= \varepsilon_0 \int_{-\infty}^{\infty} \chi^{(1)}(t) e^{\mathrm{i}\omega_0 t} e^{\mathrm{i}(\omega-\omega_0)t}\, dt\ \hat{E}(\mathbf{r},\omega-\omega_0), \\ &= \varepsilon_0 \hat{\chi}^{(1)}(\omega)\ \hat{E}(\mathbf{r},\omega-\omega_0). \end{aligned} \tag{A.18}$$

For optical fibers $\chi^{(3)}$ and $|E(\mathbf{r},t)|^2$ are close to their time mean values (cf. Ref. [TM01, Chapter 20]) and so we assume $\varepsilon_{\mathrm{NL}}$ is independent of time, as done in Ref. [Agr01, Sec. 2.3.1]. Thus,

$$\hat{P}_{\mathrm{NL}}(\mathbf{r},\omega-\omega_0) \approx \varepsilon_0 \varepsilon_{\mathrm{NL}} \hat{E}(\mathbf{r},\omega-\omega_0). \tag{A.19}$$

If we define $\varepsilon(\omega) = 1 + \chi^{(1)}(\omega) + \varepsilon_{\mathrm{NL}}$, and take the Fourier transform of the divergence condition (A.3) we have,

$$\nabla \cdot (\varepsilon(\omega)\hat{E}) = \nabla \cdot \hat{D} = 0.$$

For step-index fibers, the dielectric constant $\varepsilon(\omega)$ is independent of the spatial coordinates in both the core and cladding and so $\nabla \cdot (\varepsilon(\omega)\hat{E}) = \varepsilon(\omega)\nabla \cdot \hat{E}$ and so,

$$\nabla \cdot \hat{E} = 0. \tag{A.20}$$

Finally we are ready to substitute Ansätze (A.12)-(A.14) into the electromagnetic wave equation (A.7),

$$0 = \nabla \times \nabla \times \{E e^{-\mathrm{i}\omega_0 t}\} + \frac{1}{c^2}\partial_t^2 \{E e^{-\mathrm{i}\omega_0 t}\} + \mu_0 \partial_t^2 \{P_{\mathrm{L}} e^{-\mathrm{i}\omega_0 t} + P_{\mathrm{NL}} e^{-\mathrm{i}\omega_0 t}\}.$$

Applying the Fourier transform then gives,

$$0 = \nabla \times \nabla \times \{\hat{E}\} + \frac{1}{c^2}\{\omega^2 \hat{E}\} + \mu_0 \{\omega^2 \hat{P}_{\mathrm{L}} + \omega^2 \hat{P}_{\mathrm{NL}}\}.$$

[5] ansätze is the plural form of the German word ansatz.

Using the identity $\nabla \times \nabla \times u = \nabla(\nabla \cdot u) - \nabla^2 u$ and Eq. (A.20) yields,

$$0 = \nabla^2\{\hat{E}\} + \frac{1}{c^2}\{\omega^2 \hat{E}\} + \mu_0\{\omega^2 \hat{P}_{\mathrm{L}} + \omega^2 \hat{P}_{\mathrm{NL}}\}.$$

Substituting Eqs. (A.18) and (A.19) into the above expression results in a scalar equation for the $\overrightarrow{\mathbf{e}_x}$ component of $\mathcal{E}$,

$$\nabla^2 \hat{E} + \varepsilon(\omega) k^2 \hat{E} = 0, \tag{A.21}$$

which is the Helmholtz equation with $k = \omega/c$ and $\varepsilon(\omega) = 1 + \chi^{(1)}(\omega) + \varepsilon_{\mathrm{NL}}$.

A.1.4 The nonlinear Schrödinger equation

Equation (A.21) can be solved using the separation of variables technique. We make the ansatz,

$$\hat{E}(\mathbf{r}, \omega - \omega_0) = F(x, y)\hat{A}(z, \omega - \omega_0)e^{\mathrm{i}\beta_0 z}, \tag{A.22}$$

where $\hat{A}$ is a slowly varying function of z. Upon substitution of ansatz (A.22) into the Helmholtz equation (A.21) we have,

$$\hat{A}\nabla^2 F - \hat{A}F\beta_0^2 + \partial_z^2 \hat{A}F + 2\mathrm{i}\beta_0 \partial_z \hat{A}F + \varepsilon(\omega)k^2 \hat{A}F = 0. \tag{A.23}$$

Since the envelope is varying slowly, we ignore the contribution from $\partial_z^2 \hat{A}$, and so we write the above as,

$$\frac{\nabla^2 F}{F} + \varepsilon(\omega)k^2 = \beta_0^2 - \partial_z \hat{A}\frac{2\mathrm{i}\beta_0}{A}. \tag{A.24}$$

We still assert that $\varepsilon_{\mathrm{NL}}$ is a small perturbation and so Eq. (A.24) above can only be satisfied if both sides of the equation are equal to some constant $\tilde{\beta}^2$,

$$\nabla^2 F + \left(\varepsilon(\omega)k^2 - \tilde{\beta}^2\right) F = 0, \tag{A.25}$$

$$\partial_z \hat{A} 2\mathrm{i}\beta_0 + (\tilde{\beta}^2 - \beta_0^2)\hat{A} = 0. \tag{A.26}$$

The solution of Eq. (A.25) for single mode fibers with the condition that electric field is continuous across the interface of the core and cladding is given in [Agr01, Sec. 2.2]. The eigenvalue $\tilde{\beta}^2$ is,

$$\tilde{\beta}(\omega) = \beta(\omega) + \delta\beta(\omega), \tag{A.27}$$

where $\beta(\omega)$ is the eigenvalue corresponding to Eq. (A.25) for $\varepsilon_{\mathrm{NL}} = 0$ and,

$$\delta\beta(\omega) = \frac{k^2 n(\omega)}{\beta(\omega)} \frac{\int\int_{-\infty}^{\infty} \delta n |F|^2 dxdy}{\int\int_{-\infty}^{\infty} |F|^2 dxdy}, \tag{A.28}$$

where it is normal to express the effect of the polarization through the refractive indices which satisfy, see Ref. [TM01, Chapter 20],

$$\begin{aligned} \varepsilon &\approx n^2 + 2n\,\delta n, \quad n(\omega) \approx 1 + \frac{1}{2}\mathrm{Re}\hat{\chi}^{(1)}(\omega), \\ \delta n &\approx n_2|E|^2 + \frac{\mathrm{i}\alpha}{2k}, \quad n_2 \approx \frac{3}{8n(\omega)}\mathrm{Re}\hat{\chi}^{(3)}, \end{aligned}$$

where α is a term accounting for fiber loss. We now turn to solving Eq. (A.26). Since $\tilde{\beta} \approx \beta_0$ we have $\tilde{\beta}^2 - \beta_0^2 \approx 2\beta_0(\tilde{\beta} - \beta_0)$, and so we write (A.26) as,

$$\partial_z \hat{A} = \mathrm{i}(\beta + \delta\beta - \beta_0)\hat{A}. \tag{A.29}$$

However, an exact functional form of $\beta(\omega)$ is rarely known [Agr01], so we use the Taylor series centered at ω_0,

$$\beta(\omega) \approx \beta_0 + (\omega - \omega_0)\beta_1 + \frac{1}{2}(\omega - \omega_0)^2\beta_2, \tag{A.30}$$

where,

$$\beta_n = \left.\frac{d^n\beta}{d\omega^n}\right|_{\omega=\omega_0}. \tag{A.31}$$

Substituting these expressions into (A.26) yields,

$$\partial_z \hat{A} = \mathrm{i}\left((\omega - \omega_0)\beta_1 + \frac{1}{2}(\omega - \omega_0)^2\beta_2 + \delta\beta\right)\hat{A}. \tag{A.32}$$

Using the inverse Fourier transform,

$$A(z,t) = \frac{1}{2\pi}\int_{\infty}^{\infty} \hat{A}(z, \omega - \omega_0)e^{-\mathrm{i}(\omega-\omega_0)t}d\omega, \tag{A.33}$$

turns Eq. (A.32) into,

$$\partial_z A = \beta_1\partial_t A - \frac{\mathrm{i}\beta_2}{2}\partial_t^2 A + \mathrm{i}\delta\beta A. \tag{A.34}$$

If we assume that $\beta(\omega) \approx n(\omega)\omega/c$ and that $F(x,y)$ does not vary much then,

$$\delta\beta \approx \gamma|A|^2 + \frac{\mathrm{i}\alpha}{2}, \tag{A.35}$$

where,

$$\gamma = \frac{n_2\omega_0}{cA_{\text{eff}}}, \qquad A_{\text{eff}} = \frac{(\int\int_{-\infty}^{\infty}|F|^2dxdy)^2}{\int\int_{-\infty}^{\infty}|F|^4dxdy}. \tag{A.36}$$

Using the traveling coordinate frame $t = t' + \beta_1 z$ yields,

$$\partial_z A + \frac{\mathrm{i}\beta_2}{2}\partial_t^2 A + \frac{\alpha}{2} = \mathrm{i}\gamma A|A|^2, \tag{A.37}$$

which is the NLS equation.

Some of the assumptions we made in order to derive the NLS equation could be challenged on physical and/or mathematical grounds. To put the NLS equation into context and when it would be relevant to use a model equation based on this derivation, we list the assumptions used in Table A.2. A more rigorous derivation of the NLS equation from the nonlinear Klein-Gordon equation is shown in Sec. 2.1.

	Assumption	**Where assumption is used**
1.	No free charges and no induced magnetism	Derivation of Eq. (A.7)
2.	$\mathcal{P}$ and $\mathcal{E}$ far from medium resonance	Expression used for the polarization (A.8)
3.	Nonlinear polarization response is instantaneous	Eq. (A.11)
4.	Symmetries of fiber	Even order susceptibility tensors are diagonal and odd order tensors vanish
5.	Polarization is maintained	Only one component of electric field considered nonzero
6.	All frequencies are near some center frequency ω_0	Eqs. (A.12)-(A.14)
7.	Oscillations with frequency 3ω very small	Eq. (A.17)
8.	$\chi^{(3)}$ and $\lvert E(\mathbf{r},t)\rvert^2$ are close to their time mean values	$\varepsilon_{\mathrm{NL}}$ not a convolution when Fourier transform taken
9.	Step index fibers used	$\varepsilon_{\mathrm{NL}}$ independent of spatial coordinate in core and cladding
10.	Variation in z assumed to be slow	Eq. (A.24)

Table A.2: List of assumptions used to derive the NLS equation from the Maxwell equations.

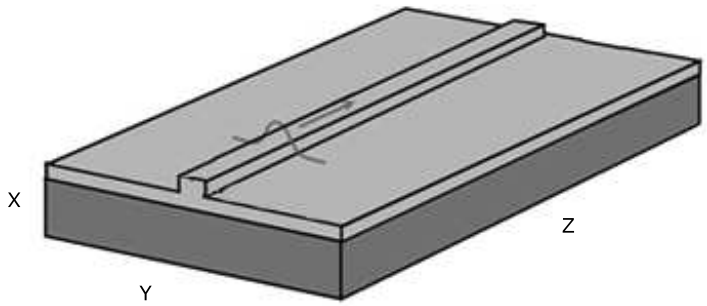

Figure A.4: A simplified version of a waveguide. The intensity of the electric field is shown propagating along the z axis. The mode is confined in the y direction which is taken to be much larger then the x component.

A.2 Derivation of discrete models

It is also possible to guide light in a different geometry. In Sec. A.2.1 we describe channel waveguides and introduce the corresponding model equation. In Sec. A.2.2 we derive coupled mode equations to describe light propagation in a coupled set of channel waveguides (i.e. directional couplers). Finally, in Sec. A.2.3 we extend this to an array of waveguides where we derive a DNLS equation. Unlike the situation for fiber optic cables, we are unaware of a detailed derivation of the DNLS equation in the context of waveguide arrays. What is presented here was extracted mainly from Ref. [Yar91, Chapter 13] and the journal articles [Jen82, CJ88, FA90].

A.2.1 Channel waveguides

Dielectric slab (or planar) waveguides guide light in a similar way to optical fibers. Similarly to the optical fiber case, the guiding part of the waveguide, or core, has a higher index of refraction than the outer layer, or cladding. This contrast makes the guiding possible. Waveguides are composed of silica glass and often doped with other elements to induce the desired nonlinear properties [SF03]. We are actually interested in a channel waveguide, as shown in Fig. A.4, which has material variation in the x and y directions. It is possible to approximate channel waveguide equations with the slab waveguide equations if we take the y direction to be significantly larger than the x direction, which is due to the so called effective refractive index which in turn is induced by the geometry. We assume light propagation along the z axis.

The electromagnetic wave equation is once again the fundamental wave propagation equation,

$$\nabla \times \nabla \times \mathcal{E} = -\frac{1}{c^2}\partial_t^2 \mathcal{E} - \mu_0 \partial_t^2 \mathcal{P},$$

since we can assume $\rho_f = J_f = \mathcal{M} = 0$ (see Sec. A.1.2). When analyzing Maxwell equations, one often transforms the problem into the *time-harmonic* equations, where the time variable

is absent. This can be done using the Fourier transform, as done in the previous section for fiber optics, or by taking an ansatz like,

$$\mathcal{E}(\mathbf{r},t) = \overrightarrow{\mathbf{e}_x}\left\{\frac{1}{2}E(x,y)e^{\mathrm{i}(\omega t-\beta z)} + \text{c.c.}\right\},$$

which corresponds to a mode with a fixed frequency ω that propagates in the z direction with propagation constant β and maintains polarization in the x component. After substituting the above ansatz into the electromagnetic wave equation (A.7) and making similar material assumptions[6] as done in Sec. A.1, we find that a mode of the waveguide is a solution of,

$$\nabla^2 E + \left(\varepsilon(\omega)k^2 - \beta^2\right)E = 0, \tag{A.38}$$

where, as before, $k = \omega/c$, and $\varepsilon(\omega) \approx n_0^2 + 2n_0n_2|E|^2$. This is the same as Eq. (A.25). We note that the distribution $E = E(x,y)$ is independent of the frequency ω. This is justified because the time of propagation is much shorter then that of optical fibers. Solutions of Eq. (A.38) were discussed in Sec. A.1.4 in the case of cylindrical geometry. In the case of a rectangular waveguide, we have the geometry as shown in Fig. A.4. We are actually interested in coupled structures, so details of solving Eq. (A.38) are omitted here (the interested reader should consult Ref. [MF53, Chapter 9]). In general, several modes will be possible. The spectrum will depend on the width of the guide, the frequency ω, and the refractive indices. For parameter values where the spectrum is discrete, the number of eigenvalues β_m, correspond to the number of confined modes supported by that configuration. Confined modes are those where the corresponding field decays exponentially in the outer part of the guide, opposed to radiation modes (corresponding to continuous part of spectrum) which oscillate throughout the surrounding layer, cf. [Yar91, Sec. 13.1].

A.2.2 Coupled mode theory

Consider the directional coupler shown in the left panel of Fig. A.5. We assume that the device is fabricated in such a way that the refractive index distribution looks like that in the right panel of Fig. A.5. This can be interpreted as two waveguides, **a** and **b**, that are in close proximity. Such devices can be used as optical switches [Yar91].

The total medium polarization of the coupled structure is taken as,

$$\mathcal{P}(\mathbf{r},t) = \varepsilon_0\mathcal{E}^{(c)}(\varepsilon^{(c)} - 1),$$

where $\mathcal{E}^{(c)}$ is corresponding electric field and $\varepsilon^{(c)}$ is the coupler dielectric parameter. We approximate the electric field of the coupled structure as a superposition of the fields of the associated isolated waveguides, i.e.

$$\mathcal{E}^{(c)} = \overrightarrow{\mathbf{e}_x}\left\{A(z)\mathcal{E}^{(a)} + B(z)\mathcal{E}^{(b)} + \text{c.c.}\right\}, \tag{A.39}$$

where $A(z)$ and $B(z)$ are the unknown functions sought and,

$$\begin{aligned}\mathcal{E}^{(a)} &= E^{(a)}(x,y)e^{\mathrm{i}(\omega t-\beta_a z)},\\ \mathcal{E}^{(b)} &= E^{(b)}(x,y)e^{\mathrm{i}(\omega t-\beta_b z)},\end{aligned}$$

[6] See Table A.3 at end of section for assumptions used to derive equations for rectangular waveguides.

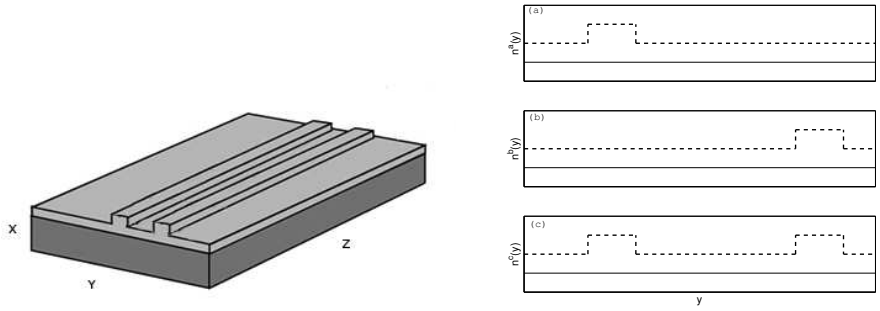

Figure A.5: Left: A section of a directional coupler. The overall dynamics are altered due to coupling between the waveguides. The equations describing a *nonlinear* directional coupler was first described in Ref. [Jen82] and later experimentally verified in [DCB87]. Right: (a) refractive index of waveguide **a**, (b) refractive index of waveguide **b**, and (c) refractive index of the coupled waveguide structure.

are the $\overrightarrow{\mathbf{e}_x}$ components of the fields of the isolated waveguides **a** and **b** respectively which solve Eq. (A.38). With this approximation, the polarization becomes,

$$\mathcal{P}(\mathbf{r},t) = \varepsilon_0(A(z)\mathcal{E}^{(a)} + B(z)\mathcal{E}^{(b)})(\varepsilon^{(c)} - 1) + \text{c.c.}.$$

Adding and subtracting $\varepsilon_0 A(z)\mathcal{E}^{(a)}\varepsilon^{(a)}$ and $\varepsilon_0 B(z)\mathcal{E}^{(b)}\varepsilon^{(b)}$ yields,

$$\mathcal{P}(\mathbf{r},t) = \varepsilon_0(P_0 + P_{\text{pert}}) + \text{c.c.}\,, \tag{A.40}$$

where,

$$P_0 = A(z)\mathcal{E}^{(a)}\varepsilon^{(a)} + B(z)\mathcal{E}^{(b)}\varepsilon^{(b)} - (A(z)\mathcal{E}^{(a)} + B(z)\mathcal{E}^{(b)}), \tag{A.41}$$

$$P_{\text{pert}} = A(z)\mathcal{E}^{(a)}(\varepsilon^{(c)} - \varepsilon^{(a)}) + B(z)\mathcal{E}^{(b)}(\varepsilon^{(c)} - \varepsilon^{(b)}). \tag{A.42}$$

We assume identical waveguides so that $E^{(b)}(x) = E^{(a)}(x-d)$ where d is suitably defined separation between waveguides and $\beta_a = \beta_b$ (called β from now on). Substitution of Eqs. (A.39) and (A.40) into the electromagnetic wave equation (A.7) leads to,

$$\begin{aligned} &A\left(\nabla^2 E^{(a)} + (k^2\varepsilon^{(a)} - \beta)E^{(a)}\right) + \frac{1}{2}\left(-2\mathrm{i}\beta\frac{\partial A}{\partial z} + \frac{\partial^2 A}{\partial z^2}\right)E^{(a)} \\ &+B\left(\nabla^2 E^{(b)} + (k^2\varepsilon^{(b)} - \beta)E^{(b)}\right) + \frac{1}{2}\left(-2\mathrm{i}\beta\frac{\partial B}{\partial z} + \frac{\partial^2 B}{\partial z^2}\right)E^{(b)} \\ &= e^{-\mathrm{i}(\omega t - \beta z)}\frac{1}{c^2}\partial_t^2 P_{\text{pert}}, \end{aligned}$$

and similarly for the corresponding complex conjugate. We know $E^{(a)}$ and $E^{(b)}$ correspond to solutions of the isolated waveguide equation, and we assume that the amplitude varies slowly in z ($\partial_z^2 A$ and $\partial_z^2 B$ are ignored) and so the above expression becomes,

$$-\mathrm{i}\beta\frac{\partial A}{\partial z}E^{(a)} - \mathrm{i}\beta\frac{\partial B}{\partial z}E^{(b)} = e^{-\mathrm{i}(\omega t - \beta z)}\frac{1}{c^2}\partial_t^2 P_{\text{pert}}. \tag{A.43}$$

Multiplying this equation by $\bar{E}^{(a)}$ (where the bar indicates complex conjugation) and integrating over the entire x domain leads to,

$$-\mathrm{i}\frac{\partial A}{\partial z} = \frac{\omega\varepsilon_0}{4}\int_{-\infty}^{\infty}\Big(A(z)E^{(a)}(\varepsilon^{(c)}-\varepsilon^{(a)}) + B(z)E^{(b)}(\varepsilon^{(c)}-\varepsilon^{(b)})\Big)\,\bar{E}^{(a)}dx, \tag{A.44}$$

where we used expression (A.42) and the mode orthogonality relation, cf. [Yar91, 13.2],

$$\int_{-\infty}^{\infty} E^n\bar{E}^m dx \approx \frac{4\omega\mu_0}{\beta}\delta_{n,m}, \tag{A.45}$$

where $\delta_{n,m}$ is Kronecker's delta. Equality holds in the case of linear waveguides. Recall that,

$$\begin{aligned}\varepsilon^{(a)} &= (n^a)^2,\\ &= (n_0^a + n_2^a|E^{(a)}A|^2)^2,\\ &\approx ((n_0^a)^2 + 2n_0^a n_2^a|E^{(a)}A|^2),\end{aligned} \tag{A.46}$$

where n_0^a is the linear refractive index and n_2^a is the nonlinear refractive index distribution of waveguide **a**. We have a similar relation for $\varepsilon^{(b)}$ and,

$$\begin{aligned}\varepsilon^{(c)} &= (n^c)^2,\\ &\approx ((n_0^c)^2 + 2n_0^c n_2^a|E^{(a)}A + E^{(b)}B|^2),\end{aligned}$$

where higher order nonlinear terms were ignored. Direct substitution of these expressions into Eq. (A.44) gives us,

$$\begin{aligned}-\mathrm{i}\frac{\partial A}{\partial z} &= Q_1A + Q_2B + (Q_3|A|^2 + 2Q_4|B|^2)A\\ &\quad + Q_5\bar{A}B^2 + Q_6A^2\bar{B} + Q_7|B|^2B + Q_8 2|A|^2B,\end{aligned} \tag{A.47}$$

where,

$$Q_1 = \frac{\omega\varepsilon_0}{4}\int |E^a|^2((n_0^c)^2 - (n_0^a)^2)\,dx, \tag{A.48}$$

$$Q_2 = \frac{\omega\varepsilon_0}{4}\int \bar{E}^a E^b((n_0^c)^2 - (n_0^b)^2)\,dx, \tag{A.49}$$

$$Q_3 = \frac{\omega\varepsilon_0}{4}\int |E^a|^4 2(n_0^c n_2^c - n_0^a n_2^a)dx, \tag{A.50}$$

$$Q_4 = \frac{\omega\varepsilon_0}{4}\int |E^a|^2|E^b|^2 2(n_0^c n_2^c - n_0^a n_2^a)\,dx, \tag{A.51}$$

$$Q_5 = \frac{\omega\varepsilon_0}{4}\int (\bar{E}^a)^2(E^b)^2 2n_0^c n_2^c\,dx, \tag{A.52}$$

$$Q_6 = \frac{\omega\varepsilon_0}{4}\int |E^a|^2 E^a\bar{E}^b 2n_0^c n_2^c\,dx, \tag{A.53}$$

$$Q_7 = \frac{\omega\varepsilon_0}{4}\int |E^b|^2 E^b\bar{E}^a(n_0^c n_2^c - n_0^b n_2^b)\,dx, \tag{A.54}$$

$$Q_8 = \frac{\omega\varepsilon_0}{4}\int |E^a|^2 E^b\bar{E}^a 2n_0^c n_2^c\,dx. \tag{A.55}$$

The expression for the z evolution of B is similar. The terms corresponding to cross phase modulation are Q_4 to Q_8 and can be ignored for small overlap between the adjacent modes [FA90]. Therefore, the system of equations for the amplitudes of weakly coupled identical waveguides are,

$$-\mathrm{i}\frac{\partial A}{\partial z} = Q_1 A + Q_2 B + Q_3 |A|^2 A, \tag{A.56}$$

$$-\mathrm{i}\frac{\partial B}{\partial z} = Q_1 B + Q_2 A + Q_3 |B|^2 B. \tag{A.57}$$

Since we have identical waveguides, the coefficients are the same for the B equation. In a general system, these would be different. Making the change of variables $A(z) = A'(z)\exp(\mathrm{i}Q_1 z)$ and $B(z) = B'(z)\exp(\mathrm{i}Q_1 z)$ gives us the following equations for A' and B',

$$-\mathrm{i}\frac{\partial A}{\partial z} = Q_2 B + Q_3 |A|^2 A, \tag{A.58}$$

$$-\mathrm{i}\frac{\partial B}{\partial z} = Q_2 A + Q_3 |B|^2 B. \tag{A.59}$$

where the primes have been dropped for notional simplicity. These are sometimes referred to as *coupled-mode* equations.

A.2.3 The discrete nonlinear Schrödinger equation

The extension of the coupled mode equations (A.58)-(A.59) to represent an *array* of weakly coupled nonlinear waveguides is straight forward (see Fig. A.6),

$$-\mathrm{i}\frac{\partial A_n}{\partial z} = Q_2(A_{n-1} + A_{n+1}) + Q_3 |A_n|^2 A_n, \tag{A.60}$$

where A_n is the amplitude of the *nth* guide. Since the waveguides are identical the quantities Q_2 and Q_3 remain unchanged. Since the uncoupled fields $E^{(n)}$ are known, finding the A_n

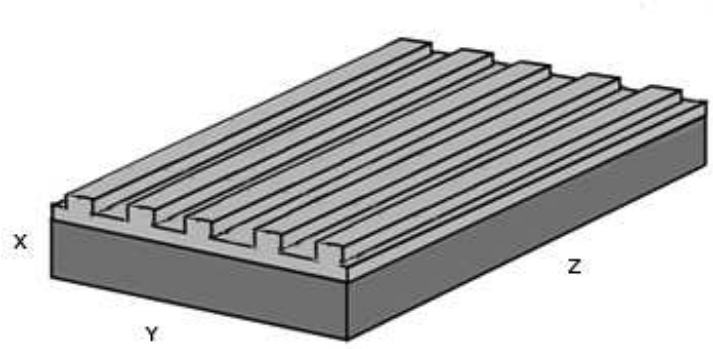

Figure A.6: A waveguide array. The equation governing a *nonlinear* waveguide array was first reported in Ref. [CJ88] and experimentally verified in Ref. [ESM+98].

will determine the total electric field. Thus we may represent the field at some z by, [Yar91, Sec. 13.9],

$$\mathbf{E}(z) \equiv \begin{pmatrix} A_1(z)e^{-i\beta z} \\ A_2(z)e^{-i\beta z} \\ \vdots \end{pmatrix} \equiv \begin{pmatrix} E_1(z) \\ E_2(z) \\ \vdots \end{pmatrix} . \tag{A.61}$$

Differentiating (A.61) with respect to z yields,

$$\frac{dE_n}{dz} = -\mathrm{i}\beta A_n e^{-i\beta z} + \frac{dA_n}{dz} e^{-i\beta z}. \tag{A.62}$$

Using Eqs. (A.60) the above becomes,

$$\frac{dE_n}{dz} = -\mathrm{i}\beta A_n e^{-i\beta z} + \mathrm{i}\left(Q_2(A_{n-1} + A_{n+1}) + Q_3|A_n|^2 A_n\right) e^{-i\beta z}, \tag{A.63}$$

and using the definition Eq. (A.61) we get,

$$-\mathrm{i}\frac{dE_n}{dz} = -\beta E_n + Q_2(E_{n-1} + E_{n+1}) + Q_3|E_n|^2 E_n. \tag{A.64}$$

Making the change of variable $E_n(z) = \psi_n(z)\exp(\mathrm{i}(2Q_2 - \beta)z)$ yields the standard discrete nonlinear Schrödinger equation,

$$-\mathrm{i}\frac{d\psi_n}{dz} = Q_2(\psi_{n-1} + \psi_{n+1} - 2\psi_n) + Q_3\psi_n|\psi_n|^2. \tag{A.65}$$

If $Q_3 > 0$ then the nonlinear term is called self-focusing, since it has the effect of concentrating, or focusing, the field distribution. $Q_3 < 0$ corresponds to the self-defocusing nonlinearity since it tends to spread the solution out.

An equation featuring the next term in the nonlinearity can be derived in the same way by using $\varepsilon \approx (n_0 + n_2|E|^2 + n_4|E|^4)$ and keeping the higher order nonlinear terms ignored in (A.46). This results in,

$$-\mathrm{i}\frac{d\psi_n}{dz} = Q_2(\psi_{n-1} + \psi_{n+1} - 2\psi_n) + Q_3\psi_n|\psi_n|^2 - Q\psi_n|\psi_n|^4,$$

where

$$Q \;=\; \frac{\omega\varepsilon_0}{4}\int |E^a|^5(n_0^c n_4^c + (n_4^c)^4 - n_0^a n_4^a - (n_4^a)^4)\, dx,$$

which is the called the CQDNLS equation. There has been experimental observation of optical nonlinearities that are best described by a combination of self-focusing cubic and self-defocusing quintic terms [BCL$^+$03, GBM$^+$04]. This corresponds to refractive indices such that $Q_3, Q > 0$.

Remark A.1. To be consistent with the existing literature we set $C \equiv Q_2$ and $B \equiv Q_3$, where B shouldn't be confused the mode coefficient used in Sec. A.2.2.

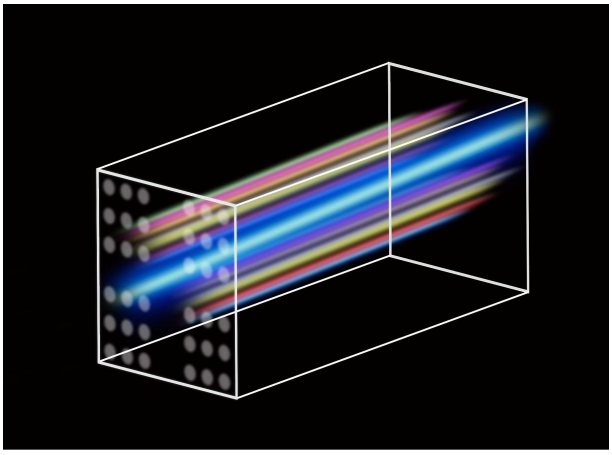

Figure A.7: Example of discrete light propagation in a two-dimensional waveguide array. Such a device is described in Ref. [PPL$^+$04] in the case of linear materials.

Although we don't derive equations for a two-dimensional waveguide array (such as the one in Fig. A.7) we write down an equation that could be a relevant model by adding an extra spatial coordinate to the CQDNLS equation,

$$-\mathrm{i}\frac{d\psi_{n,m}}{dz} = C\Delta^{(2)}\psi_{n,m} + B|\psi_{n,m}|^2\psi_{n,m} - Q|\psi_{n,m}|^4\psi_{n,m},$$

where discrete Laplacian is defined as,

$$\Delta^{(2)}\psi_{n,m} \equiv \psi_{n+1,m} + \psi_{n-1,m} + \psi_{n,m+1} + \psi_{n,m-1} - 4\psi_{n,m}.$$

The choice of this model is motivated by Ref. [PPL$^+$04] where the above is used with $B = Q = 0$. There was good agreement between the model and experimental results.

The assumptions used to derive the DNLS equation are listed in Table A.3. For more information on nonlinear waveguide arrays see review [CLS03]. It also worth mentioning that DNLS equations are also relevant in other fields, such as Bose-Einstein condensation and DNA double strand modeling (see reviews [KRB01, Kev08] and references therein).

There is less literature concerning CQDNLS equations. They provide the starting point of the results presented in Chapter 3.

	Assumption	**Where assumption is used**
1.	No free charges and no induced magnetism	Derivation of Eq. (A.7)
2.	Spatio-temporal effects ignored	$E(x, y)$ independent of ω
4.	Polarization is maintained	Only one component of electric field considered nonzero
5.	Waveguides are identical	Eq. (A.43)
6.	$\chi^{(3)}$ and $\|E(\mathbf{r}, t)\|^2$ are close to their time mean values	Eq. (A.43)
7.	Variation in z assumed to be slow	Eq. (A.43)
8.	Weak coupling between adjacent waveguides	Eqs. (A.56) and (A.57)

Table A.3: List of assumptions used to derive the DNLS equation from the Maxwell equations.

Appendix B

Symbols and notations

We tried to use conventional notation, but it was impossible to satisfy all conventions. Although defined in the text, a collection of symbols is presented here.

B.1 List of Acronyms

Acronym	Definition
CQDNLS	cubic-quintic discrete nonlinear Schrödinger
DNLS	discrete nonlinear Schrödinger
FFT	fast Fourier transform
NKG	nonlinear Klein-Gordon
NLS	nonlinear Schrödinger
NLSE	nonlinear Schrödinger equation
ODE	ordinary differential equation
PDE	partial differential equation
PS	pseudo-spectral
SI	International System of Units

B.2 Mathematical symbols and operators

Symbol	Description
$\overline{a}, a^*$	Complex conjugate of a
$*$	Convolution
$\nabla\times$	Curl operator
$\nabla\cdot$	Divergence operator
$\mathcal{F}_M$	Discrete Fourier transform taken with M points
Δ	Discrete Laplacian operator
$\mathcal{F}$	Fourier transform
$\hat{a}$	Fourier transform of a
i	Imaginary unit
$< a, b >$	Inner product
D	Jacobian operator
∇^2	Laplacian operator
$\|a\|$	Modulus of a
∂_j	Partial derivative with respect to jth argument.
$\otimes$	Tensor product
$\vec{a}, \mathbf{a}$	Vector quantity

B.3 Spaces

Space	Description
C_b^s	The space of s-times continuously differentiable functions for which $\|u\|_{C_b^s} = \sum_{j=0}^{s} \sup_{x\in\mathbb{R}} \|\partial_x^j u\|$ is finite.
$H^s(m)$	The Sobolev space of s-times weakly differentiable functions for which $\|u\|_{H^s(m)} = \|u\rho^m\|_{H^s} = (\sum_{j=0}^{s} \int \|\partial_x^j (u\rho^m)\|^2 dx)^{1/2}$ with $\rho(x) = \sqrt{1+x^2}$ is finite.
l^2	Hilbert space for which $\|\mathbf{u}\|_{l^2} = (\sum_{n\in\mathbb{Z}} \|u_n\|^2)^{1/2}$ is finite.
l^∞	Space of sequences for which $\sup \|\{u_n\}_{n\in\mathbb{Z}}\|$ is finite.
L^2	Hilbert space for which $\|u\|_{L^2} = (\int \|u\|^2 dx)^{1/2}$ is finite.

Appendix C

The NLS 2-soliton

The derivation of the two-soliton solution to the NLS equation,

$$2\mathrm{i}\omega\partial_T A + (1-c^2)\partial_X^2 A + 3|A|^2 A, = 0,$$

can be found in Ref. [OHK95]. It is,

$$A_{2-\mathrm{sol}} = \frac{2\sqrt{f_3}\eta_1 \cosh(\eta_2 t' - \sigma_2 - \mathrm{i}\psi_1)e^{-\mathrm{i}\kappa_1 t' - \mathrm{i}\theta_1}}{n_1 + n_2 + n_3} + \frac{2\sqrt{f_3}\eta_2 \cosh(\eta_1 t' - \sigma_1 - \mathrm{i}\psi_2)e^{-\mathrm{i}\kappa_2 t' - \mathrm{i}\theta_2}}{n_1 + n_2 + n_3},$$

where,

$$\begin{aligned}
\sigma_n &= -\eta_n\kappa_n x' + \sigma_{n0} \\
\theta_n &= \frac{1}{2}(\kappa_n^2 - \eta_n^2)x' + \theta_{n0} \qquad n = 1, 2 \\
\psi_1 &= ((\kappa_1 - \kappa_2)^2 + (\eta_1 - \eta_2)^2)/(2\eta_2(\kappa_1 - \kappa_2)) + \frac{\pi}{2} \\
\psi_2 &= ((\kappa_2 - \kappa_1)^2 + (\eta_2 - \eta_1)^2)/(2\eta_1(\kappa_2 - \kappa_1)) + \frac{\pi}{2} \\
f_3 &= ((\kappa_1 - \kappa_2)^2 + (\eta_1 + \eta_2)^2)/((\kappa_1 - \kappa_2)^2 + (\eta_1 - \eta_2)^2) \\
n_1 &= \cosh((\eta_1 t' - \sigma_1) + (\eta_2 t' - \sigma_2)) \\
n_2 &= f_3 \cosh((\eta_1 t' - \sigma_1) - (\eta_2 t' - \sigma_2)) \\
n_3 &= 4\eta_1\eta_2 \cos((\kappa_1 - \kappa_2)t' + \theta_1 - \theta_2)/((\kappa_1 - \kappa_2)^2 + (\eta_1 - \eta_2)^2)
\end{aligned}$$

with parameters $t' = T\sqrt{\mathrm{i}\omega/3}$ and $x' = X2\mathrm{i}\omega/(1-c^2)$ and $\sigma_{n0}, \theta_{n0}, \eta_n, \kappa_n, \in \mathbb{R}$.

Bibliography

[ABK04] G.L. Alfimov, V.A. Brazhnyi, and V.V. Konotop. On classification of intrinsic localized modes for the discrete nonlinear Schrödinger equation. *Physica D*, 194:127, 2004.

[Agr01] G.P. Agrawal. *Nonlinear fiber optics Optics*. Academic Press, London, 2001.

[AKL79] M. J. Ablowitz, M. D. Kruskal, and J. F. Ladik. Solitary wave collisions. *SIAM J. Appl. Math.*, 36:428–437, 1979.

[ASY96] K. Alligood, T. Sauer, and J.A. Yorke. *CHAOS: An introduction to dynamical systems*. Springer, New York, 1996.

[Aub06] S. Aubry. Discrete Breathers: Localization and transfer of energy in discrete Hamiltonian nonlinear systems. *Physica D*, 216:1–30, April 2006.

[BC90] P.N. Butcher and D.N. Cotter. *The elements of nonlinear optics*. Cambridge university press, Cambridge, 1990.

[BCL+03] G. Boudebs, S. Cherukulappurath, H. Leblond, J. Troles, F. Smektala, and F. Sanchez. Experimental and theoretical study of higher-order nonlinearities in chalcogenide glasses. *Opt. Commun.*, 219:427–433, 2003.

[BF06] A. Babin and A. Figotin. Linear superposition in nonlinear wave dynamics. *Rev. Math. Phys.*, 18:971–1053, 2006.

[BM96] O. Bang and P.D. Miller. Exploiting discreteness for switching in arrays of nonlinear waveguides. *Phys. Scripta*, T67:26, 1996.

[BMW94] B. Birnir, H.P. McKean, and A. Weinstein. The rigidity of sine-Gordon breathers. *Comm. Pure Appl. Math.*, 47:1043–1051, 1994.

[BRI05] A. Bondeson, T. Rylander, and P. Ingelström. *Computational electromagnetics*. Springer, New York, 2005.

[CB09] M. Chirilus-Bruckner. *Nonlinear interaction of pulses*. PhD thesis, Universität Karlsruhe (TH), Karlsruhe, Germany, 2009.

[CBCSU08] M. Chirilus-Bruckner, C. Chong, G. Schneider, and H. Uecker. Separation of internal and interaction dynamics for NLS-described wave packets with different carrier waves. *J. Math. Anal. Appl.*, 347:304–314, 2008.

[CBSU07] M. Chirilus-Bruckner, G. Schneider, and H. Uecker. On the interaction of NLS-described modulating pulses with different carrier waves. *Math. Method. Appl. Sci.*, 15:1965–1978, 2007.

[CCGMK09] C. Chong, R. Carretero-González, B.A. Malomed, and P.G. Kevrekidis. Multistable solitons in higher-dimensional cubic–quintic nonlinear Schrödinger lattices. *Physica D*, 238:126 – 136, 2009.

[CE85] J. Carr and J. Eilbeck. Stability of stationary solutions of the discrete self-trapping equation. *Phys. Lett. A*, 109:201–204, 1985.

[CGTCM06] R. Carretero-González, J. D. Talley, C. Chong, and B.A. Malomed. Multistable solitons in the cubic–quintic discrete nonlinear Schrödinger equation. *Physica D*, 216:77–89, 2006.

[Chi99] C.C. Chicone. *Ordinary differential equations with applications*. Springer, New York, 1999.

[CHL08] D. Cohen, E. Hairer, and C. Lubich. Conservation of energy, momentum and actions in numerical discretizations of nonlinear wave equations. *Numer. Math.*, 110:113–143, 2008.

[Cho06] C. Chong. Solitons in discrete nonlinear media with higher order nonlinearities. Master's thesis, San Diego State University, San Diego, 2006.

[CJ88] D. N. Christodoulides and R. I. Joseph. Discrete self-focusing in nonlinear arrays of coupled waveguides. *Opt. Lett.*, 13:794–796, 1988.

[CKFM09] J. Cuevas, P.G. Kevrekidis, D.J. Frantzeskakis, and B.A. Malomed. Discrete solitons in nonlinear Schrödinger lattices with a power-law nonlinearity. *Physica D*, 238:67–76, 2009.

[CLS03] D. N. Christodoulides, F. Lederer, and Y. Silberberg. Discretizing light behaviour in linear and nonlinear waveguide lattices. *Nature*, 424:817–823, 2003.

[CM08] L.A. Cisneros and A.A. Minzoni. Asymptotics for kink propagation in the discrete Sine-Gordon equation. *Physica D*, 237:50–65, 2008.

[DCB87] U. Das, Y. Chen, and P. Bhattacharya. Nonlinear effects in coplanar GaAs/InGaAs strained-layer superlattice directional couplers. *Appl. Phys. Lett.*, 51:1679–1681, 1987.

[Den93] J. Denzler. Nonpersistence of breather families for the perturbed sine Gordon equation. *Commun. Math. Phys.*, 158:397–430, 1993.

[Die69] J. Dieudonne. *Foundations of Modern Analysis*. Academic, New York, 1969.

[DJ89] P.G. Drazin and R.S. Johnson. *Solitons: an introduction*. Cambridge university press, Cambridge, 1989.

[ESM+98] H. S. Eisenberg, Y. Silberberg, R. Morandotti, A. R. Boyd, and J. S. Aitchison. Discrete spatial optical solitons in waveguide arrays. *Phys. Rev. Lett.*, 81:3383–3386, 1998.

[FA90] F. J. Fraile-Pelaez and G. Assanto. Coupled-mode equations for nonlinear directional couplers. *Appl. Optics*, 29:2216–2217, 1990.

[FKM97] S. Flach, K. Kladko, and R. S. MacKay. Energy thresholds for discrete breathers in one-, two-, and three-dimensional lattices. *Phys. Rev. Lett.*, 78:1207–1210, 1997.

[GBM+04] R. A. Ganeev, M. Baba, M. Morita, A. I. Ryasnyansky, M. Suzuki, M. Turu, and H. Kuroda. Fifth-order optical nonlinearity of pseudoisocyanine solution at 529 nm. *J. Opt. A: Pure Appl. Opt.*, 6:282–287, 2004.

[GO77] D. Gottlieb and S.A. Orszag. *Numerical analysis of spectral methods.* SIAM, Philadelphia, 1977.

[Gri99] D.J. Griffths. *Introduction to electrodynamics 3rd ed.* Prentice Hall, New Jersey, 1999.

[GSS88] M. Golubitsky, D.G. Schaeffer, and I. Stewart. *Singularities and groups in bifurcation theory*, volume 2:. Springer, New York, 1988.

[Hec02] J. Hecht. *Understanding fiber optics, 4th ed.* Prentice-Hall, New Jersey, 2002.

[Hen81] D. Henry. *Geometric theory of semilinear parabolic equations.* Springer, New York, 1981.

[HJ90] R.A. Horn and C.R. Johnson. *Matrix analysis.* Cambridge University Press, Cambridge, 1990.

[HLW00] E. Hairer, C. Lubich, and G. Wanner. *Geometric numerical integration.* Springer, New York, 2000.

[HS95] P.D. Hislop and I.M. Sigal. *Introduction to spectral theory: with applications to Schrödinger operators.* Springer, New York, 1995.

[Jen82] S.M. Jensen. The nonlinear coherent coupler. *IEEEJ. Quantum Electron.*, QE-18:1580, 1982.

[JM03] Eilbeck J.C. and Johansson M. The discrete nonlinear Schrödinger equation - 20 years on. In *Zorzano (Ed.), Proceedings of the third conference on localization and energy transfer in nonlinear systems, June 17-21*, pages 44–67, 2003.

[Kau05] D.J. Kaup. Variational solutions for the discrete nonlinear Schrödinger equation. *Math. Comput. Simulat.*, 69:322–333, 2005.

[Kev08] P.G. Kevrekidis. *The discrete nonlinear Schrödinger equation: mathematical analysis, numerical computations and physical perspectives.* Springer, New York, 2008.

[KRB01] P.G. Kevrekidis, K.Ø. Rasmussen, and A.R. Bishop. The discrete nonlinear Schrödinger equation: a survey of recent results. *Int. J. Mod. Phys. B*, 15:2833–2900, 2001.

[KSM92] P. Kirrmann, G. Schneider, and A. Mielke. The validity of modulation equations for extended systems with cubic nonlinearities. *Proc. of the Royal Society of Edinburgh*, 122A:85–91, 1992.

[Lau93] J. Laude. *Wavelength division multiplexing*. Prentice-Hall, New Jersey, 1993.

[MA94] R.S. MacKay and S. Aubry. Proof of existence of breathers for time-reversible or Hamiltonian networks of weakly coupled oscillators. *Nonlinearity*, 7:1623–1643, 1994.

[Mal02] B.A. Malomed. Variational methods in nonlinear fiber optics and related fields. *Prog. Opt.*, 43:71–193, 2002.

[Mat08a] Mathworks. MATLAB fast Fourier transform documentation. `www.mathworks.com/access/helpdesk/help/techdoc/ref/fft.html`, 2008.

[Mat08b] Mathworks. Maximizing MATLAB performance. `http://www.mathworks.com/access/helpdesk_r13/help/techdoc/matlab_prog/ch7_perf.html`, 2008.

[MCKC06] T.R.O. Melvin, A.R. Champneys, P.G. Kevrekidis, and J. Cuevas. Radiationless traveling waves in saturable nonlinear Schrödinger lattices. *Phys. Rev. Lett.*, 97:124101, 2006.

[MF53] P.M. Morse and H. Feshbach. *Methods of theoretical physics*, volume 2: Chapters 9 to 13. McGraw-Hill, New York, 1953.

[MGDM05] I.M. Merhasin, B.V. Gisin, R. Driben, and B.A. Malomed. Finite-band solitons in the Kronig-Penney model with the cubic-quintic nonlinearity. *Phys. Rev. E*, 71:016613, 2005.

[MHM08] A. Maluckov, L. Hadžievski, and B.A. Malomed. Staggered and moving localized modes in dynamical lattices with the cubic-quintic nonlinearity. *Phys. Rev. E*, 77:036604, 2008.

[Mil91] D.L. Mills. *Nonlinear optics*. Springer, New York, 1991.

[MW96] B.A. Malomed and M.I. Weinstein. Soliton dynamics in the discrete nonlinear Schrödinger equation. *Phys. Lett. A*, 220:91–96, 1996.

[OHK95] T. Okamawari, A. Hasegawa, and Y. Kodoma. Analyses of soliton interactions by means of a perturbed inverse-scattering transformation. *Phys. Rev. A*, 51:250–2497, 1995.

[ÖJ09] M. Öster and M. Johansson. Stability, mobility and power currents in a two-dimensional model for waveguide arras with nonlinear coupling. *Physica D*, 238:88–99, 2009.

[OY74] M. Oikawa and N. Yajima. A perturbation approach to nonlinear systems. 2: Interaction of nonlinear modulated waves. *J. Phys. Soc. Japan*, 37:486–496, 1974.

[PKMF03] I.E. Papacharalampous, P.G. Kevrekidis, B.A. Malomed, and D.J. Frantzeskakis. Soliton collisions in the discrete nonlinear Schrödinger equation. *Phys. Rev.*, 68:046604, 2003.

[PMC07] D.E. Pelinovsky, T.R.O. Melvin, and A.R. Champneys. One-parameter localized traveling waves in nonlinear Schrödinger lattices. *Physica D*, 236:22–43, 2007.

[PPL+04] T. Pertsch, U. Peschel, F. Lederer, J. Burghoff, M. Will, S. Nolte, and A. Tünnermann. Discrete diffraction in two-dimensional arrays of coupled waveguides in silica. *Opt. Lett.*, 29:468–470, 2004.

[PPT79] Kh. I. Pushkarov, D. I. Pushkarov, and I. V. Tomov. Self-action of light beams in nonlinear media: soliton solutions. *Opt. Quantum Electron.*, 11:471, 1979.

[PW96] R.D. Pierce and C.E. Wayne. On the validity of mean field amplitude equations for counterpropagating wavetrains. *Nonlinearity*, 8:433–457, 1996.

[PZ04] A. D. Polyanin and V. F. Zaitsev. *Handbook of nonlinear partial differential equations*. Chapman and cats Hall/CRC, Boca Raton, 2004.

[Sch91] W. E. Schiesser. *The numerical method of lines*. Academic Press, London, 1991.

[SF03] T. Suhara and M. Fujimura. *Waveguide nonlinear-optic devices*. Springer, New York, 2003.

[SK87] H. Segur and M.D. Kruskal. Nonexistence of small-amplitude breathers in ϕ^4 theory. *Phys. Rev. Lett.*, 58:747–50, 1987.

[SKCG+07] H. Susanto, P.G. Kevrekidis, R. Carretero-González, B.A. Malomed, and D.J. Frantzeskakis. Mobility of discrete solitons in quadratically nonlinear media. *Phys. Rev. Lett.*, 99:214103, 2007.

[SS99] C. Sulem and P.L. Sulem. *The nonlinear Schrödinger equation: self-focusing and wave collapse*. Springer, New York, 1999.

[Str04] J.C. Strikwerda. *Finite difference schemes and partial differential equations*. SIAM, Philadelphia, 2004.

[Tao06] T. Tao. *Nonlinear dispersive equations*. American Mathematical Society, Providence, 2006.

[TB97] L.N. Trefethen and D. Bau. *Numerical linear algebra*. SIAM, Philadelphia, 1997.

[Tho95] J.W. Thomas. *Numerical partial differential equations: finite difference methods*. Springer, New York, 1995.

[TM01] R. Temam and A. Miranville. *Mathematical modeling in continuum mechanics*. Cambridge university press, Cambridge, 2001.

[TPB04] L. Tkeshelashvili, S. Pereira, and K. Busch. General theory of nonresonant wave interaction: Giant soliton shift in photonic band gap materials. *Europhys. Lett.*, 86(2):205–211, 2004.

[VJ06] R.A. Vicencio and M. Johansson. Discrete soliton mobility in two-dimensional waveguide arrays with saturable nonlinearity. *Phys. Rev. E*, 73:046602, 2006.

[VMK06] R.A. Vicencio, M.I. Molina, and Y.S. Kivshar. All-optical switching and amplification of discrete vector solitons in nonlinear cubic birefringent waveguide arrays. *Phys. Rev. E*, 73:046602, 2006.

[Wei99] M.I. Weinstein. Excitation thresholds for nonlinear localized modes on lattices. *Nonlinearity*, 12:673, 1999.

[Wig03] S. Wiggins. *Introduction to applied nonlinear dynamical systems and chaos*. Springer, New York, 2003.

[WMGS91] S.B. Wineberg, J.F. McGrath, E.F. Gabl, and C.E. Scott. Implicit spectral methods for wave propagation problems. *J. Comput. Phys.*, 97:311–336, 1991.

[Yar91] A. Yariv. *Optical electronics*. Saunders College Publishing, Philadelphia, 1991.